PERCEPTUALLY INSPIRED VARIATIONAL RETINEX METHODS FOR ENHANCING AND RESTORING IMAGES

Thesis

Submitted in partial fulfillment of the requirements for the degree of

DOCTOR OF PHILOSOPHY

by

FEBIN I.P.

DEPARTMENT OF MATHEMATICAL AND COMPUTATIONAL SCIENCES

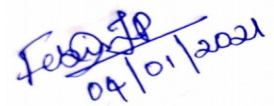NATIONAL INSTITUTE OF TECHNOLOGY KARNATAKA,

SURATHKAL, MANGALORE - 575 025

JANUARY 2021

DECLARATION
By the Ph.D. Research Scholar

I hereby declare that the Research Thesis entitled **PERCEPTUALLY INSPIRED VARIATIONAL RETINEX METHODS FOR ENHANCING AND RESTORING IMAGES** which is being submitted to the **National Institute of Technology Karnataka, Surathkal** in partial fulfillment of the requirements for the award of the Degree of **Doctor of Philosophy** in **Mathematical and Computational Sciences** is a *bonafide report of the research work carried out by me.* The material contained in this Research Thesis has not been submitted to any University or Institution for the award of any degree.

177159MA501, Febin I.P.
(Register Number, Name & Signature of the Research Scholar)

Department of Mathematical and Computational Sciences

Place: NITK-Surathkal

Date: 04/01/2021

CERTIFICATE

This is to *certify* that the Research Thesis entitled **PERCEPTUALLY INSPIRED VARIATIONAL RETINEX METHODS FOR ENHANCING AND RESTORING IMAGES** submitted by **Ms. FEBIN I.P.**, (Register Number: 177159MA501) as the record of the research work carried out by her is *accepted as the Research Thesis submission* in partial fulfillment of the requirements for the award of degree of **Doctor of Philosophy**.

Dr. JIDESH P

Research Guide

Chairman - DRPC

(Signature with Date and Seal)

ACKNOWLEDGEMENTS

Place: NITK, Surathkal   FEBIN I.P.

Date: 04-01-2021

ABSTRACT OF THE THESIS

Image restoration and enhancement are the two inevitable pre-processing activities that we come across in almost all imaging applications. Apparently, these two requirements contradict each other as one is a complement of the other. The image restoration aims at smoothing out the signal to reduce the noise interventions. On the other hand, enhancement seeks for an image with non-smooth features. Therefore, one should aim for a trade-off between these two requirements when providing a solution. Perceptually inspired frameworks have taken a considerable lead in image restoration and enhancement activities, as they seek for a visually appealing solution in addition to their excellent performance in terms of statistical quantifications. Retinex framework is being explored extensively in the literature to provide the desired enhancement to the images under consideration. This thesis provides an in-depth insight into various restoration frameworks and contributes a set of state-of-the-art restoration and enhancement models to assist the preprocessing step of various imaging applications with specific relevance to satellite and medical imaging. The degradation analysis is the primary step in an automated restoration framework. As one cannot apply a blanket restoration model for all kinds of distortions, the appropriate models are designed in due respect to the noise distribution of the input data. The second chapter of the thesis contributes a fully automated framework for analysing and detecting the noise distribution of the noise from input data. Analysis of noise distribution duly provides an insight to choose appropriate variational model to restore the images from the specific degradation analysed therein. A machine learning approach is employed to analyse the noise distribution from the input image characteristics. Various statistical and geometric features of the images are analysed to arrive at the conclusion regarding the distribution. Subsequent to the noise distribution analysis, the respective retinex based variational models are chosen to restore and enhance the images. One of the major issues with the variational models is that, they converge slowly when explicit numerical schemes are used for solving them. Many models designed under this framework use the explicit schemes due to the ease of implementation. Fast numerical implementations are one of the requirements of a real-time application model. This thesis investigates some of the fast numerical schemes such as Bregman iteration scheme redesigned for the problem under consideration to effectively solve the problems. Moreover, the computational cost is a major matter for

concern among the scientists, as most of the practically viable systems should be computationally efficient to be used under a real-time scenario. This thesis addresses this issue considerably well by employing parallel computing algorithms designed to be executed under multi-processing environments to improve the computational efficiency of the model.

Keywords: Perceptually inspired model, Retinex framework, Variational restoration models, Data-correlated noise, Image enhancement, Satellite and medical image enhancement.

Table of Contents

List of Figures

List of Tables

x

List of Notations

I	Original image (Intensity matrix)
I_0	Observed image
n	noise of any type
$I(x,y)$	Intensity of I at the location x and y
R	Reflectance matrix
L	Illumination matrix
i	Log of Intensity
r	Log of Reflectance
l	Log of Illumination
∇	Gradient operator
Δ	Laplacian matrix
$|.|$	Absolute value
$\prod$	Product
$\sum$	Summation
Ω	Image Domain
∂	Partial derivative
$T(x)$	Normalizing factor for w(x,y)
$D_{KL}(X||Y)$	KL divergence from distribution X to Y
$JSD(X||Y)$	JS divergence between distributions X and Y
$\nabla_{NL}I(x,y)$	Non-Local gradient for pair of pixels x and y
$\phi(.)$	Level set function
G_σ	Gaussian kernel with standard deviation σ

exp	Exponential
$P(z)$	Probability of z
μ	Mean
σ	Standard Deviation
σ^2	Variance
$*$	Convolution operator
$K_r bf(z, z')$	Radial basis function for data z and support vector z'
$\| x_j - y_j \|$	Euclidean distance between x_j and y_j
z	A random variable
e	Exponential
λ_p	Poisson noise variance
s	Shape parameter of Gamma noise
θ	Scale parameter of Gamma noise
I_{xx}	Second derivative of I in horizontal direction
I_{yy}	Second derivative of I in vertical direction
I_t	Temporal derivative of I
c	Coefficient of diffusion
$E(I)$	Energy functional
$w(x, y)$	Weight calculated between pixels x and y
$H(z)$	Entropy of z
$s_k(z)$	Skewness of z
$k_u(z)$	Kurtosis of z

List of Abbreviations

PDF	Probability Density Function
KL	Kullback-Leibler
NLTV	Non-Local Total Variation Minimization
PSNR	Peak Signal to Noise Ratio
MSE	Mean Square Error
MAP	Maximum A Posteriori
BV	Bounded Variations
SVM	Support Vector Machine
RBF	Radial Basis Function
NLTBV	Non-Local Total Bounded Variation
SB	Split Bregman
SAR	Synthetic Aperture Radar
US	Ultrasound
TV	Total Variation
MLE	Maximum Likelihood Estimator
NLM	Non-Local Means
TBV	Total Bounded Variation
CT	Computed Tomography
PET	Positron Emission Tomography
BTV	Bounded Total Variation
HYDICE	Hyperspectral Digital Imagery Collection Experiment
RESM	Ratio-based Edge Strength Map
RAG	Region Adjacency Graph
NNG	Nearest Neighbor Graph
KLD	KL divergence

JS	Jensen-Shannon
JSD	JS divergence
HE	Histogram Equalization
MSR	Multi-Scale Retinex
HSV	Hue Saturation Value
GCF	Global Contrast Factor
SVD	Singular Value Decomposition
DCT	Discrete Cosine Transform
DWT	Discrete Wavelet Transform
AG	Average Gradient
NIQE	Naturalness Image Quality Evaluator
GCF	Global Contrast Factor
CCA	Common Carotid Artery
SNR	Signal to Noise Ratio
ENL	Equivalent Number of Looks
ROI	Region Of Interests
CNR	Contrast Noise Ratio
AVIRIS	Airborne Visible InfraRed Imaging Spectrometer
SM	Streaming Multiprocessors
MMD	Maximum Mean Discrepancy
BLIINDS	BLind Image Integrity Notator using DCT Statistics
RCBLP	Relative Common Boundary Length Penalty

CHAPTER 1

Introduction

Remote sensing and medical imaging technology has witnessed tremendous improvements in the quality of captured images due to various enhancements applied to them during capture or post capture phases. Nevertheless, the images are still far away from providing a foolproof analysis due to various reasons. The main factors that contribute to the spurious analysis are; noise, device artefacts and contrast degradations present in captured data. In general, images are formed by sensing the signals reflected back from the imaging object. In medical imaging domain, for creating different scan results, experts make use of ultrasound waves, X-rays, radio waves, magnets, tracers etc. Similarly, in remote sensing, different bands of electromagnetic signals are being used for creating corresponding images. All these images are formed under various surrounding conditions. Hence the signals used for imaging gets attenuated or scattered which eventually leads to errors and degradations in the final image Zamperoni (2013). Moreover, the sensors used for imaging also contribute to the distortion scenario. As the images are formed in different ways in various imaging modalities, the distortion that occurs in them are also not uniform in nature. For instance, the Synthetic Aperture Radar (SAR) images are formed by capturing the reflections of microwave signals sent to probe the details of the object on Earth's surface. During the transmission or return, these waves undergo constructive or destructive interferences causing undesired features in the captured data Demirel et al. (2010). The waveforms thus captured are observed to be distorted and therefore need to be restored before subjecting them to any kind of analysis, else may result in spurious inferences. So is the case with medical data. Many medical imaging modalities also suffer from various distortions, despite of

the fact that the devices have become more sophisticated over the years. Therefore, the images captured are susceptible to various distortions which hampers the further analysis of data in several applications. This has been a major concern of the imaging and image processing community for decades altogether.

Though various restoration models are proposed over the years, they have their own merits and demerits. None of them are efficient enough to tackle different distortions uniformly. Moreover, the image restoration and enhancement are two complementary requirements. As we try to refine one, the other becomes coarse. Furthermore, restoration is an ill-posed problem whose solution may not be unique even if one exists and the uniqueness does not guarantee a continuous dependence of data on the solution. Therefore, one cannot guarantee a regular solution to such ill-posed problems in an obvious manner Hadamard and Morse (1953). Therefore, achieving a regular solution to such conflicting requirements is practically tedious. The detailed degradation aspects in the images are discussed in the sections to follow.

1.1 Image degradations

Image degradations are mainly due to the noise interferences, intensity inhomogeneity or contrast unevenness and equipment defects during data capture. The device artefacts are deterministic and can be modeled mathematically. The common artefact includes blur. The blurring artefacts causes the sharp details to be hardly distinguishable. There are various resolutions proposed for this defect, including improving the devise capabilities to enhance the images during capture or perform a post processing of stored data. Nevertheless, it is not a matter of major concerns for the imaging community as it can be addressed to a considerable extent. Noise and intensity or contrast unevenness is one of the major causes of misinterpretation of the data in later phases. The images represent different information, therefore, noise does not necessarily mean an unimportant information as it names to be. Therefore, denoising is a critical preprocessing step in image analysis phase. Since, noise is a non-deterministic quantity, it has to be modeled as a random process. The noise being a random variable, it follows a particular noise distribution. The noise intervention results in various noise distortions in terms of their

2

(a)   (b)
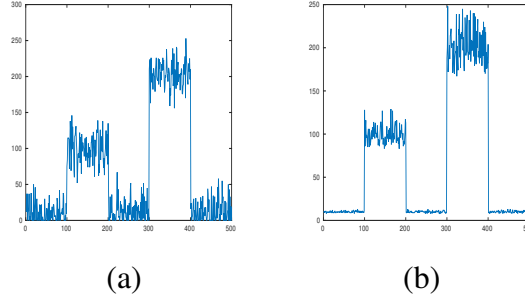
Figure 1.1 Noisy 1D signals (a) Data independent (b)Data dependent

distribution. The common assumption on the distribution includes an average white Gaussian noise, Gamma distributed noise, Poisson noise etc.

1.1.1 Noise models

Based on how noises interact with the image intensity, it can be classified into either data independent or dependent. In Figure 1.1(b), the noise intensity increases as the amplitude of the signal increases, this implies signal dependent nature of the noise, whereas, in sub-figure (a), noise intensity is constant and does not vary according to the signal amplitude. Additive noise like white Gaussian or thermal is considered as data independent Zamperoni (2013). If I_0 is a given noisy image, and n the noise and I the actual data, then an additive noise in an image is modeled as follows:

$$I_0(x) = I(x) + n(x), \qquad (1.1.1)$$

where x represents the spatial coordinates of pixels in an image. If the noise is assumed to be generated due to a random process and the number of such samples are large, then based on the central limit theorem, the samples follow a Gaussian distribution. This is the most common type of noise model and seen in images as thermal or sensor noise. A test image with additive noise is given in Figure1.2(a) and the histogram of the highlighted homogeneous region is given in sub-figure(b), where the Gaussian Probability Density Function (PDF) shows a better fit. The PDF (Hogg and Craig, 1970) for the Gaussian noise is given by,

$$G(z) = \frac{1}{\sigma\sqrt{2\pi}} e^{\frac{(z-\mu)^2}{2\sigma^2}}, \qquad (1.1.2)$$

where z is any real value $(0, \infty)$, μ is the mean and σ is the standard deviation.

If the noise is correlated to the data itself, then they are generally categorized as

3
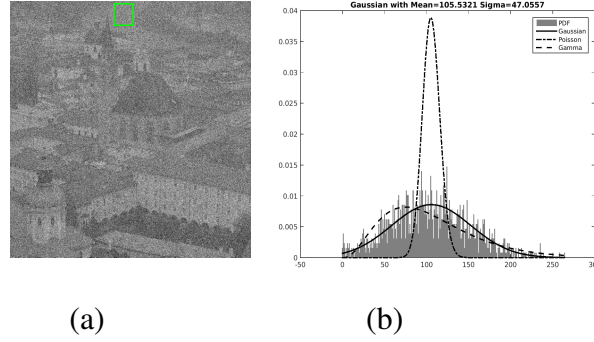
Figure 1.2 (a) Gaussian Noisy image with homogeneous area marked in Green. (b) Fitting of Gaussian, Poisson and Gamma distributions on the data.
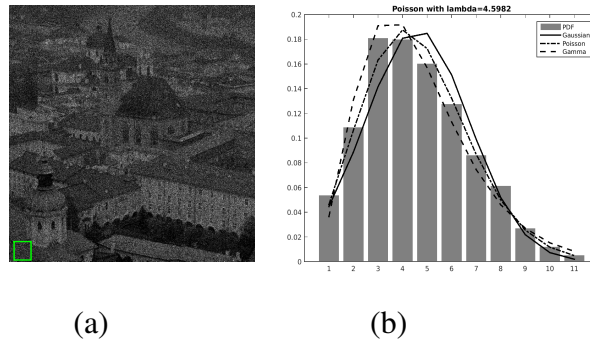
Figure 1.3 (a) Poisson Noisy image with homogeneous area marked in Green. (b) Fitting of Gaussian, Poisson and Gamma distributions on the data.

data-dependent. Noises like multiplicative Gaussian, Gamma and Poisson are regarded under this category of distortions. Satellite and medical images are usually affected by these kinds of noises and their removal is comparatively tedious. A multiplicative noise is modeled as given below:

$$I_0(x) = I(x)n(x). \tag{1.1.3}$$

Gamma and Rayleigh noises are observed to follow the above model.

Poisson noise is commonly seen in PET scans or satellite images and it is formed as a result of a Poisson process (Luisier et al., 2011). A test image with Poisson noise is given in Figure1.3(a) and the histogram of the highlighted homogeneous region is given in sub-figure(b), where the Poisson PDF shows a better fit. The Poisson distribution with parameters mean and variance λ_p is given by,

$$P_{\lambda_p}(z) = \frac{e^{\lambda_p}\lambda_p^z}{z!}, z \geq 0. \tag{1.1.4}$$

4
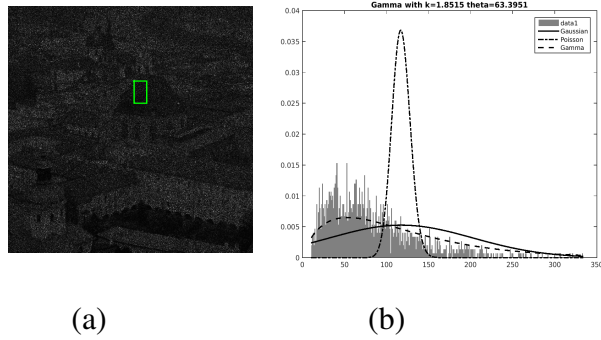
Figure 1.4 (a) Gamma Noisy image with homogeneous area marked in Green. (b) Fitting of Gaussian, Poisson and Gamma distributions on the data.

Gamma noise is commonly seen in the radar and ultrasound images (Zamperoni, 2013). Gamma noise is usually multiplicative in nature and follows the model given in (1.1.3). A test image with Gamma noise is given in Figure1.4(a) and the histogram of the highlighted homogeneous region is given in sub-figure(b), where the Gamma PDF is shown to fit better. The distribution is given by,

$$P_{s,\theta}(z) = \frac{z^{s-1}}{\theta^s \Gamma(s)} exp\left(-\frac{z}{\theta}\right), \tag{1.1.5}$$

where s is the shape parameter, θ is the scale parameter, mean $\mu = \frac{s}{\theta}$ and variance is $\sigma^2 = \frac{s}{\theta^2}$.

1.1.2 Degradations in satellite/remote sensing images

Remote-sensing is the process of obtaining information about an object or a process without directly contacting the same. It has wide range of applications in environmental studies and monitoring. Generally, the remote sensing can be airborne or space-borne. Satellites are used for space-borne remote sensing. Whereas, airborne sensors are mounted on space crafts to capture images (Schowengerdt, 2007). Remote sensing includes SAR (Synthetic Aperture Radar), Multi-spectral, and Hyper-spectral images. The areal images are also quite popular in remote sensing domain and mostly it uses airborne sensors or cameras for its capture. This is relatively an old remote sensing technique and widely popular due to the high resolution of the captured data. However, it is more expensive to cover a large area of study (Schowengerdt, 2007). A remote sensing system can be either active or passive in nature based on whether it uses external energy

source or not (Schowengerdt, 2007). Passive techniques measure the reflections of light or infrared radiations for imaging purpose. In case of SAR images, microwave signals are used for imaging whereas, multi and hyper-spectral images make use of a band of electromagnetic radiations for their representation.

Remote sensing forms images of distant objects, hence the electromagnetic radiations have to travel a long distance through the atmosphere to reach the sensor. Different atmospheric conditions like aerosols, gases, ice crystals etc., causes scattering and absorption of signals and results in low contrast and noisy image representations. Moreover, sensors themselves interfere with the received signals to degrade them with thermal noise and shot noise (Zamperoni, 2013). Even though the sensors are capable of recording a wide range of intensity variations, in most cases the reflected signals gets skewed to a narrow range, making the resultant image contrast deficient. As a result of this, contrast enhancement and denoising are the inevitable key operations in remote sensing domain.

1.1.3 Degradations in medical images

In medical imaging domain, scan images are heavily used for diagnosing the diseases. Based on the characteristics of the imaging organ, different modalities are used which include Ultrasound, Computed Tomography (CT), Positron Emission Tomography (PET) etc., (see Damerjiana et al. (2014)). In case of CT scan images, change in absorption of X-rays is recorded. In a human body, bones and different tissues respond to X-rays differently and if this change in absorption is not significant then the scan results will be low in contrast. Whereas, PET scan imaging is done by injecting a radioactive tracer that emits positrons into the patients body. This emitted positrons interacts with electrons in the body and end up in emitting gamma rays. Later, Gamma cameras are used for generating the scan results. Both CT and PET scan images are affected by the missing X-rays or Gamma rays, which eventually degrades the scan result. This is generally modeled using a Poisson process or yields a data dependent Poisson noise.

Ultrasound scanning is a well known technique due to the lack of ionizing radiations (Damerjiana et al., 2014). It is extensively used in gynaecology, cardiovascular study and so on. Real-time ultrasound imaging is also popular in studying development of

foetus. Ultrasound beams passing through a patient's body gets reflected, refracted, or scattered during its passage. When the passing wave encounters a difference in acoustic properties, a portion of the wave gets reflected and will be recorded. The ultrasound beam also gets attenuated as they travel through the body, hence the beams reflected from deep tissues will be less in intensity. Scattering of this wave occurs when the signal strikes objects of size same or smaller than its wavelength (Damerjiana et al., 2014). The constructive and destructive interferences of the scattered signals form speckle noises in the resultant image. The echo imaging technique used in ultrasound is similar to the radar based imaging, hence the presence of speckle noise is also common in both the cases. The speckle noises are multiplicative in nature and it degrades the quality and contrast of the scan result. Resultantly, ultrasound scan images are grainy and low in contrast which needs proper enhancement and restoration for accurate analysis (Moreira et al., 2013).

1.2 Restoration models

Given certain prior information such as the degradation scenario and the noise characteristics such as distribution of the random variable, image restoration aims to retrieve the approximation of the original image from its distorted version. As stated before, given the degradation model as additive with Gaussian distributed noise intervention, one can model it as

$$I_0(x) = I(x) + n(x), \tag{1.2.1}$$

here I is the original image and I_0 is the observed distorted image and n is the noise following a Gaussian distribution with zero mean (μ) and noise variance σ^2. All denoising models tend to reduce the fluctuations in the data in order to reduce the noise. The pioneer denoising models perform this task by averaging near by pixels. The common averaging filters reduce the noise by subsidizing the intensity variations. The linear heat kernel is a good example. The solution to a linear heat equation is a convolution with heat/Gaussian kernel with a specified standard deviation. As the time progresses, the diffusion spreads isotropically to more intensity pixels around the central one and results in fading of intensity variations (Aubert and Kornprobst, 2006). However, such

a denoising is undesirable in many imaging applications as the images themselves contain various features that contributes to the intensity fluctuations whose removal could result in serious setbacks during the image analysis phase. A linear diffusion model takes the form:

$$I_t = c(I_{xx} + I_{yy}), \tag{1.2.2}$$

where I_t is time derivative of the image function I and I_{xx} and I_{yy} are the second order space derivatives of I, and c is the coefficient of diffusion which is a constant here. Therefore, selective smoothing models were introduced in the literature. Non-linear diffusion model or anisotropic diffusion model has set a good example in this regime (Aubert and Kornprobst, 2006). The introduction of anisotropic models in image processing is attributed to Perona-Malik model (Perona and Malik, 1990). This is a well known non-linear diffusion model whose diffusion coefficient is controlled by a non-linear function of image gradient. Anisotropic model introduced in (Perona and Malik, 1990) is

$$I_t = \nabla.(c(|\nabla I|)\nabla I), \tag{1.2.3}$$

where ∇I is the gradient field of I and $\nabla.$ is the divergence function. Here $c(|\nabla I|) = 1/1 + (|\nabla I|/k)^2$ is the coefficient of diffusion which is a function of the gradient magnitude. The magnitude of diffusion is controlled by the diffusion coefficient whose value is (0,1]. It takes the value 1 when the gradient magnitude is close to zero and approaches zero when magnitude is very high. Therefore, high gradient points such as edges and discontinuities are preserved in the course of evolution whereas, the noise features are eliminated only from low-gradient regions. This is one of the notable setbacks of the non-linear diffusion model. There were many modifications suggested for this model by various researchers in the literature (Marquina and Osher, 2000; Lee and Seo, 2005) etc.

Apart from anisotropic models, there are scale-space models proposed for image restoration. Wavelet models are quite well known in this category (Xizhi, 2008). The wavelet models transform the image to a spatio-frequency domain and perform thresholding to reduce the noise intervention. Both, soft and hard thresholding methods are employed therein. Finding an appropriate threshold for the restoration is a tedious task.

In later works, curvelets were also used for image restoration (Jean-Luc Starck et al., 2002). Another noticeable set of scale-space models categorically falls under Stockwell transform (or s-transform) (Parolai, 2009). These models are well known for multi-resolution image processing. However, they apparently work well with Gaussian or random noise.

Another promising improvement in the image restoration literature is introduction of variational models (Tikhonov and Arsenin, 1977; Rudin et al., 1992). The variational models derive the concepts from penalization theory. The variational models are quite efficient in defining the restoration framework. The models helps us to study the theoretical aspects of the model such as existence, uniqueness and stability of the solution. We are dealing with ill-posed inverse problems for which solutions are not trivial. As stated before, in case of the ill-posed problems, the solution may not exist or even if the solutions exist, it may not be unique and may not depend on the data continuously. In other words, small perturbations in the data may lead to large ones in the solution. Therefore, a regularization framework serves as an appropriate model to define the solution for an ill-posed inverse problem. This is the one of the motivations for employing regularization frameworks in the present study. Apart from providing a platform for performing a detailed theoretical analysis, variational models have various other advantages. For instance, in variational regularization framework, one can redefine the model to handle various noise distributions in the data (Aubert and Aujol, 2008; Le et al., 2007; Kayyar and Jidesh, 2018). Fast numerical solvers which are less sensitive to the parameters can also be used for the solution of the model. Therefore, variational models captured the attention of scientists in various imaging disciplines.

The penalization theory defines a optimization function with a regularization and data fidelity term.

$$E(I) = \min_{I} \|I\|_2^2 + \lambda (I - I_0)^2, \tag{1.2.4}$$

this is a L^2 regularization problem where $\|I\|_2^2$ is the L^2 norm of I. The data fidelity term $(I - I_0)^2$ is the squared error term and λ is the regularization parameter $(0, \infty)$. So, the above model is a squared error minimization model or minimum mean square error model. The solution is defined in L^2 space where the functions are normally smoother.

Therefore, the solution fails to retain edges and details present in the input.

Driven by the penalization theory, a pioneer model in the regularization framework was proposed in Tikhonov and Arsenin (1977). This model is well known by the name Tikhonov regularization model is defined as:

$$E(I) = \min_I \|\nabla I\|_2^2 + \lambda (I - I_0)^2, \tag{1.2.5}$$

where ∇I denotes the gradient field of I and the other terms have their usual meaning. The minimization yields smoother versions of I and the solution is defined in the space of square integrable functions (L^2 space) and as mentioned before this space does not admit discontinuities in the solution, leading to smoother versions of the input image. Therefore, Tikhonov model is not effective in restoring images with discontinuities as many of them seems to be.

Total variation (TV) regularization is an improvement of the above mentioned one (Rudin et al., 1992), in terms of retention of image features such as edges and details. The total variation is defined as $\int_\Omega |\nabla I| d\Omega$, where ∇ denotes the gradient vector, $|.|$ denotes the L^1 norm or the normal magnitude function. The TV regularization is

$$E(I) = \min_I \int_\Omega \{|\nabla I| + \lambda (I - I_0)^2\} d\Omega. \tag{1.2.6}$$

The solution is defined in the space of bounded variation where the variations are bounded. The BV space is defined as $BV(\Omega) = \int_\Omega |\nabla I| d\Omega < \infty$, where all cumulative variations are bounded. The space admits discontinuities which makes the space suitable for image restoration in case of images with details. However, the TV regularization discussed above is designed based on the assumption that the noise is random and data-uncorrelated. The model is derived using a Bayesian framework by assuming the prior and the likelihood. The data-fidelity term is directly derived from the distribution of the likelihood function. The Bayesian formulation takes the form:

$$P(I|I_0) = \frac{P(I_0|I)P(I)}{P(I_0)}, \tag{1.2.7}$$

where $P(I|I_0)$ is the conditional probability and it is generally called the posterior probability. That is, the probability of occurrence of the event I given I_0. In this case, the symbols I and I_0 denotes original and observed images respectively, the posteriori estimate tries to find the conditional probability of I (the probability of the approximation being close to the original one) given the distorted image I_0. So, maximizing the poste-

rior estimate reduces the approximation error or eventually we get the resultant image pretty close to the original one. The term $P(I)$ denotes the prior assumption and $P(I_0|I)$ is the likelihood probability. The likelihood estimate approaches the posterior estimate when the prior probability is constant. Here we observe that the likelihood follows distribution of the noise. So, for restoring images corrupted with the Gaussian noise, one should assume the probability distribution of the likelihood as Gaussian. The TV functional in (1.2.6) is derived using the Bayesian formulation assuming the noise as Gaussian and the prior as TV. See Appendix A for the detailed derivation.

Apart from TV regularization there were quite a few other regularization models proposed in the literature (see Marquina and Osher (2000); Aubert and Aujol (2008)). Many of therm are marginal variations in the regularization prior. For instance, in Liu and Huang (2010) instead of TV prior the authors propose a Bounded Total Variation (BTV) prior and claims that the model preserves details better compared to the TV model. In additions to the variations in the regularization term, there are proposals which modify the data fidelity terms to incorporate the distribution of the noise present in the data. As observed in the literature, a model designed for Gaussian noise does not necessarily perform well with another noise distribution such as Gamma or Poisson. Therefore, the researchers have studied various variational frameworks to handle different noise distribution in the data. The model in Aubert and Aujol (2008) assumes Gamma noise in the input while designing the model, on the other hand, in Le et al. (2007), the authors assume a Poisson distributed noise (or the noise is generated as an aftermath of a Poisson process) and so on. In these models, the authors derive the framework based on the Bayesian model by assuming that the likelihood follows the distribution of noise present in the data.

The non-local framework was a considerable improvement in the image restoration literature (Buades et al., 2005). Motivated by the non-local means (Buades et al., 2005), Gilboa et al. (Gilboa and Osher, 2008) introduced a non-local variational regularization model. Unlike the local variational models, the non-local models are observed to work well with the image details and they preserve them well. In a non-local framework, the similarity function is defined in terms of a negative exponential. The weighted

averaging is performed where the weight is a function of the similarity measure. The patches having high similarity will participate in the averaging process whereas, the patches with low similarity refrain from the averaging process. This eventually helps in averaging the similar patches which are even located apart from each other. Whereas, in local averaging only the nearby pixels take part in the averaging process. The non-local gradient of a function I, for a pair of points or pixels (x,y) is defined as,

$$\nabla_{NL}I(x,y) = (I(y) - I(x))\sqrt{w(x,y)}, \qquad (1.2.8)$$

where $w(x,y)$ is the weight between x and y, and $w(x,y)$ is calculated as

$$w(x,y) = \frac{1}{T(x)}e^{-\frac{(G_\sigma * |v(N_x) - v(N_y)|^2)}{h^2}}, \qquad (1.2.9)$$

where

$$T(x) = \int_{y\in\Omega} e^{-\frac{(G_\sigma * |v(N_x) - v(N_y)|^2)}{h^2}} dy,$$

and N_x denotes a square neighborhood of fixed size and centered at a pixel x and similarly for y, G_σ is Gaussian blurring kernel, and h is a filtering parameter. There are some variations to non-local averaging as well in the literature. A bi-lateral filtering is a good example (Patil and Kumbhar, 2015; Zhang and Allebach, 2008). This filter performs averaging based on spatial and radiometric similarity. The exponential function defining the similarity is based on both spatial similarity and radiometric similarity. The spatial similarity or spatiometric distance decreases as the spatial distance of the patches increases. In other words, the spatiometric similarity is inversely proportional to the spatial distance between the patches. The radiometric similarity depends only on the intensity values. If the intensity values are similar in a patch, they tend to have high radiometric similarity. Non-local variational models were modified to handle different noise distributions in the data as well. In Kayyar and Jidesh (2018), the authors designed a model to handle Poisson noise. Similarly, in Jidesh and Balaji (2018); Holla and Jidesh (2018), authors developed models that can handle Gamma and Rayleigh noise. In Jidesh and Holla (2018), the authors propose a model to handle MR data corrupted by Rice and Chi noise distribution.

Perceptual driven models are introduced for enhancing images with intensity inhomogeneity or contrast deficiency. The retinex framework redefines the image function

in terms of intensity, luminance and reflectance.

$$I = L \times R, \tag{1.2.10}$$

where I, L, and R are intensity, illumination and reflectance respectively. Here reflectance is the property of the object on which the light falls and intensity and illumination are related to the light source. Retinex based methods are popular in enhancing images in various domains like remote sensing (Huifang Li and Shen 2012), underwater imaging (Zhang et al. 2017), medical imaging (Setty et al. 2016), microscopic imaging (Mohamed et al. 2017) etc.

1.3 Dataset

For experimental studies, we have used publically available hyperspectral datasets such as Indian Pines, Jasper Ridge (courtesy, Pursues university MultiSpec), and Cuprite (courtesy, AVIRIS NASA). All these images are obtained using AVIRIS (Airborne Visible InfraRed Imaging Spectrometer) sensor and includes 224 spectral bands in the range of wavelength 400 to 2500 nanometers. The Indian Pines dataset includes images of size 145×145 and the Cuprite data images are of size 250×190 pixels. In the case of the Jasper Ridge, the original image size is 512×614 pixels, but we are using only a 100×100 sub-image of the same. Moreover, the Washington DC data (courtesy, Pursues university MultiSpec) obtained using HYDICE (Hyperspectral Digital Imagery Collection Experiment) sensor has also been used in our experimental study. It includes 210 spectral bands in the wavelength range same as AVIRIS. The size of the data is 1208×307. In addition to the hyperspectral images, some aerial images are also been used in the comparative analysis. We have used the publicly available Massachusetts Buildings Dataset (http://www.cs.toronto.edu/ vmnih/data/), which is a collection of aerial images of Boston city in the USA. Each of these images is of size 1500×1500 pixels. A satellite-based overhead object detection data called xView (http://xviewdataset.org/dataset) has also been included in our analysis. It contains high-resolution images collected by using WorldView-3 satellites. Further, for the speckle-noise study, we are using B-mode ultrasound images of the common carotid artery (CCA) (courtesy, Signal Processing Laboratory, Czech Republic:

http://splab.cz/en). These images are of resolution 390×330 pixels and two linear transducers of frequencies 10MHz and 14MHz were used to capture the same.

1.4 Motivation

A generalized framework for restoring and enhancing images from multiple imaging domains is not explored much the in literature. Such a framework has enormous applications in the contemporary imaging science. As most of the imaging modalities produce distorted images, their analysis demands an efficient pre-processing step. Satellite and medical imaging applications analyze a large number of images for various studies. Moreover, these modalities produce distorted images despite of the quality of devices used for image acquisition. The distortions in the captured data in these modalities are unique and depends on the characteristics of the modality under which the images are formed. Though there are models designed for restoration in each of these modalities, they tend to address one of the distortions for which it is designed. There lacks a common framework which handles different kinds of distortions while performing an enhancement to them. This thesis intents to bridge this gap by providing a common framework for medical and satellite imaging application to restore and enhance the images corrupted with various kinds of distortions without affecting the prominent details required for their further analysis. Therefore, this designed framework can be plugged into the preprocessing step of various imaging applications. Moreover, the model thus designed will converge at a faster rate and would be computationally efficient so that it can be employed for images of bigger size as the ones that commonly appear in medical and satellite imaging applications.

1.5 Research Objectives

Image enhancement is an inevitable pre-processing activity in many of the image processing applications. The images captured are degraded during various stages of imaging and image processing. Image acquisition and storage are the two prominent stages which are prone to the degradation scenario. Since image enhancement and restoration is an ill-posed problem, its solution is not trivial. Various regularization frameworks

14

are to be employed for the design of an effective solution. Though there are a few approaches highlighted in the recent literature for enhancing and restoring images from satellite and medical imaging domain, they have their own pros and cons. Analysis of the noise distribution is another important requirement as far as the design of a restoration model is concerned. There are no blanket restoration models available to date to handle all kinds of noise distributions uniformly. So, analyzing the noise distributions from the input data is a crucial requirement in the design of an appropriate enhancement and restoration framework. The thesis addressees these issues to a considerable level. The overall objectives are highlighted below.

- Analyse and estimate the noise distribution and noise parameters of input images from medical and satellite imaging application using automated machine learning algorithms.

- Designing variational frameworks equipped with retinex models to enhance and restore various kinds of images corrupted by different noise distributions such as Gaussian, Poisson and Gamma.

- Analyse and study the model both theoretically and experimentally and compare with the state of the art restoration models.

- To enhance the computational efficiency of the models using fast numerical approaches such as Split-Bregman scheme in order to improve the convergence rate of the model.

- Further to improve the computational speed by parallelizing the algorithms to be executed under a multi-core processing environment such as GPU.

1.6 Organization and Contribution of the Thesis

The degradation analysis is the primary step in an automated restoration framework. As one cannot apply a common restoration model for all kinds of distortions, appropriate models are designed in due respect of the noise distribution of the input data. Chapter two of the thesis contributes a fully automated novel framework for analyzing and detecting the distribution of the noise from the input data. Analysis of noise distribution

15

duly provides an insight to choose appropriate variational model to restore the images from the specific degradation analysed therein. A machine learning approach is employed to analyse the noise distribution from the input image characteristics. Various statistical and geometric features of the images are studied to arrive at the conclusion regarding the distribution. Subsequent to the noise distribution analysis, the respective retinex based variational models are chosen to restore and enhance the images.

Third chapter highlights the model proposed for restoring and enhancing low contrast Gaussian noisy images from satellite imaging applications. As a matter of fact, many remote sensing images are low-contrast and noisy in nature, therefore, we intent to address these issues using a perceptually driven variational retinex framework under a non-local strategy.

Generally, noises present in remote sensing images can be categorized as data-independent thermal noise, stripping noise and data-dependent shot noise (Poisson noise). Removal of data-correlated noise like shot noise is comparatively challenging than the common data-independent counterparts. The noise distribution is analysed from the input image using the model described in Chapter 2. Subsequently, the fourth Chapter highlights a model proposed for restoring and enhancing low contrast and Poisson noisy satellite images.

Ultrasound images are very popular in medical domain and it commonly gets degraded due to speckle noise which in most of the literatures assumed to follow a Gamma distribution. In Chapter 5 a model for restoring ultrasound images is introduced. The model duly analyses the noise distribution in the data using the procedure discussed in Chapter 2 and designs a retinex based variational framework to enhance and restore the images.

The last chapter provides a conclusion of the thesis throwing some light on future enhancements. The models designed as a part of this thesis are implemented using C++ under parallel CUDA programming environment of NVIDIA GPU processor Tesla V100. This improves the overall computational efficiency of the model. The non-local variational frameworks deal with huge matrices, therefore, a sequential processing of the data is computationally demanding and consumes enormous CPU time. This was

considerably addressed in this thesis by employing parallel algorithms for processing the data. On the machines which does not possess the parallel computing facility, the models run under the sequential schemes without categorically demanding a specific platform for their computation. The users are to be least worried about the computing platform, as the model gives optimal results under different computing environments no matter whether the parallel computing environments are available or not. Some of the future enhancements being planned to undertake in order to further improvise the models studied herein has been discussed in this chapter.

Some of the bulky derivations and definitions are provided in Appendix A of the thesis.

CHAPTER 2

Degradation analysis from the data

2.1 Introduction

Noise is an unexpected intervention in an image and it gets included during its capture, transmission or processing. As mentioned earlier, presence of degradation such as noise restrict the proper information retrieval from an image, hence it is a major concern in image analysis. Removing noise from an image without losing the data is a tedious task and without prior information about the nature of noise, this can even cause blurring or loss of information. Resultantly, identifying the nature of noise is essential to perform an appropriate restoration of the degraded image.

Despite of its importance, noise classification is comparatively a less studied area and only a few initiatives are available on this topic. Many methods are proposed for estimating noise parameters and noise density from data, refer Liu et al. (2006), Liu et al. (2013), and Liu et al. (2014). However, these methods fail to analyze the noise distributions. Initial research on identifying the nature of noise was done in Chehdi and Sabri (1992), which is elaborated in Beaurepaire et al. (1997) by additionally analyzing local histograms. In Vozel et al. (2006), authors tried to recognize the additive or multiplicative noises by fitting a polynomial regression and Chen and Das (2007) uses existing filters like Weiner, homomorphic and median for estimating noise. In this Chapter, we propose a framework for identifying the nature of noise present in a degraded image. Noise can be classified into different categories based on its distribution.

Noise classification is a preliminary step in the regularization frameworks, which are popular in preserving details while restoring distorted images (Jidesh, 2014). Among
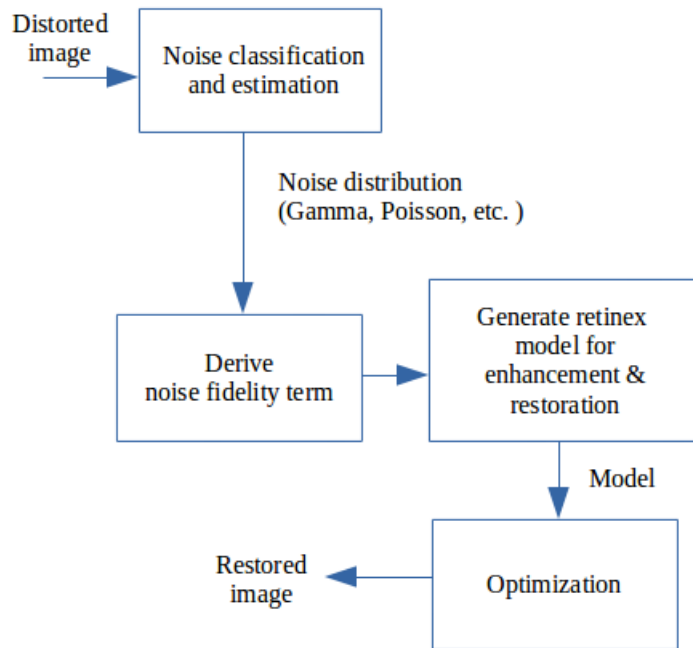
Figure 2.1 Automatic Restoration system

the regularization models, non-local algorithms have an edge over the others in terms of preserving local features like textures and details, see Antoni Buades and Morel (2005), Aubert and Aujol (2008), and Gilboa and Osher (2008) for the details. Many regularization algorithms are proposed for different image processing applications, see Lu et al. (2014) and Lu et al. (2013). Many among them, are designed specifically for a particular type of noise intervention in the data. For instance, Liu and Huang (2014), Le et al. (2007), and Jidesh and Balaji (2018) are designed for Gaussian, Poisson and Gamma noises, respectively. An adaptive framework which automatically chooses the best regularization algorithm based on noise characteristics and does enhancement and denoising will be handy to the end users who do not possess knowledge about the type degradations present in the data. The different noise distributions considered in this study are Gaussian, Poisson and Speckle following Gamma, as these are the most common type of noises present in remote sensing and medical imaging applications. The block diagram of the automated restoration system proposed in this Chapter is as in Figure 2.1. The details of noise classification and estimation module is elaborated

in the next section. The design and analysis of various restoration models under the variational framework for Gaussian, Poisson, Gamma noises are explained in Chapters 3, 4, and 5 respectively.

2.2 The proposed Methodology

The methodology adopted for automatic noise classification includes mainly three steps namely: Homogeneous region extraction, Feature extraction, and classification. Overall work-flow of the framework is given in Figure 2.2. The nature of noise can easily be analyzed if the intensity values are constant over the region. Hence, the first step towards automatic noise identification is the extraction of such homogeneous intensity regions within the image. Afterwards, the histogram of these uniform intensity regions provides an insight to the underlying noise distribution. However, automatically detecting the appropriate distribution from a list of possible outcomes is a tricky task and to address this issue we use a machine learning technique in this study. Feature extraction is the next important step, which in turn is the process of identifying features with high discrimination capability. After extracting the features, a classifier is designed accordingly to effectively classify the noise distribution.

2.2.1 Homogeneous region Extraction

Extracting homogeneous regions is an important step in noise analysis phase as in those areas, intensity values are almost constant and the variations are mainly due to the noise components. Homogeneous region extraction from a noisy input is a challenging task for which we have adopted a fast segmentation method based on region-merging technique (Shui and Zhang, 2014). In this method, a Ratio-based Edge Strength Map (RESM) is extracted from an input image which gets thresholded to reduce local minima inside the homogeneous regions. Afterwards, the watershed transform is applied on thresholded RESM to form the initial partition. Initial partitions always give an over-segmented result which again gets merged to form the final one by using a new cost function for merging with relative common boundary length penalty (RCBLP). To form a fast algorithm, region-merging is combined with region adjacency graph (RAG) to represent segmentation result and nearest neighbor graph (NNG) to do fast minimal

edge searching. Around thirty homogeneous regions are extracted from every input image in this study. Homogeneous region extracted from synthetic and real noisy images are given in Figures 2.3 and 2.4, respectively.

2.2.2 Feature Extraction

In case of noisy data, the histogram obtained from the homogeneous intensity region essentially follow the distribution of the noise present in it. Finding the similarity of this image PDF with different noise distributions provides an insight to the nature of the noise present in the image. For this purpose, Jensen-Shannon (JS) Divergence which is an extension of the popular Kullback-Leibler (KL) divergence is being used. Apart from JS divergence, skewness, kurtosis, entropy, and fifth central moment are evaluated to get the information about the shape and nature of the distribution. Along with these features, we have also extracted the steepness of mean-variance curve to distinguish between the additive and multiplicative nature of the noise.

JS Divergence:

It is a measure of dissimilarity between two distributions and it is considered as an extension of popular KL divergence (Menendez et al., 1997).

KL Divergence: It measures how one probability distribution differs from another one (Kullback and Leibler, 1952). This method was introduced by Solomon Kullback and Richard Leibler. The KL divergence from X to Y is generally denoted as $D_{KL}(X||Y)$, where X and Y denote two distributions. For a discrete case (i.e where probability distributions X and Y are discrete), D_{KL} is as shown below (Menendez et al., 1991)

$$D_{KL}(X||Y) = \sum_{x \in \Omega} X(x) log \frac{X(x)}{Y(x)} \tag{2.2.1}$$

and for the continuous case, it is defined as

$$D_{KL}(X||Y) = \int_{-\infty}^{+\infty} X(x) log \frac{X(x)}{Y(x)} dx \tag{2.2.2}$$

D_{KL} is a non-negative ($D_{KL}>=0$) and non-symmetric ($D_{KL}(X||Y) \neq D_{KL}(Y||X)$) measure. If two distributions are exactly similar, then D_{KL} approaches zero and it increases with the increase in dissimilarity. KL divergence is very closely related to relative en-
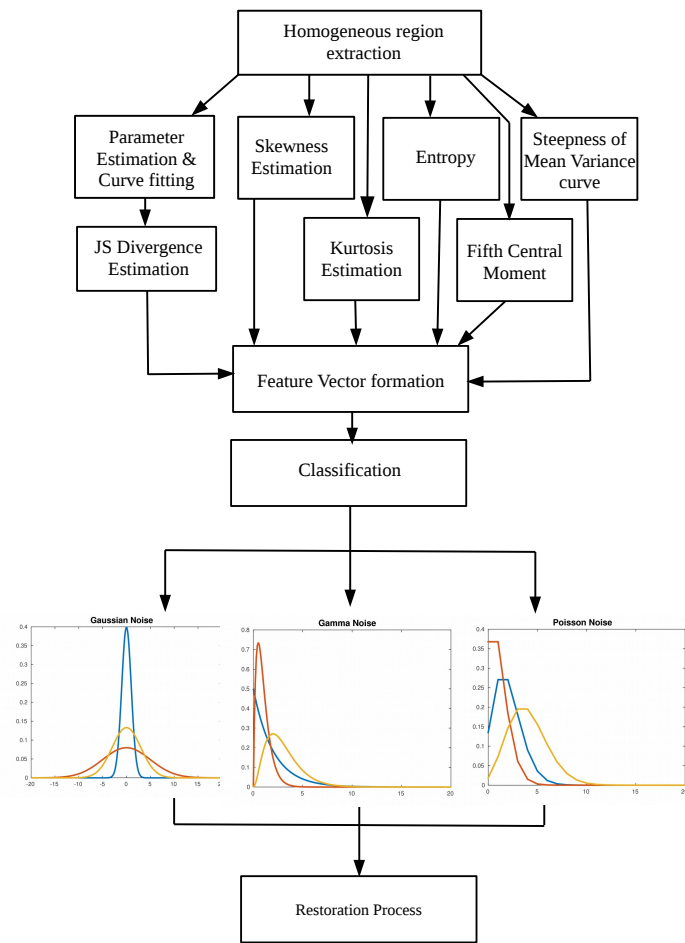
Figure 2.2 Overview of the Noise estimation and classification system

<div align="center">(a1)   (a2)   (a3)</div>

<div align="center">(b1)   (b2)   (b3)</div>

<div align="center">(c1)   (c2)   (c3)</div>
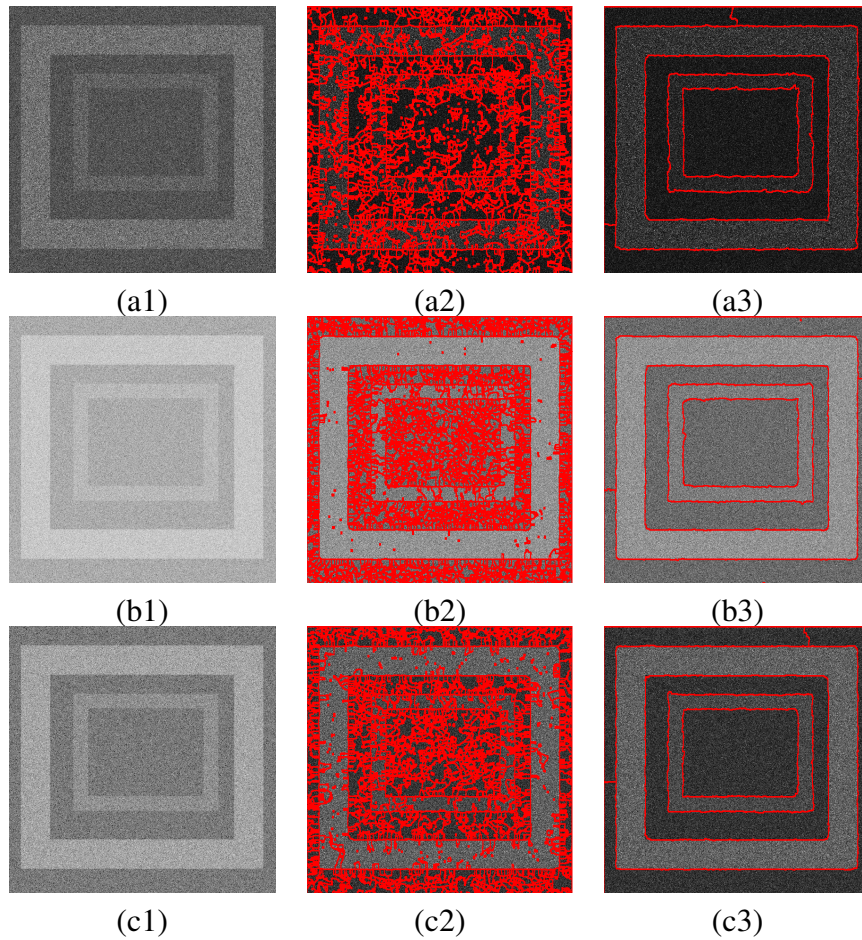
Figure 2.3 Homogeneous region extraction in a noisy synthetic image: Row 1: Image with Gamma Noise: (a1) Noisy image (a2) Initial partition (a3) Final segmented image; Row 2: Image with Gaussian noise: (b1) Noisy image (b2) Initial partition (b3) Final segmented image; Row 3: Image with Poisson noise: (c1) Noisy image (c2) Initial partition (c3) Final segmented image;
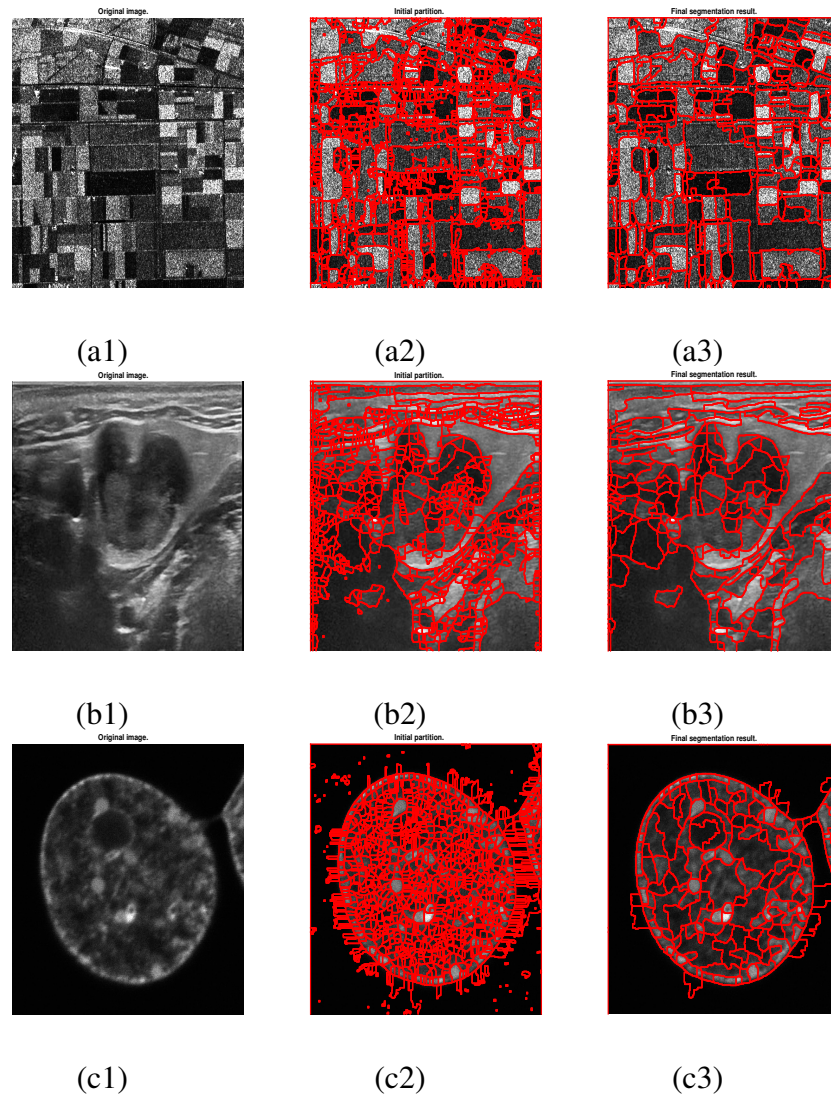
Figure 2.4 Homogeneous region extraction in real noisy images: Row 1: SAR image (Intensity AIRSAR image of Flevoland, Netherlands 500×500,HH polarization, four looks) : (a1) Noisy image (a2) Initial partition (a3) Final segmented image; Row 2: Ultrasound image (Pleomorphic adenoma in the submandibular gland,Courtesy of www.ultrasoundcases.info): (b1) Noisy image (b2) Initial partition (b3) Final segmented image; Row 3: Confocal Microscopic image (Mouse fibroblast cell, Courtesy of www.cellimagelibrary.org, doi:10.7295/W9CIL1315): (c1) Noisy image (c2) Initial partition (c3) Final segmented image;

tropy and $D_{KL}(X||Y)$ can be considered as the difference between the cross-entropy of X and Y ($H(X,Y)$) and the entropy of X ($H(X)$).

$$D_{KL}(X||Y) = H(X,Y) - H(X). \qquad (2.2.3)$$

Though JS divergence is defined based on KLD, it is a symmetric measure and it always gives a finite value. JS divergence is also measured as the total divergence to the average. JS divergence (JSD) is defined as follows (Fuglede and Topsoe, 2004).

$$JSD(X||Y) = \frac{1}{2}D_{KL}(X||M) + \frac{1}{2}D_{KL}(Y||M) \qquad (2.2.4)$$

where $M = \frac{1}{2}(X+Y)$ i.e,

$$JSD(X||Y) = \sum_{x \in \Omega} X(x) log \frac{X(x)}{\frac{1}{2}X(x) + \frac{1}{2}Y(x)} + \sum_{x \in \Omega} Y(x) log \frac{Y(x)}{\frac{1}{2}X(x) + \frac{1}{2}Y(x)}. \qquad (2.2.5)$$

Based on entropy it can be formulated as below

$$JSD(X,Y) = H(\frac{X+Y}{2}) - \frac{1}{2}H(X) - \frac{1}{2}H(Y). \qquad (2.2.6)$$

The general form is, $JSD(X,Y) = H(\pi_1 X + \pi_2 Y) - \pi_1 H(X) - \pi_2 H(Y)$ where π_1, π_2 are the weights for probabilities X and Y respectively. When there is more than two probability distributions (Menendez et al., 1991) then

$$JSD(X_1, X_2, ..., X_N) = H(\sum_{j=1}^{N} \pi_j X_j) - \sum_{j=1}^{N} \pi_j H(X_j). \qquad (2.2.7)$$

Skewness:

Skewness is the measure of asymmetry of the distribution (Doric et al., 2009), it is the third central standardized moment, which is also known as First Pearson's coefficient. Skewness S_k of random variable z can be defined as below

$$S_k = E\left[\left(\frac{z-\mu}{\sigma}\right)^3\right], \qquad (2.2.8)$$

where μ represents mean, E is the expectation operator and σ represents the standard deviation. In accordance with the asymmetry, one distribution can be positively or negatively skewed. Negative skewness indicates the long left side tail. Similarly, positive skewness indicates that the right side tail is longer. For positive skewness, median and mean of the distribution will appear on the right side of the Mode whereas, for negative skewness it appears on left side.

Normal distribution (Gaussian distribution) is always symmetric and consequently,
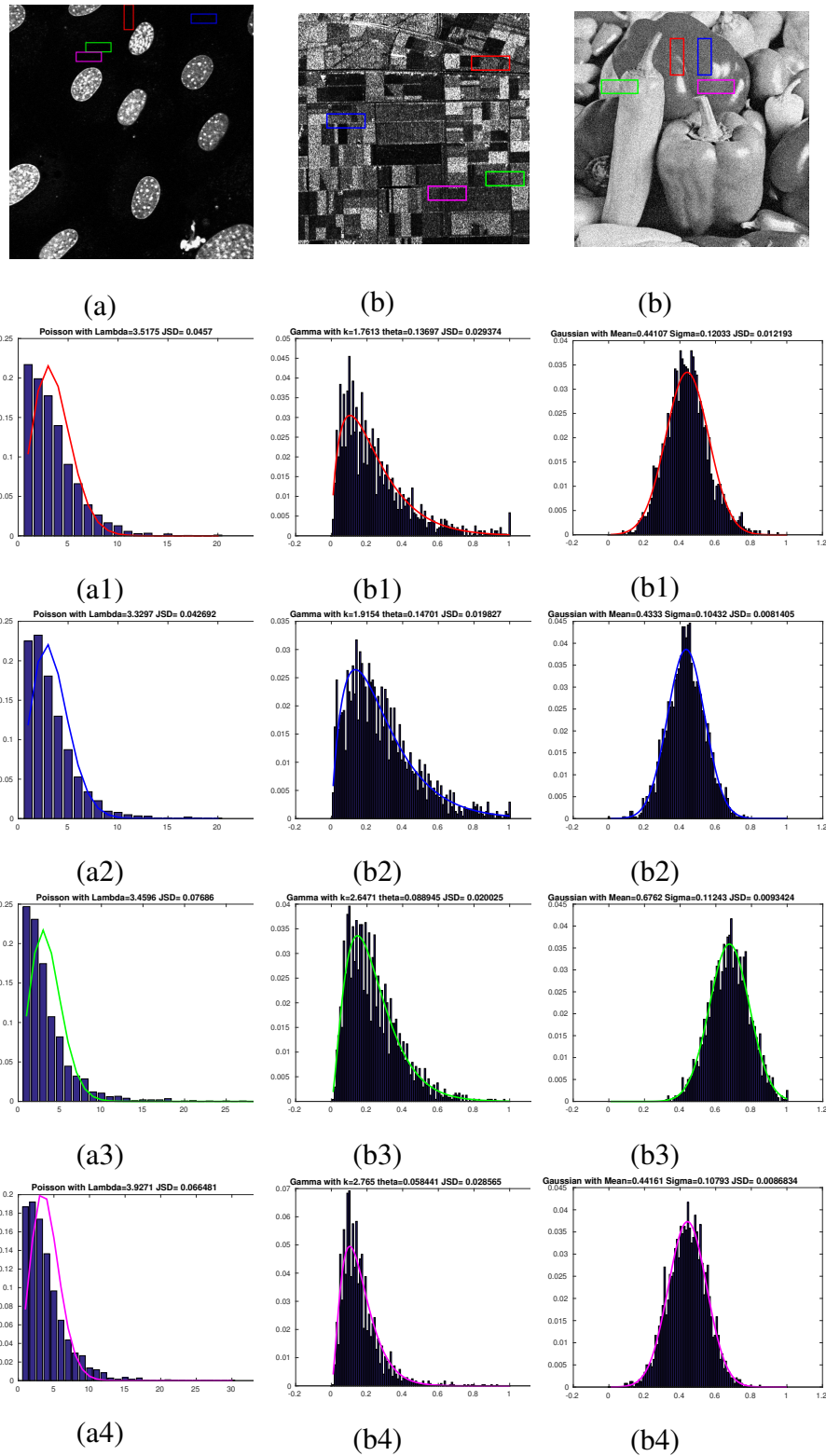
Figure 2.5 Fitting and JSD estimate on different noisy images Row 1: (a) Poisson noisy input (b) Speckle noisy input (c) Gaussian noisy input; Rows 2-5 : fitting on different homogeneous regions marked using the corresponding estimated parameters

its skewness value will be always close to zero. For Gamma distribution, the skewness is defined as below

$$S_{kGamma} = \frac{2}{\sqrt{s}} \tag{2.2.9}$$

where s is the shape parameter. As the value of s increases, skewness approaches to zero and the distribution tends close to a Gaussian.

For a Poisson distribution, skewness is defined as

$$S_{kPoisson} = \lambda_p^{-1/2} \tag{2.2.10}$$

here λ_p is the average number of events per interval.

Kurtosis:

Kurtosis is sometimes considered as the measure of peakedness, but it is more related to the tails of the distribution, hence it can be treated as a measure of "tailedness" of the probability distribution. It is the fourth standardized moment, popularly known as second Pearson's coefficient. Kurtosis K_u of random variable z is defined as

$$K_u = E\left[\left(\frac{z - \mu}{\sigma}\right)^4\right] \tag{2.2.11}$$

where μ represents mean, E is the expectation operator and σ represents the standard deviation.

The kurtosis of a popular normal distribution is 3. If kurtosis distributions is less than 3 it is known as platykurtic and those with kurtosis greater than 3 are called leptokurtic (Doric et al., 2009). Laplace distribution is an example for leptokurtic as its tail approaches zero more slowly. Kurtosis of a Gamma distribution is defined as

$$K_{uGamma} = 3 + \frac{6}{s} \tag{2.2.12}$$

where s is the shape parameter and as s approaches infinity, Kurtosis of Gamma distribution approaches three and subsequently, the distribution tends closer to a Normal (Gaussian) distribution. Kurtosis of the Poisson distribution is defined as

$$K_{uPoisson} = \lambda_p^{-1} \tag{2.2.13}$$

here λ_p is the average number of events per interval.

Entropy:

Entropy is the measure of unpredictability, it is also known as the average information content (Azzam and Awad, 1996). Entropy is measured as the negative logarithm of probability mass function, which means a less probable event contains more information or it carries more uncertainty. Entropy $H(z)$ for the discrete domain can be defined as below

$$H(z) = -\sum_{j=1}^{N} logP(z_j) \qquad (2.2.14)$$

The entropy of a Normal distribution is

$$H_{Normal} = \frac{1}{2}log(2\pi e\sigma^2) \qquad (2.2.15)$$

and for Gamma and Poisson distributions, entropy is as shown below (Azzam and Awad, 1996)

$$H_{Gamma} = s + ln\theta + ln\Gamma(s) + (1-s)\psi(s) \qquad (2.2.16)$$

where s and θ represents the shape and scale parameters of Gamma, Γ is the gamma function , and ψ denotes the digamma function.

$$H_{Poisson} = \lambda_p[1 - log(\lambda_p)] + e^{-\lambda_p} \sum_{k_p=o}^{\infty} \frac{\lambda_p^{k_p} log(k_p!)}{k_p!}, \qquad (2.2.17)$$

where k_p represents the number of occurrences of an event.

Fifth central moment (FCM):

Central Moment is the moment about the mean, and fifth central moment can be defined as below

$$FCM = E((z-\mu)^5). \qquad (2.2.18)$$

It acts as a measure of relative importance of tail versus Mode for causing the skewness.

The Steepness of Mean-Variance curve:

With reference to Chehdi and Sabri (1992), in a homogeneous region of an image (g_h), if the variance is constant then the noise present in it will be additive in nature and if the variance ($\sigma^2[g_h]$) according to the average($E[g_h]$) is a parabola passing through the origin, then it is more likely to be multiplicative in nature.

The noisy image can be expressed as $I_0 = I + n$ (in additive case). Therefore,

$$\sigma^2[I_0] = \sigma^2[I] + \sigma^2[n]. \qquad (2.2.19)$$

In a homogeneous region, $\sigma^2[g_h] = \sigma^2[n]$, where g_h indicates an observation relative to a homogeneous region. In case of multiplicative noise, $I_0 = I * n$, so,

$$\sigma^2[g_h] = E^2[g_h]\sigma^2[n]. \qquad (2.2.20)$$

This implies that the nature of the mean-variance curve, especially steepness of the curve will be different for different kind of noises. Thus steepness or slope of the mean-variance curve can be regarded as an important feature to distinguish additive noise like Gaussian from multiplicative noise like Gamma.

2.2.3 Classification

For classification, we have used multi-class Support Vector Machine (SVM) with RBF (Radial basis function) Kernel. SVM is a supervised learning technique which analyses the training data to build a model that later correctly categorizes the unknown testing inputs. In SVM, one can achieve a non-linear classification by using Kernel tricks (Cortes, 1995). An RBF Kernel on two samples z and $z^{'}$ is defined as

$$K_{rbf}(z, z^{'}) = e^{-\frac{\|z - z^{'}\|^2}{2\sigma^2}} \qquad (2.2.21)$$

where $\gamma^{'} = \frac{1}{2\sigma^2}$, therefore, it is also defined as $K_{rbf}(z, z^{'}) = e^{-\gamma^{'}\|z - z^{'}\|^2}$

Mostly, multi-class SVMs are developed by dividing it into multiple binary classification problems (Duan and Keerthi, 2005). Common two approaches for this are 'one-versus-all' and 'one-versus-one'. In 'one-versus-all' we build a binary classifier to distinguish one of the labels from the rest, whereas, in 'one-versus-one' we build it to distinguish between every two classes. The 'one-versus-all' classification makes use of 'winner-takes-all' strategy whereas the 'one-versus-one' approach uses a voting strategy. We have used the 'one-versus-all' method for classification. For training the classifier, we have created a set of 150 images, each of which is manually corrupted with a Gaussian, Poisson, or Gamma noise. To increase the reliability of the system, we have used different noise variances. Furthermore, a set of images that consists of real noisy data such as medical and satellite images are also created for the testing purpose.

2.2.4 Testing of the system using pioneering Non-local regularization frameworks

For testing the complete system, we use the state of the art non-local regularization algorithms for each noise distributions under consideration. Inspired from the models in Rudin et al. (1992); Gilboa and Osher (2008), we employed the following functional to restore Gaussian noisy images.

$$\min_{I} \left\{ E(I) = \int_{\Omega} |\nabla_{NL} I| dx + \lambda/2 \int_{\Omega} (I - I_0)^2 dx \right\}, \qquad (2.2.22)$$

where $\lambda > 0$ is the regularization parameter, Ω is the area of image support and $\nabla_{NL} I$ is the non-local Total Variation (TV) of I (where $TV(I) = \int_{\Omega} |\nabla I| \, d\Omega$) (refer Liu and Huang (2014),Gilboa and Osher (2008) and Antoni Buades and Morel (2005)).

The speckle reducing model in Jidesh and Balaji (2018) is being used to restore images with Gamma noise distribution and the functional used for this is given below:

$$\min_{I} \left\{ E(I) = \int_{\Omega} |\nabla_{NL} I| dx + \lambda/2 \int_{\Omega} \left(\frac{I_0}{I} + \log I \right) dx \right\}. \qquad (2.2.23)$$

However, in Chapter 5, a more efficient framework is proposed for restoring speckled data.

The non-local regularization framework for denoising photon-limited images is studied in Le et al. (2007),Liu et al. (2017a) and the corresponding energy functional has been used to restore images with Poisson noise distribution. The functional takes the form:

$$\min_{I} \left\{ E(I) = \int_{\Omega} |\nabla_{NL} I| dx + \lambda/2 \int_{\Omega} (I - I_0 \log I) dx \right\}. \qquad (2.2.24)$$

An advanced model for Poisson noise removal is proposed in Chapter 4 of this thesis. The overall process is detailed in Algorithm 1.

2.3 Experimental Results and Analysis

Gaussian, Gamma and Poisson noise distributions are subjected for the present study. For a single image, we have extracted features from thirty different homogeneous regions to make the process more reliable. The segmentation method we have used (Shui and Zhang, 2014) was proposed for SAR images, but it has been observed to work well for the other noisy images too. The segmentation results obtained on Gaussian, Gamma and Poisson noisy images are shown in Figure 2.3. Real SAR, Ultrasound and Micro-

scopic images are used to show the segmentation results, refer to Figure 2.4 for the details. The homogeneous regions extracted are free of any other intensity variations except the noises, hence it helps in analyzing noise distributions more accurately. The JSD/KLD features obtained from fitted curves give significant information about noise distribution. The Figure 2.5 shows the fitting of curves on different noisy inputs. The JSD/KLD shows very small values when the fitting is close to the noise PDF.

Algorithm 1 Algorithm to implement the method
___

Input $I_0 \leftarrow$ Image corrupted by the noise
Output Restored image I

1: Extract homogeneous intensity regions h from input image using the fast segmentation method proposed in Shui and Zhang (2014).
2: **for** each region h **do**
3:     Find the probability density function of the identified homogeneous region h.
4:     Estimate the parameters for different assumed noise distributions (Gaussian, Gamma and Poisson) using Maximum Likelihood estimate (MLE).
5:     Perform curve fittings using the estimated parameters.
6:     Evaluate the JS/KL divergence between the actual estimated PDF and different fitted PDFs.
7:     Find Skewness, Kurtosis, Entropy and Fifth central moment from region h.
8:     Calculate steepness of mean-variance curve using the method proposed in Chehdi and Sabri (1992).
9:     Combine results of step: 6,7 and 8 together to form the final feature vector v.
10: **end for**
11: Feed v into trained multi class SVM to obtain noise distribution label L
12: $\varepsilon \leftarrow$ small scalar positive value.
13: Initialize I^0,
14: **while** $\|I^k - I^{k-1}\|/\|I^k\| < \varepsilon$ **do**
15:     if L is Gaussian then

$$I^{k+1} = \min_I \left\{ E(I) = \int_\Omega |\nabla_{NL} I| dx + \lambda/2 \int_\Omega (I - I_0)^2 dx \right\},$$

16:     else if L is Gamma then

$$I^{k+1} = \min_I \left\{ E(I) = \int_\Omega |\nabla_{NL} I| dx + \lambda/2 \int_\Omega \left(\frac{I_0}{I} + \log I \right) dx \right\},$$

17:     else if L is Poisson then

$$I^{k+1} = \min_I \left\{ E(I) = \int_\Omega |\nabla_{NL} I| dx + \lambda/2 \int_\Omega (I - I_0 \log I) dx \right\},$$

18: **end while**
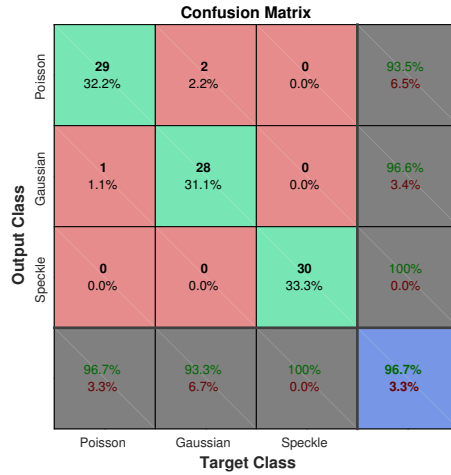
Figure 2.6 Confusion matrix

Table 2.1 Precision and Recall for each class

	Poisson	Gaussian	Speckle
Precision	93.5	96.6	100
Recall	96.7	93.3	100

For training, we used 150 different images (50 from each class) and the testing is performed on 90 images (30 from each category). Test images obtained from decsai (http://decsai.ugr.es) are synthetically corrupted with different noise (following different noise distributions) and being used as the training set. To make the system more robust, the training set was inclusive of Gaussian Noises with different variances, Poisson Noises with different λ values (very high λ values are excluded to avoid the possible similarity with Gaussian) and Gamma noises with different values of shape and scale parameters (Gamma distribution with high shape value will be close to a Gaussian distribution which is excluded to reduce mis classification). Furthermore, the additional testing set was made of background images obtained from computational vision lab at Caltech (Collected by Markus Weber at California Institute of Technology) and these images were synthetically corrupted with Poisson noise.The SAR dataset is obtained from Copernicus Open Access Hub (https://scihub.copernicus.eu/dhus/home) and ESA PolSARpro (https://earth.esa.int/web/polsarpro), Ultrasound images were obtained from Signal Processing Laboratory and Ultrasoundcases.info, and Microscopic images were obtained from the Cell Image Library (www.cellimagelibrary.org). The

33

Table 2.2 Different performance measures evaluated for the system.

Average accuracy	97.7%
Error rate	2.22%
$Precision_M$	96.7%
$Recall_M$	96.7%

testing set also includes noises with different variances and peaks. The trained system classified the testing set with 96.7% accuracy, see confusion matrix in Figure 2.6. Precision and Recall for each class is given in Table 2.1. According to Sokolova and Lapalme (2009), the performance of a multi-class classifier can be evaluated using a number of measures in macro-averaging and micro-averaging category. The Macro-averaging technique treats all classes equally, while micro-averaging favors the classes which are big in size. Here we have used the macro-averaging (denoted by suffix M), as all the classes are of equal size, see Table 2.2 for different performance measures evaluated. The equations used for calculating the same are given below:

$$Precision_M = \frac{\sum_{j=1}^{l} \frac{tp_j}{tp_j+fp_j}}{l} \qquad (2.3.1)$$

$$Recall_M = \frac{\sum_{j=1}^{l} \frac{tp_j}{tp_j+fn_j}}{l} \qquad (2.3.2)$$

$$Average\ accuracy = \frac{\sum_{j=1}^{l} \frac{tp_j+tn_j}{tp_j+fn_j+fp_j+tn_j}}{l} \qquad (2.3.3)$$

$$Error\ rate = \frac{\sum_{j=1}^{l} \frac{fp_j+fn_j}{tp_j+fn_j+fp_j+tn_j}}{l} \qquad (2.3.4)$$

where l is the number of classes used. The terms tp, fn, tn, and fp represents the true positive, false negative, true negative, and false positive respectively.

The restoration results obtained on different real images are given in Figure 2.7. After the classification of noise features, the images corrupted by a particular noise is restored using the corresponding restoration method designed using a variational framework. The subsequent chapters introduces various variational frameworks proposed for restoring images corrupted by various noise distributions from satellite and medical imaging applications.

(a1)	(a2)	(b1)	(b2)

(c1)	(c2)	(d1)	(d2)
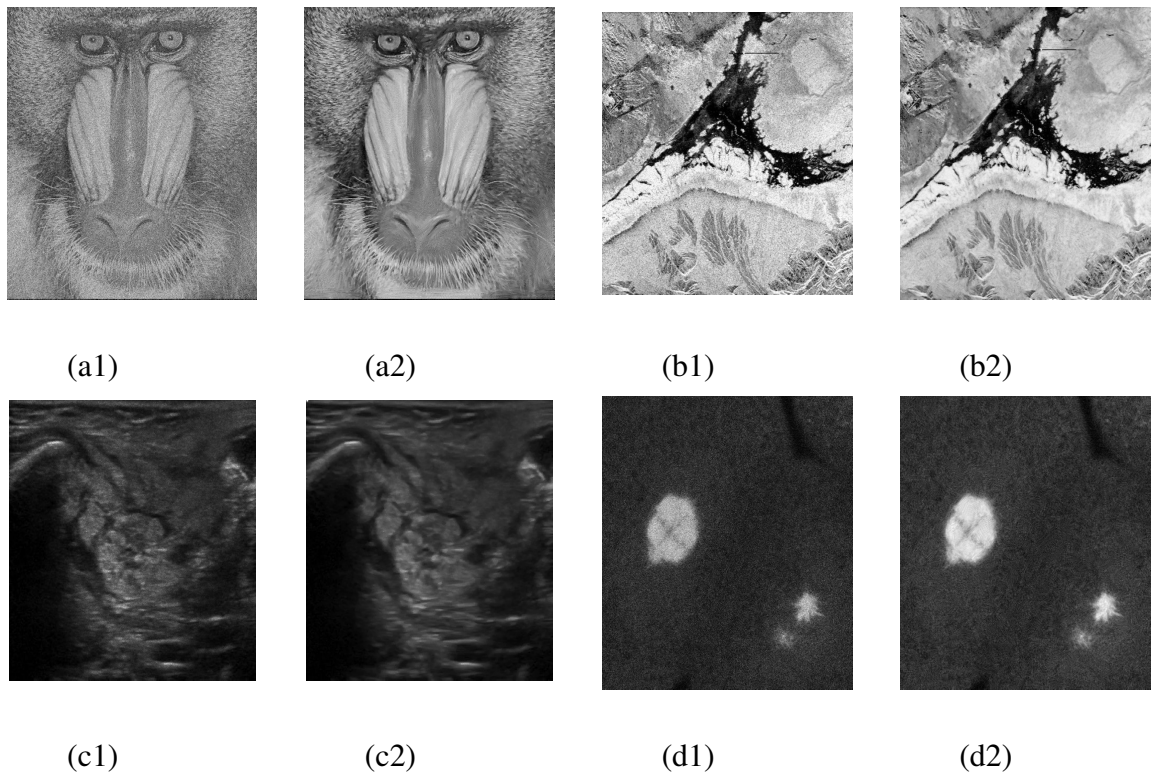
Figure 2.7 Noisy and corresponding Restored images for different Noise distributions: Gaussian Noise: (a1) Noisy image (a2) Restored image; Gamma Noise: (b1) AIRSAR image of Death Valley (CA), Courtesy of ESA polSARpro and NASA/JPL-Caltech (b2) SAR Restored image;(c1) Ultrasound image of Submandibular gland, Courtesy of www.ultrasoundcases.info (c2) Restored image; Poisson Noise: (d1) Confocal microscopic image of Embryo, Courtesy of Cell Image Library (d2) Restored microscopic image;

2.4 Summary of the Chapter

To make the restoration of images more effective and dynamic, a method has been proposed in this chapter. The model analyzes and classifies degraded images based on the statistical distribution of noise. The system designed in this chapter duly determines the kind of noise distortion (in terms of its probability distribution) present in the input images. This serves as a pre-processing step in many restoration models. An appropriate functional based on the noise distribution is chosen to restore images from corresponding noise intervention. The rest of the thesis focuses on proposing new models for restoration and enhancement of low contrast and noisy input images from remote sensing and medical domains.

CHAPTER 3

Retinex model for data uncorrelated noise distortion

3.1 Introduction

Data uncorrelated noise interventions are well-known in most imaging domains, and very commonly seen in hyper-spectral or multi-spectral images as thermal noise or quantization noise (Rasti et al., 2018). Generally, remote sensing images are heavily used by various applications to detect and analyse different objects on Earth and atmosphere. The visual quality of images plays a dominant role in the image analysis. However, these images are also more prone to contrast degradations due to the unpredictable influence of atmospheric conditions like cloud, fog, and poor illumination. Though there are models proposed for homogenizing the intensity or improving the contrast aspects of the data and denoising them, there lacks a method which simultaneously performs these activities.

The major correction methods studied in the literature include absolute radiometric/photometric and relative radiometric/photometric corrections. The absolute radiometric correction methods require accurate measurements of the data during the acquisition (Huifang Li and Shen, 2012). Since, majority of the archived data does not possess this information, relative radiometric corrections are usually employed instead of the absolute ones. The classical image enhancement methods use either histogram equalization (HE) or homomorphic filtering. The HE model is purely based on the radiometric measures and tends to neglect the spatiometric information present in the data. Homomorphic filtering has been used for image processing applications for decades al-

together (Nnolim and Lee, 2008). The basic concept of Homomorphic filtering is to filter images in order to make them visually appealing by exploring the weakness of the human visual system. However, when the homomorphic techniques are used, the colour distortion is quite evident in the enhanced output under the RGB colour model. Processing of the data based on the visual perception makes the results more sensible to the human visual system. Retinex theory makes use of this principle. Perceptually inspired models are found to perform better than the other low-level processing techniques in terms of the visual representation of the output-data (Bertalmio et al., 2009). These models were inspired by the homomorphic filtering technique which considers the intensity as a product of the reflectance of the object and the illumination aspects of the source. The retinex theory is rooted in this concept, a detailed description of the same is provided down the line. There are many image enhancement models proposed in the literature under the retinex framework. In Li et al. (2015), the authors propose a retinex based algorithm for image enhancement using recursive bilateral filtering. In yet another study detailed in Fu et al. (2014), the authors propose an enhancement method with illumination adjustment. A fast alternating direction method is used for its implementation. Another recent work in this field is proposed in Fuyu et al. (2018), where the authors devise a retinex-based image enhancement framework by using region covariance filter. They use three different stages for getting the enhanced data and fuse the inputs to get the final image synthesized. In a similar sense, in Zhang et al. (2018) a retinex model has been devised for image enhancement using a guided filter and a variational framework. In this study, the authors propose a contrast limited adaptive histogram equalization for image enhancement. In Jobson et al. (1997), a popular multi-scale retinex (MSR) algorithm (also known as NASA's retinex method) has been introduced which bridges the gap between colour images and human visual system. In addition, a dictionary-based image enhancement method is found in Chang et al. (2015). Nevertheless, these models lack a proper analysis of the noise distortion present in images. Though there are some efforts to handle noise distortions using the retinex theory as in Liu et al. (2017c); Li et al. (2018), the performance is limited as the distribution of the noise is not taken into consideration while designing the model.

Variational models are the state-of-the-art restoration methods, due to their inherent capacities to handle various data-related features such as edges and discontinuities during the restoration process (Ferradans et al., 2015). Moreover, they provide an effective framework for theoretically analyzing the model in terms of its existence, uniqueness, stability etc. These models also incorporate the Bayesian framework when designing the optimization problem. In this study, we intent to explore the capacity of the variational models to drive the processing in a perceptually significant direction and improve the perceptual quality of the data in terms of both visual and quantitative assessments. Various low-contrast and noisy data are considered from satellite imaging applications in order to scientifically prove the efficiency of the proposed strategy.

Many satellite images such as SAR and multi-spectral images suffer from contrast unevenness and noise intervention. The case is not much different for multi-spectral and hyper-spectral images used in satellite image analysis. These facts eventually provide an insight to tackle the distorted images using efficient models which can address these issues to a considerable extent. Since we deal with the problems which are inverse and ill-posed in nature, certain assumptions are to be made while designing and solving them in order to improve the approximations of the solutions. These assumptions form a set of constraints in the constrained optimization framework. In a variational framework, one can design a constrained optimization problem and solve it effectively. Typically, a designed energy functional denotes an unconstrained optimization problem, minimizing which eventually yields the desired solution. An introduction to variational retinex models and their insights that lead to the design of a new model is highlighted below.

3.1.1 Retinex Theory

Human visual system perceives the color of an object equally in all lighting variations, this illusion is known as the Retinex effect (Ng and Wang, 2011). According to Retinex theory, the intensity of an image can be represented as the product of its illumination and reflectance i.e.

$$I(x,y) = L(x,y)R(x,y), \tag{3.1.1}$$

where $I(x,y)$ represents the digitized intensity image of size $M \times N$, $R(x,y)$ and $L(x,y)$ represent the digitized reflectance and illumination of the image respectively. Initially, retinex got proposed as a random walk algorithm by Land and McCann (Land and McCann, 1971; Land, 1977, 1983). Based on the study of Land et al. (refer Land (1977)) most of the retinex methods perform a logarithmic conversion. In a logarithmic domain, it can represented as

$$i = l + r, \tag{3.1.2}$$

where $i = log(I)$, $l = log(L)$, and $r = log(R)$. Here, computation also is less intense. A variational framework for Retinex was first proposed by Kimmel et al. in Kimmel et al. (2003). It is based on the assumption that the illumination is spatially smooth. The model amounts to:

$$\min E[l] = \int_\Omega \left(\|\nabla l\|_2^2 + \alpha(l-i)^2 + \beta \|\nabla(l-i)\|_2^2 \right) dxdy. \tag{3.1.3}$$

However, as observed in many previous works the reflectance is non-smooth and based on this a new total variation based retinex framework has been introduced in Ng and Wang (2011). The authors of this work assume that the reflectance belongs to a space of bounded variation (BV), in which the total variations (TV) are bounded. Their proposed optimization functional includes both illumination and reflectance terms. They have also suggested the use of advanced numerical algorithms for fast computation. The functional of this model takes the form:

$$\min E[l,r] = \int_\Omega \|\nabla r\| dxdy + \alpha \int_\Omega \|\nabla l\|_2^2 dxdy$$
$$+ \beta (l - r' - i)^2 dxdy + \mu \int_\Omega l^2 dxdy, \tag{3.1.4}$$

where the last term is for the theoretical setting and $r' = -log(R)$. The solution is sought under a spit-Bregman scheme. The main assumptions followed in these works are; the intensity varies smoothly across the image, so is the luminance. However, reflectance being the property of the object on which the light falls, it does not follow a smooth pattern. Therefore, in the minimization functional, the TV norm of the gradient reflectance forms one term, similarly, the L^2 norm of the gradient of the other quantities forms the other terms, including the data fidelity term. Therefore, the non-smooth nature of the reflectance preserves the details present in images. Further, a bayesian framework for variational retinex is also introduced in Wang et al. (2014).

Perceptually inspired variational models have taken a deserving position in the recent literature due to their inherent ability to tune itself to the intensity and reflectance characteristics of the data. In a general setting, the energy functional of a variational model can be expressed in terms of the contrast and dispersion of the data i.e. $E(I) = C(I) + D(I)$, where $C(.)$ and $D(.)$ are contrast and dispersion functionals, respectively. The perceptually inspired retinex models were applied to various imaging domains by the researchers. For instance in Huifang Li and Shen (2012) the authors applied a modified TV based retinex method for intensity correction of remote sensing images. As well-known from the literature, the TV norm performs a piece-wise approximation of the input, resulting in visual discrepancies in the enhanced output. Therefore, in this model, the authors propose to modify the TV norm of the gradient of the reflectance using an adaptive norm constraint which switches between L^2 and TV norms depending on the image characteristics. This provides a better visual interpretation of the output. The model in Huifang Li and Shen (2012) follows

$$\min E[r] = \int_\Omega \|\nabla(r - i)\|_2^2 dxdy + \lambda_1 \int_\Omega (\|\nabla r_t\|_t^t) dxdy$$
$$+ \lambda_2 \int_\Omega (exp(r) - 1/2)^2 dxdy, \qquad (3.1.5)$$

where $t = 1$ when the pixel belongs to an edge, 2 otherwise. The first two terms denote the contrast and the third one is the dispersion of data. The average dispersion is assumed to be 0.5. The model tends to switch between TV and L^2 norms in high and low gradient regions and the corresponding reflectance-term takes the form $||\nabla r_1||$ and $||\nabla r_2||_2^2$ respectively, where r_1 includes the pixels with high gradient values and r_2 includes the pixels with low gradient values (refer Huifang Li and Shen (2012) for more details).

Further, the non-local version of TV retinex introduced in the literature reduces the artefacts caused by normal TV minimization framework due to its piecewise approximation of the input functions. Thus, the non-local framework improves the visual quality of the output, and such a strategy is followed to develop the non-local retinex (NLR) in Zosso et al. (2015). Numerical implementations of the models are done using explicit and semi-implicit schemes. There are some studies relating to the adoption of faster numerical schemes such as Split-Bregman, for improved convergence rate as in

Ma and Osher (2012).

Deriving the motivations from the retinex theory a perceptual inspired framework for restoring and enhancing the images from satellite imaging domain has been studied in this Chapter. The model is designed, implemented and analysed below.

3.2 The proposed retinex model

As a matter of fact, many remote sensing images are low-contrast and noisy in nature, therefore we intent to address these issues using a perceptually driven variational retinex framework under a non-local strategy. We assume that the reflectance is non-smooth, unlike luminance and intensity. Further, we recall that the relation $I = LR$, holds good, where L, I and R follows the definition from (3.1.1). Taking log of the above expression, one has $\log(I) = \log(L) + \log(R)$, denoted as $i = l + r$. Now the constrained optimization problem takes the form

$$
\begin{aligned}
\min_{l,r}\{E(l,r)\} = & \ \lambda_0 \int_\Omega \|\nabla l\|_2^2 dxdy + \lambda_1 \int_\Omega \|\widetilde{\nabla}\hat{r}\|^{p(r)} dxdy \\
& + \lambda_2 \int_\Omega (exp(r) - 1/2)^2 dxdy + \lambda_3 \int_\Omega \|\widetilde{\nabla}\hat{i}\|^{p(i)} dxdy \\
& + \lambda_4 \int_\Omega (r - i + l)^2 dxdy + \lambda_5 \int_\Omega (i - i_0)^2,
\end{aligned}
\tag{3.2.1}
$$

The term $\int_\Omega \|\widetilde{\nabla}\hat{r}\|$ and $\int_\Omega \|\widetilde{\nabla}\hat{i}\|$ in the above expression denotes the weberized non-local TV norm for r and i respectively. They improve the visual quality of the model. Weber's law or Weber-Fechner law explains the influence of background stimulus on human perception of change in physical stimuli. According to this law, in case of vision, the background intensity has an effect on human sensitivity to the intensity change. In Shen (2003), the authors replaces the TV term with weberized local variation $|\nabla\hat{i}| = \frac{|\nabla i|}{i}$ to get a visually pleasing result. In the proposed model instead of using a constant TV norm we are applying a p norm for both reflectance and intensity images. The function $p(x) = 1 + \frac{1}{1 + \|\nabla x\|}$ for all x and it switches from TV to L^2 norms gradually based on the corresponding gradient. In the data fidelity term (the last term), i_0 represents the distorted image intensity and this term is derived based on the assumption that the noise follows a Gaussian law (in the log domain) [1]. The derivation of which is given in

---

[1] Other than Gaussian distribution the noise in satellite images can also follow a multiplicative distribution such as Gamma or Rayleigh resulting in a speckled appearance. However, in the log domain the

Jidesh and Febin (2019). The first two terms in the functional are related to contrast and the third one represents the dispersion of the data. A noise adaptive regularization term $\|\nabla \hat{i}\|^{p(i)}$ is also included for the denoising purpose. Two data fidelity terms are being used in this model, one to minimize the error in $i = l + r$ and the other one to avoid over-smoothing of the intensity variations and preserve textures and details. The regularization prior follows a nonlocal formulation so as to improve the spatiometric processing of the data. The Non-Local gradient of a function I, for a pair of points or pixels (x, y) is defined as,

$$\widetilde{\nabla} I(x, y) = (I(y) - I(x)) \sqrt{w(x, y)}, \tag{3.2.2}$$

where $w(x, y)$ is the weight between x and y. As mentioned in Chapter 1, the weight $w(x, y)$ is evaluated as

$$w(x, y) = \frac{1}{T(x)} e^{-\frac{(G_\sigma * |v(N_x) - v(N_y)|^2)}{h^2}}, \tag{3.2.3}$$

where parameter h controls the negative exponential function, N_x and N_y represents a small neighbourhood around pixels x and y respectively, $T(x)$ is a constant for normalization, and G_σ denotes the Gaussian kernel with standard deviation σ, for further details refer Gilboa and Osher (2008).

3.2.1 Numerical Implementation

An alternating minimization approach is being used for optimizing the model given in equation ((3.2.1)). On each nth iteration of the model, we estimate $r^{n+\frac{1}{2}}$ by minimizing the following functionals:

$$\min_r \{E(r)\} = \lambda_1 \int_\Omega \|\widetilde{\nabla} \hat{r}\|^{p(r)} dxdy \tag{3.2.4}$$

$$+ \lambda_2 \int_\Omega (exp(r) - 1/2)^2 dxdy + \lambda_4 \int_\Omega (r - i + l)^2 dxdy$$

and update r^{n+1} as $max(r^{n+\frac{1}{2}}, 0)$. Then compute $l^{n+\frac{1}{2}}$ by solving

$$\min_l \{E(l)\} = \lambda_0 \int_\Omega \|\nabla l\|_2^2 dxdy + \lambda_4 \int_\Omega (r - i + l)^2 dxdy \tag{3.2.5}$$

and update l^{n+1} as $max(l^{n+\frac{1}{2}}, i)$.

Later, minimize the following to update i^{n+1}

$$\min_i \{E(i)\} = \lambda_3 \int_\Omega \|\widetilde{\nabla} \hat{i}\|^{p(i)} dxdy + \lambda_4 \int_\Omega (r - i + l)^2 dxdy$$

---

multiplicative noise also gets transformed to an additive noise with Gaussian PDF.

$$+\lambda_5 \int_\Omega (i-i_0)^2 dxdy, \tag{3.2.6}$$

To solve (3.2.4), (3.2.5), and (3.2.6), Euler-Lagrange formulation is applied which takes the following form

$$\delta E(r) = -\lambda_1 \widetilde{\nabla} . \frac{\widetilde{\nabla}\hat{r}}{|\widetilde{\nabla}\hat{r}|^{2-p}} + \lambda_2 exp(r)\left(exp(r)-\frac{1}{2}\right)$$

$$+\lambda_4(r-i+l)=0, \tag{3.2.7}$$

$$\delta E(i) = -\lambda_3 \widetilde{\nabla} . \frac{\widetilde{\nabla}\hat{i}}{|\widetilde{\nabla}\hat{i}|^{2-p}} + \lambda_4(r-i+l) \qquad +\lambda_5(i-i_0)=0, \tag{3.2.8}$$

and

$$\delta E(l) = -\lambda_0 \Delta(l) + \lambda_4(r-i+l) = 0. \tag{3.2.9}$$

Then, at each step we use the Gradient descent algorithm to get the intermediate results. The restored version of the image *I* is estimated at the steady state solution of the expression given below:

$$I^{n+1} = I^n + \Delta t\ (-\delta E(I)). \tag{3.2.10}$$

The parameters are set to ensure the best performance of each model implemented for the comparative study.

3.3 Experimental Results and Analysis

Various test images from the hyper-spectral and aerial imaging fields are tested and compared with the state-of-the-art enhancement methods. The methods under the comparative study include VFR method in Kimmel et al. (2003), TVR method in Ng and Wang (2011), Intensity correction of remote sensing images (ICRS) in Huifang Li and Shen (2012), NLR in Zosso et al. (2015), Adaptive Gamma Correction with Weighting Distribution (AGCWD) in Huang et al. (2013), Regularized-Histogram Equalization and DCT (RHE-DCT) in Fu et al. (2015), Robust Retinex Model (RRM) in Li et al. (2018) along with the proposed method. The test images are procured from the publicly available portal MultiSpec, Grupo de Inteligencia Computacional (GIC), and Massachusetts Buildings Dataset (Mnih, 2013). All processing tasks are done in the Hue Saturation Value (HSV) domain. The visual representations of output results for the hyper-spectral and aerial images are demonstrated in Figures 3.1, 3.2, and 3.3 along

44

Figure 3.1 Hyper-spectral image results along with enlarged portions: (a) Low-contrast and noisy input image (b) VFR (Kimmel et al., 2003) (c) TVR (Ng and Wang, 2011) (d) AGCWD (Huang et al., 2013) (e) ICRS (Huifang Li and Shen, 2012) (f) NLR (Zosso et al., 2015) (g) RHE-DCT (Fu et al., 2015) (h) RRM (Li et al., 2018) (i) The proposed method
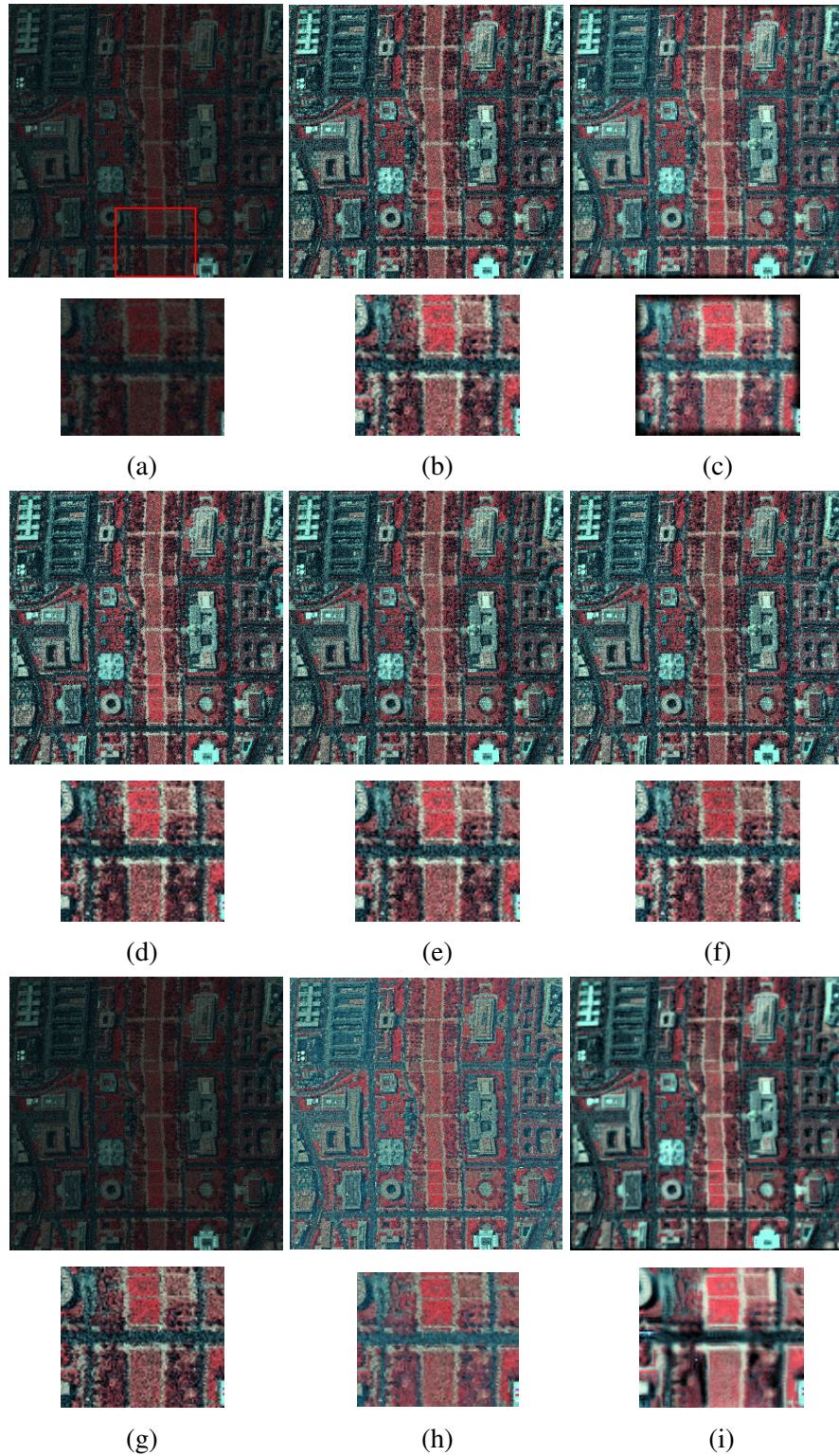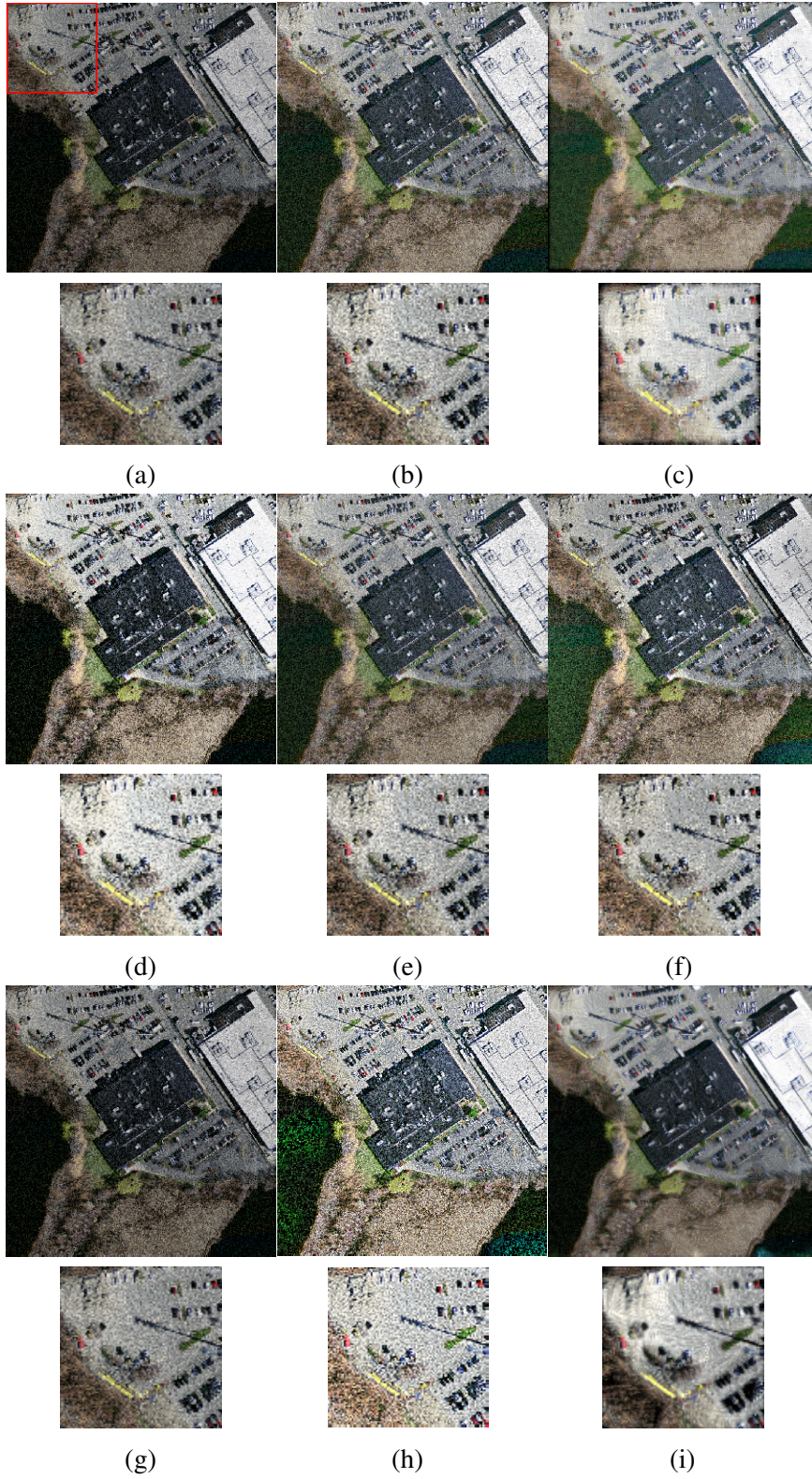
Figure 3.2 Aerial image results along with enlarged portions: (a) Low-contrast and noisy input image, (b) VFR (Kimmel et al., 2003) (c) TVR (Ng and Wang, 2011) (d) AGCWD (Huang et al., 2013) (e) ICRS (Huifang Li and Shen, 2012) (f) NLR (Zosso et al., 2015) (g) RHE-DCT (Fu et al., 2015) (h) RRM (Li et al., 2018) (i) The proposed method

46

with an enlarged portion (for better visual comprehension). The sub-figure (a) of Figures 3.1, 3.2, 3.3 and sub-figure (j) of Figure 3.3 are the input test-images affected by the Gaussian noise and contrast deficiency. In Figures 3.1, 3.2 the noise degradations are synthetically generated to analyze the performance of various models and Figure 3.3 shows the results obtained on a real noisy remote sensing data. As perceived from the results, the proposed model outperforms the other comparative models in terms of the visual quality of the output by reducing noise distortion and enhancing the contrast, whereas the other methods enhances the noise along with data as categorically evident from Figure 3.3. Moreover, the details present in the images are duly preserved by the proposed model.

A quantitative assessment was performed for various methods considered in this study to analyze their performance in terms of denoising and contrast enhancement. We have used the state-of-the-art measures such as blind image integrity notator using discrete cosine transform (DCT) statistics (BLIINDS-II) (Saad et al., 2010), Natural image quality evaluator (NIQE) (Mittal et al., 2013), and Global Contrast Factor (GCF) (Matkovic et al., 2005) to quantify the results. The performance comparison on the basis of different quality metrics are given in Table 3.1. We have fixed the parameter values as $\lambda_0 = 0.4, \lambda_1 = 5, \lambda_2 = 3, \lambda_3 = 0.3, \lambda_4 = 0.08$, and $\lambda_5 = 80$ for getting the result as mentioned in the table. In case of real noisy data (Cuprite bands 223 and 220) the analysis conducted on the influence of each parameter on different quality measures is given in Figure 3.4 and based on this study the parameters are being initialized as $\lambda_0 = 0.06, \lambda_1 = 3, \lambda_2 = 3, \lambda_3 = 0.3, \lambda_4 = 0.01$, and $\lambda_5 = 0.0001$. For the implementation, we have initialized $i = log(I)$, $l = max(i)$ and r as the difference between l and i. The step size used here is 0.03. The parameter λ_0 controls the smoothing of illumination and a high value of which leads to a highly illuminated image. Similarly, λ_1 and λ_3 also control the smoothing in r and i respectively, λ_3 shall be increased to get better denoising. However, a high value of the parameter λ_3 results in loss of the details which can be controlled to a considerable extent by choosing a high value for λ_5. The statistical analysis conducted has proved the denoising capability of the proposed method by providing comparatively very low BLIINDS-II and NIQE values. The BLIINDS-II
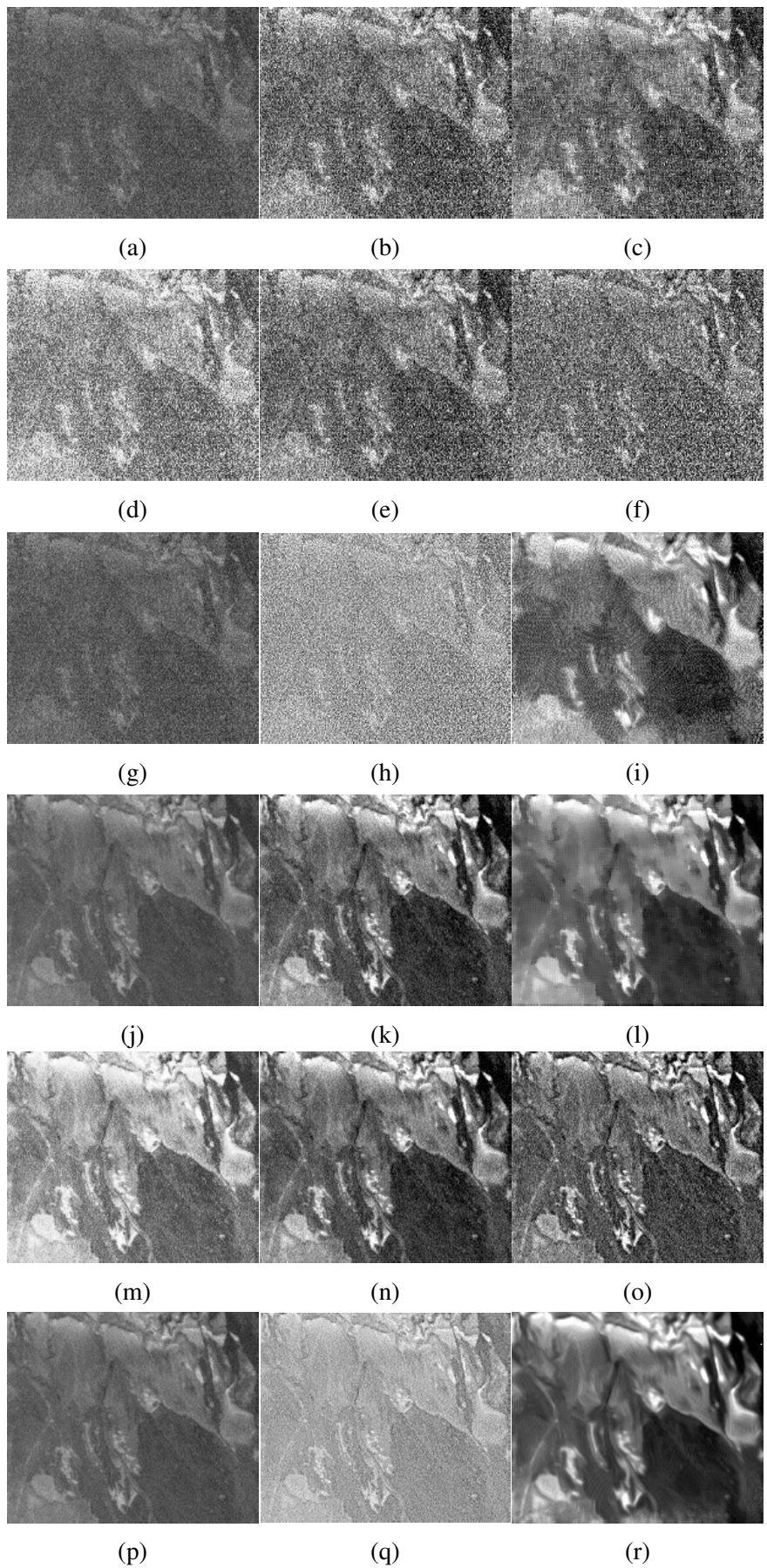
Figure 3.3 Noisy Cuprite Hyper-spectral image and its restored versions (for the bands :223 and 220, respectively) : (a) (j) Low-contrast and noisy input image (b) (k) VFR (c) (l) TVR (d) (m) AGCWD (e) (n) ICRS (f) (o) NLR (g) (p) RHE-DCT (h) (q) RRM (i) (r) The proposed method
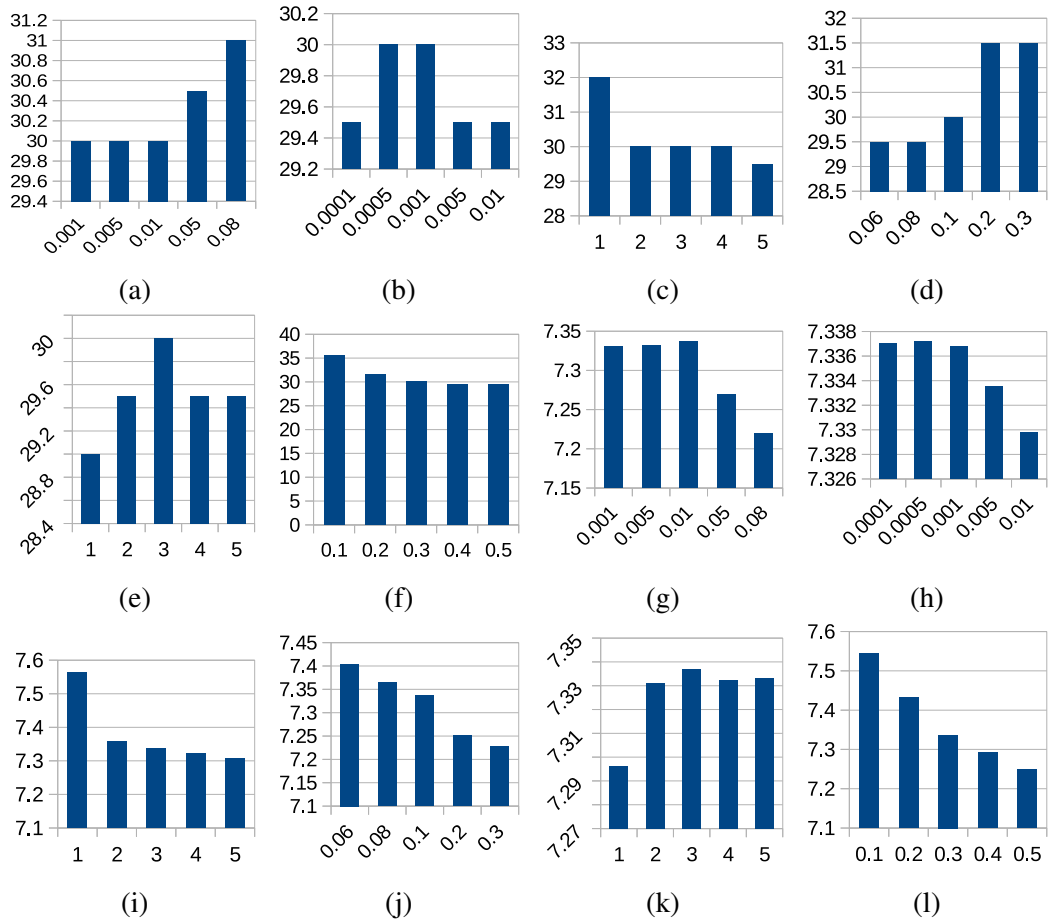
Figure 3.4 Parameter analysis on the basis of BLIINDS-II and GCF measures (a) (g) Parameter λ_4 on BLINDS-II, GCF (b) (h)Parameter λ_5 on BLINDS-II, GCF (c) (i)Parameter λ_2 on BLINDS-II, GCF (d) (j)Parameter λ_0 on BLINDS-II, GCF (e) (k) Parameter λ_1 on BLINDS-II, GCF (f) (l) Parameter λ_3 on BLINDS-II, GCF

measure applies DCT and fetches the features related to structure and contrast of the data to predict the quality of the restored image. Consequently, low value of BLIINDS-II also implies that the method proposed here is superior in preserving the structures and contrast of the images tested. The NIQE measure uses the quality aware statistical features to build the model. This measure is also evaluated as the deviation of the observation from the natural image model, as a result low value of this measure indicates a better restoration and enhancement. The GCF is calculated as a weighted average of local contrast values measured in different scales. From the tabulated values, we can infer that the GCF is comparatively high for the proposed method, which implies a better contrast enhancement capability of the method under study.

49

Table 3.1 Comparison of Quality metrics of various Enhancement methods: VFR (Kimmel et al. (2003)),TVR (Ng and Wang (2011)), ICRS (Huifang Li and Shen (2012)), NLR (Zosso et al. (2015)), AGCWD (Huang et al. (2013)),RHE-DCT (Fu et al. (2015)), RRM (Li et al. (2018))

Images	Quality Metrics	VFR	TVR	ICRS	NLR	AGCWD	RHE-DCT	RRM	Proposed method
Cuprite Band 223	BLIINDS-II	75	79.5	79	87.5	72	74.5	76.0	**36.5**
	GCF	7.2958	7.3408	7.3328	6.2553	6.4431	5.8103	3.6992	**7.3474**
	NIQE	19.2919	18.9226	18.6380	21.0405	25.0997	21.7601	23.8297	**12.9182**
Cuprite Band 220	BLIINDS-II	46.5	57	56.5	63.5	45.5	44.5	60.5	**29.5**
	GCF	7.2923	6.7693	7.2930	6.4141	5.7208	5.4292	2.6518	**7.4040**
	NIQE	10.5368	9.7968	10.0110	10.6568	10.1356	10.3818	13.8240	**5.7654**
Washington DC	BLIINDS-II	34	32.5	34	37	35	38	26.5	**20.5**
	GCF	8.3853	9.1741	8.3853	8.0087	8.8776	6.7472	6.8067	**9.4429**
	NIQE	10.8893	9.5219	10.8610	10.9776	13.3943	11.4816	11.1273	**4.5734**
Aerial image	BLIINDS-II	43	48	43	43	44	49.5	54.0	**22**
	GCF	9.4197	9.5607	9.4005	9.0846	9.9565	9.8335	11.5579	**9.9576**
	NIQE	12.5045	10.1054	12.3106	11.2920	13.2540	12.1591	19.5503	**4.9588**

3.4 Summary of the Chapter

In this chapter, a perceptually inspired image restoration model has been proposed for denoising and enhancing the remote sensing images corrupted by data uncorrelated noise distortions and contrast degradations. The presence of additive data-independent noise along with contrast inhomogeneity has been addressed in this work. The non-local framework employed here duly preserves the image features. By the use of a retinex model, the proposed method has succeeded in addressing the intensity inhomogeneity in the images while restoring them from noise interventions. The results perceived from the image representations and numerical quantifications are in favor of the proposed strategy.

CHAPTER 4

Perceptually inspired model for data correlated Poisson noise distortion

4.1 Introduction

Monitoring natural phenomenons, mapping of land cover, meteorological studies, military surveillance, etc. actively uses satellite images to give real-time updates. For instance, in remote sensing, the sensors kept on aircraft or satellites measure the electromagnetic radiations getting reflected and scattered from different objects on Earth to study about them. As pointed out in the previous chapter, satellite images generally get degraded due to the interaction of probing signals with atmospheric particles and end up forming low contrast and noisy images. These degradations limit different applications of these data eventually by reducing the accuracy and precision. As the images captured (eg: aerial, hyper-spectral, multi-spectral, Radar etc.) are severely degraded due to intensity inhomogeneity across the region of the capture, image enhancement is an inevitable preprocessing step in most of the remote sensed imaging applications. The major degradation scenario can be attributed to the environmental conditions which reduce the contrast and the details of the captured remote sensing images (Demirel et al., 2010).

Contrast enhancement is generally processed in a linear or non-linear manner. The spatial domain enhancement strategies are pioneered by the linear contrast stretching methods which changes the range of intensity values. We recap from chapter 3 that histogram equalization is a widely used technique which tries to equalize the density of the pixel values (Kwak and Park, 2014). Nevertheless, these methods lead to over-

enhancement to the high-peaks in the input data. This issue is addressed to a considerable extent in brightness-preserving dynamic HE (Ibrahim and Kong, 2007) and histogram modification framework (Arici et al., 2009). Yet another spatial domain model has been proposed for contrast enhancement. This model uses an adaptive gamma correction with weighting distribution (AGCWD) (Huang et al., 2013). Nevertheless, they tend to neglect the local image features while considering the global aspect of the data.

The fact discussed above has opened up an era of transformed domain techniques such as singular value decomposition (SVD) based model (Demirel et al., 2008), discrete cosine transform (DCT) based model (Fu et al., 2015) etc. In Demirel et al. (2008), a singular value equalization method is proposed to adjust the image brightness. A discrete wavelet-based alternative is provided in Demirel et al. (2010) which is claimed to achieve a better contrast enhancement. A method using discrete wavelet transform (DWT) and adaptive intensity transformation is also introduced for remote sensed image enhancement in Lee et al. (2013). However, the method is highly sensitive to the set parameters which is practically difficult to choose adaptively. Further to mention, a retinex based multi-scale method and a general illumination normalization method is proposed in Jang et al. (2011) and Zhang et al. (2014), respectively for optical and multiple remote sensed images. However, as noted earlier these methods also fail to retain the local features in the image, though they yield good enhancement results as far as global features are concerned.

The local feature enhancement has been considered in a transformed domain model proposed in Fu et al. (2015), where the authors propose a global enhancement using a modified histogram formation. A DCT is employed in this model to preserve the local features properly. A further improvement can be noticed in the work Liu et al. (2017b), where the authors propose a histogram compacting transform along with a linear stretch to enhance the contrast of remote sensed data. A local remapping algorithm is included in this model to preserve more details in the course of linear stretching.

Along with the contrast related artefacts, many aerial and satellite data are contaminated by the unavoidable noise intervention either during their capture or transmission. Generally, noises present in such images can be categorized as data-independent ther-

mal noise, stripping noise and data-dependent shot noise (Poisson noise) (Rasti et al., 2018). Removal of data-correlated noise like shot noise is comparatively challenging than the common data-independent counterparts. Though there are many models proposed for denoising the data and enhancing the contrast, a handful of them perform both simultaneously. In this Chapter, we intent to address the problem of enhancing and denoising the data simultaneously. A perceptual model based on the retinex theory has been employed to perform these tasks. The variational framework being an effective strategy to solve the inverse problems and analyze them from a theoretical perspective, we resolve to explore a variational retinex framework based on the perceptual model for enhancing and restoring images.

Retinex models have taken a considerable progress in the image enhancement domain over the last few years. Among them, the variational retinex models are proved to be effective in restoring contrast degraded images effectively. An introduction to retinex theory and a detailed discussion of various retinex models that were introduced lately is done in Chapter 3. A non-local TV model for retinex is also introduced by Zosso et. al. (Zosso et al., 2015). In Huifang Li and Shen (2012), authors proposed the use of a variational framework for retinex in remote sensing images to address the low contrast issues. Later a spatially adaptive retinex variational model also got introduced to apply in remote sensing domain (Lan et al., 2014), where they proposed the usage of a weight parameter W to regulate the TV prior, and a fast numerical implementation has been performed to improve the computational efficiency. The modified functional appears:

$$\min E[r] = \int_\Omega \|(i - l - r)\|^2 dxdy + \lambda_1 \int_\Omega (\|\nabla l\|_2^2) dxdy$$
$$+ \lambda_2 W \int_\Omega (\|\nabla r\|) dxdy + \lambda_3 \int_\Omega (exp(r) - 1/2)^2 dxdy. \qquad (4.1.1)$$

Even though these methods could enhance the remote sensed images to a considerable extent, they tend to ignore the inherent noise present in these images. Hence, after the enhancement, noise appears more prominent in the results.

4.1.1 Poisson degradation

Apart from the contrast related degradation, the images are also observed to be corrupted by noise interventions. Apparently in many satellite imaging modalities, the

noise is data-correlated and does not seem to follow a Gaussian law as discussed in previous works. The noise formation can be modeled as a Poisson process as the images are formed from reflections of signals from the object of interest. The Poisson noise, unlike the other noise interventions, is regarded as an aftermath of deficiency of photons that hit on the screen to form the final image. So, the regions where there is a deficiency of photons contribute to the deficiency of data, consequently leading to a Poisson noise intervention. We recall that, a Poisson distribution essentially follows the PDF:

$$P_{\lambda_p}(z) = \frac{e^{-\lambda_p}\lambda_p^z}{z!}, z \geq 0, \tag{4.1.2}$$

where λ_p denotes the parameter of the distributions signifying the mean and variance of the distribution. Many images formed under hyper and multi-spectral modality can be designed as a result of a Poisson process. Therefore, the degradation in such data essentially follows a Poisson process. In other words, the noise in such modalities can be regarded as a Poisson.

4.1.2 Restoration of Poisson images

As seen from various sources in the literature, variational methods lay a prominent platform to restore images corrupted by various noise distributions. A Bayesian framework is employed for deriving the functional which inherently captures the noise characteristics such as its distribution and parameter details from the image data. Variational models for handling Poisson data has been explored in various works earlier (Le et al., 2007; Kayyar and Jidesh, 2018). The derivation of the functional to handle Poisson data is highlighted in Appendix A of this thesis. The functional takes the form:

$$E(u) = \min_u \int \phi(u) + \lambda(I - I_0 \ log \ I), \tag{4.1.3}$$

where $\phi(u)$ denotes a prior function such as TV or Tikhonov. A non-local version of this model had been employed in Kayyar and Jidesh (2018) for restoring Poisson corrupted data. The models discussed above performs a restoration under the assumption of a Poisson noise. However, they fail to perform an enhancement to the image, especially when the data is contrast deficient.

The noise distribution is analysed using the method described in Chapter 2 of this thesis. The images classified as Poisson distorted by the machine learning framework
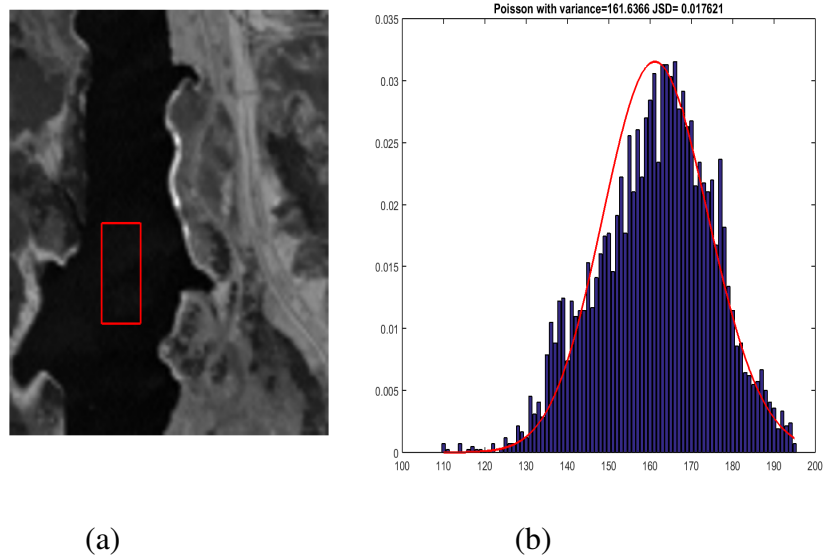
Figure 4.1 (a) Original noisy Hyper-spectral band (b) Noise fitting done on area marked

in Chapter 2 is being addressed here. Various hyper-spectral and multi-spectral images from xView database are subjected to the distribution-analysis study. Most of these images are observed to follow a Poisson law. In other words, these images can be modeled as an output of a Poisson process. The curve fitting observed from the homogeneous region of one of these images is plotted in Figure4.1. Moreover, the images are observed to be contrast deficient, and certain images even possess varying contrast characteristics or uneven contrast distribution. This makes the enhancement process more tedious.

These facts motivate us to propose a retinex based variational model to restore Poisson-noisy images and enhance them to reduce intensity inhomogeneity and improve the contrast deficiency even in case of uneven contrast distortions. This model comes in handy in many satellite imaging applications.

4.2 The proposed retinex model

In the proposed method, it is assumed that the illumination l is spatially smooth and to enforce this the L_2 norm of the illumination is being used in the formulation of the functional. Further, the reflectance and intensity variations are represented using the non-local framework to ensure the coarse operations on textured areas and boundaries to actively enforce the piecewise smooth assumption (Refer Gilboa and Osher (2008)). A weight matrix $W(x)$ is also used to scale the TV norm according to the magnitude of

the gradient. This weight function helps to retain more details on the edges and at the same time, it helps in smoothing-out the homogeneous intensity regions. The weight function is defined as:

$$W(x) = 1 + \frac{1}{\varepsilon + \|\nabla x\|}, \qquad (4.2.1)$$

where ε is a small positive value. The Weberized TV restoration proposed by Shen (2003) stated the influence of background in perceiving the change in the intensity. According to this vision psychology, a Weberized TV model has been successfully introduced for restoration. Hence a Weberized TV regularization has been employed in the present study to enhance the visual appearance of the restored data. The reflectance R is constrained using $(R - 1/2)^2$ which forces the reflectance R to be close to $1/2$ or the trivial average of the reflectance assuming this range to be $[0 - 1]$. Converting this constrain in a logarithmic domain gives $(exp(r) - 1/2)^2$. Minimization of the term $(r - i + l)$ enforces the condition $i = l + r$. The data fidelity $(I - I_0 log(I))$ assuming a shot noise following the Poisson distribution has been derived in this proposed study using the maximum a posteriori (MAP) estimation of the noise probability density function (PDF). The details may be found in the Appendix A. The proposed functional for enhancement and restoration is shown below:

$$\min_{l,r,i}\{E(l,r,i)\} = \int_{\Omega} \|\nabla l\|_2^2 dxdy \qquad (4.2.2)$$

$$+ \lambda_1 \int_{\Omega} W(r)\|\nabla \hat{r}\| dxdy$$

$$+ \lambda_2 \int_{\Omega} (exp(r) - 1/2)^2 dxdy$$

$$+ \lambda_3 \int_{\Omega} W(i)\|\nabla \hat{i}\| dxdy$$

$$+ \lambda_4 \int_{\Omega} (r - i + l)^2 dxdy$$

$$+ \lambda_5 \int_{\Omega} (I - I_0 \, log \, I).$$

The above minimization problem can be converted into three subproblems, they are

r-subproblem:

$$\min_{r}\{E(r)\} = \lambda_1 \int_{\Omega} W(r)\|\nabla \hat{r}\| dxdy \qquad (4.2.3)$$

$$+ \lambda_2 \int_{\Omega} (exp(r) - 1/2)^2 dxdy$$

$$+ \lambda_4 \int_{\Omega} (r - i + l)^2 dxdy.$$

58

i-subproblem:

$$\min_i \{E(i)\} = \lambda_3 \int_\Omega W(i)\|\nabla\hat{i}\|dxdy \qquad (4.2.4)$$

$$+ \lambda_4 \int_\Omega (r-i+l)^2 dxdy$$

$$+ \lambda_5 \int_\Omega (I - I_0 \ log \ I) dxdy.$$

l-subproblem:

$$\min_l \{E(l)\} = \int_\Omega \|\nabla l\|_2^2 dxdy \qquad (4.2.5)$$

$$+ \lambda_4 \int_\Omega (r-i+l)^2 dxdy.$$

4.2.1 Numerical Implementation

The above given subproblems can effectively solved using the split-Bregman algorithm. According to which a constraint $d = \nabla\hat{r}$ gets added in to the subproblem in (4.2.3) along with a new auxiliary variable b_1. The new subproblem under the above modification amounts to:

$$\min_r \{E(r)\} = \lambda_1 W(r)\|d\| \qquad (4.2.6)$$

$$+ \lambda_2 (exp(r) - 1/2)^2$$

$$+ \lambda_4 (r-i+l)^2$$

$$+ \lambda \|d - \nabla\hat{r} - b_1\|_2^2.$$

For equation (4.2.4), a constraint $p = \nabla\hat{i}$ and an auxiliary variable b_2 is added to form the minimization problem as below:

$$\min_i \{E(i)\} = \lambda_3 W(i)\|p\| \qquad (4.2.7)$$

$$+ \lambda_4 (r-i+l)^2$$

$$+ \lambda_5 (I - I_0 \ log \ I)$$

$$+ \alpha\|p - \nabla\hat{i} - b_2\|_2^2.$$

Equation (4.2.6) can be split into r, d, and b_1 subproblems as below

$$r^{k+1} = \min_r \left\{ \lambda_2 (exp(r) - 1/2)^2 + \lambda_4 (r-i+l)^2 \right. \qquad (4.2.8)$$

$$\left. + \lambda \|d - \nabla\hat{r} - b_1^k\|_2^2 \right\},$$

$$d^{k+1} = \min_r \left\{ \lambda_1 W(r)\|d\| + \lambda \|d - \nabla\hat{r} - b_1^k\|_2^2 \right\}, \qquad (4.2.9)$$

and

$$b_1^{k+1} = b_1^k + (\nabla \hat{r} - d^{k+1}). \tag{4.2.10}$$

Similarly equation (4.2.7) can be split into i, p, and b_2 subproblems as below

$$i^{k+1} = \min_r \left\{ \lambda_5(I - I_0 \ log \ I) + \lambda_4(r - i + l)^2 \right. \tag{4.2.11}$$

$$\left. + \alpha \| p - \nabla \hat{i} - b_2^k \|_2^2 \right\},$$

$$p^{k+1} = \min_p \left\{ \lambda_3 W(i) \, \| p \| + \alpha \| p - \nabla \hat{i} - b_2^k \|_2^2 \right\}, \tag{4.2.12}$$

and

$$b_2^{k+1} = b_2^k + (\nabla \hat{i} - p^{k+1}). \tag{4.2.13}$$

Euler-Lagrange derivative of equation (4.2.8) is evaluated as

$$\lambda_2(exp(r) \, (exp(r) - 1/2)) + \lambda_4(r - i + l) \tag{4.2.14}$$

$$+ \lambda \nabla.(d - \nabla \hat{r} - b_1^k) = 0.$$

This can be solved effectively in the Fourier domain [1].

$$r^{k+1} = F^{-1} \left\{ \frac{\lambda_4 F(i-l) - \lambda_2 F((exp(r) \, (exp(r) - 1/2))) - \lambda F(\nabla.(d - \nabla \hat{r} - b_1^k))}{\lambda_4} \right\}. \tag{4.2.15}$$

Euler-Lagrange derivative of (4.2.11) is as given below

$$\lambda_5(I - I_0) + \lambda_4(r - i + l) + \alpha \nabla.(p - \nabla \hat{i} - b_2^k) = 0. \tag{4.2.16}$$

The problem stated above is solved effectively in the Fourier domain as:

$$i^{k+1} = F^{-1} \left\{ \frac{\lambda_5 F(I_0) - \lambda_4 F(r+l) - \alpha F(\nabla.(p - \nabla \hat{i} - b_2^k))}{F((\lambda_5 \frac{I}{i}) - \lambda_4)} \right\}. \tag{4.2.17}$$

The d and p subproblems in (4.2.9) and (4.2.12) can be solved by using *shrink* function which is defined as

$$shrink(x, \theta) = \frac{x}{|x|} \max(|x| - \theta, 0). \tag{4.2.18}$$

Hence these subproblems can be rewritten as follows (assumes $\lambda_1 = 1$ and $\lambda_3 = 1$)

$$d^{k+1} = shrink(\nabla \hat{r} + b_1^k, \frac{W(r)}{\lambda}), \tag{4.2.19}$$

$$p^{k+1} = shrink(\nabla \hat{i} + b_2^k, \frac{W(i)}{\alpha}). \tag{4.2.20}$$

Auxiliary variables b_1 and b_2 are updated using

$$b_1^{k+1} = b_1^k + (\nabla \hat{r} - d^{k+1}), \tag{4.2.21}$$

$$b_2^{k+1} = b_2^k + (\nabla \hat{i} - p^{k+1}). \tag{4.2.22}$$

---

[1]where F and F^{-1} represents Discrete Fourier transform (DFT) and its inverse, ie, $y(m) = F(x(n)) = \sum_{n=0}^{N-1} x(n) e^{-j\frac{2\pi}{N}mn}$ and $x(n) = F^{-1}(y(m)) = \frac{1}{N} \sum_{m=0}^{N-1} y(m) e^{j\frac{2\pi}{N}mn}$

Finally, the optimization problem in equation (4.2.5) is solved by taking the Euler-Lagrange derivative which derives:

$$\Delta l + \lambda_4 (r - i + l) = 0. \tag{4.2.23}$$

The above expression is solved in the Fourier domain as:

$$l^{k+1} = F^{-1} \left\{ \frac{\lambda_4 F(i-r)}{F(\lambda_4 + \Delta)} \right\}. \tag{4.2.24}$$

The overall algorithm of the process is highlighted below.

Algorithm 2 Algorithm to implement the method

Input $I_0 \leftarrow$ Low contrast and noisy Digital image of size $M \times N$
Output Enhanced and Restored Digital image I of size $M \times N$

1: Initialize[2] $k = 1, \varepsilon = 0.0001, \lambda = 3.8, \lambda_2 = 6, \lambda_4 = 800, \lambda_5 = 0.001, \alpha = 0.8, d^1 = [0], b_1^1 = [0], p^1 = [0], b_2^1 = [0], i^1 = [log(I_0)], l^1 = [\max(i^1)], and\ r^1 = [(l^1 - i^1)]$
2: **while do** $\|i^{k+1} - i^k\| / \|i^{k+1}\| < \varepsilon$
3:      Given i^k, l^k and r^k find r^{k+1} using equation (4.2.15)
4:      Update d^{k+1} using shrink operator as in equation (4.2.19)
5:      Update b_1^{k+1} using equation (4.2.21)
6:      Given i^k, l^k, r^k and I_0 solve equation (4.2.17) to get i^{k+1}
7:      update p^{k+1} using shrink operator as in equation (4.2.20)
8:      update b_2^{k+1} using equation (4.2.22)
9:      Given i^k and r^k find l^{k+1} using equation (4.2.24)
10: **end while**
11: update I as exponential of $(l + r)$

4.3 Experimental Results and Analysis

The testing of various models is done using a large set of images falling under the category of hyper-spectral and aerial imagery. However, to maintain the brevity in explanation, only a subset of them, i.e., three synthetically noisy images (two xView satellite images and Washington DC, see Figure4.2), and two original noisy data (Pines and Jasper Ridge), have been used for demonstrating the results. Nevertheless, the performances of the methods to the other test images are observed to follow the pattern exhibited by the demonstrated ones. Non-uniformly illuminated and Poisson-noisy versions of these test images are used as the input to the system, see Figure 4.2 for the original images. The sub-figure (a) of Figure4.2 shows the original Washington

---

[2]All initializations in [] represent matrices of size $M \times N$, eg: [0] denotes an $M \times N$ matrix initialized with zeros

DC false-color image, which is converted to a vertically contrast degraded image by using a mask, and the resultant image is given in sub-figure (b). The sub-figures (c) and (d) are the originally contrast degraded satellite images. Poisson noise of peak 100 is used to degrade all these test images synthetically; corresponding noisy images are given in sub-figure (a) of Figure 4.3, Figure 4.4, and Figure 4.5. The performance of various comparative models for real noisy input images are shown in Figure 4.6, and Figure 4.7. The different parameter values used for the experiments are $\lambda = 3.8, \lambda_2 = 6, \alpha = 0.8, \lambda_4 = 800, \lambda_5 = 0.001$ and for the hyper-spectral images which are prone to more contrast degradation, the value of the parameter λ_2 is raised to 7.5. Among the parameters mentioned above, λ and λ_2 are specifically for processing the reflectance part of the image. Similarly, α and λ_5 controls the regularity and fidelity of the intensity data. The λ_4 signifies a global fidelity term. The parameter λ is observed to control the diffusion of reflectance part of the data. The reflectance includes the textures and other fine details. Therefore, this value is chosen to ensure the trade off between smoothing and preserving details. Throughout the experiment, we have used a fixed value for this term to retain the natural textured effect on the image. Upon an increase in the peak value of the noise, the parameter α has to be increased subsequently to maintain the restoration efficiency of the model. However, a too high value for this parameter may deteriorate the edge preservation capability of the model under consideration. To address this issue, the value of λ_5 is chosen appropriately to check the loss of information in the course of evolution. The term associated with the parameter λ_5 is the data-fidelity term derived based on the distribution characteristics of the noise (the noise is assumed as an output of a Poisson process). For a very low peak noise, the λ_5 value should be slightly higher.

The denoising ability of the system is categorically demonstrated using the state-of-the-art Poisson denoising models such as Fast TV (Wang and He, 2017) and NLTV (non-local TV)(Gilboa and Osher, 2008). Though the restoration methods considered for the comparison does not possess an enhancement capacity by themselves unlike the proposed model, we have associated an additional enhancement characteristic to them (FAST TV+CLAHE, NLTV+CLHE, etc.) in order to make them in line with

the proposed model for the sake of comparative study. The enhancement achieved by the system is also compared with the recent retinex based enhancement methods like Non-Local TV Retinex (NLTVR) (Zosso et al., 2015) and perceptually inspired variational model (PVM) for remote sensing (Huifang Li and Shen, 2012). Since we are proposing a non-local retinex framework, in order to justify the comparative results of the other methods, we have combined the retinex based enhancement methods with NLTV denoising method to form the NLTVR+NLTV and PVM+NLTV.

In addition to the visual comparisons, a quantitative study has been carried out using various quality metrics such as AG (Average Gradient) (Li et al., 2017), NIQE (Naturalness Image Quality Evaluator) (Mittal et al., 2013), GCF (Matkovic et al., 2005), Entropy (Karathanassi et al., 2007), and visual descriptors (Hautiere et al., 2008) e (rate of new visible edges), $\bar{r}$ (quality of contrast restoration), σ (number of saturated pixels). The resultant images of various comparative methods are portrayed in Figures 4.3, 4.4, and 4.5. Though most of the methods considered herein for the comparative study performs fairly well as far as denoising is concerned, the NLTVR+NLTV method performs slightly better when both denoising and enhancement are considered at once. Nonetheless, the proposed strategy exhibits a profound quality in the visual representations. The zoomed-in portions of the image duly justify the details preserving capabilities of the proposed model. In Figure 4.4 the contrast enhancement obtained by the proposed method is promising, and the corresponding enlarged image also shows the denoising capability of the system. As noticeable from Figure 4.5, the NLTVR+NLTV, PVM+NLTV, and the proposed method apparently preserve uniform illumination in the data, and the output appears more natural. Further, analyzing the enlarged portions of the restored outputs, the proposed model is observed to preserve textures and details better than the other ones.

Table 4.1 give the comparison of different denoising methods on the basis of AG and NIQE values. NIQE depicts the naturalness of the restored image, and AG measures the quality of the image. A high value of NIQE indicates a low performance in terms
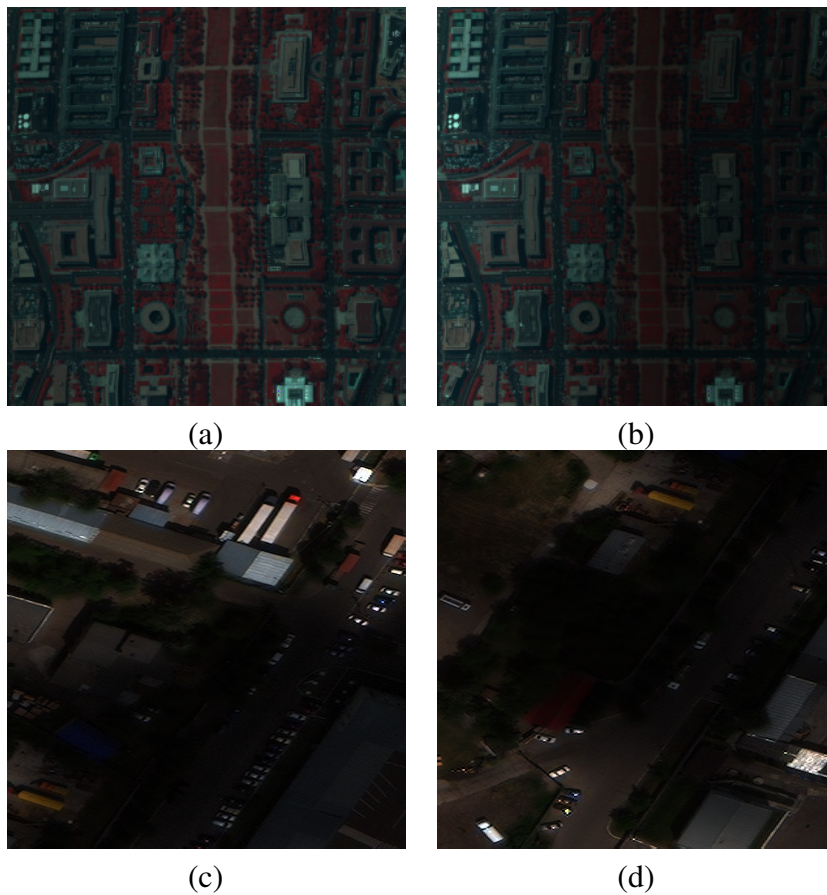
Figure 4.2 Test images used: (a) Original Hyper-spectral image of Washington DC (HYDICE, 191 spectral bands, spatial resolution: 2.8m, pixels used: 307×307, bands used: 60, 27 and 17), courtesy MultiSpec by Purdue University (b) Vertically contrast degraded image after applying mask (c) (d) Original WorldView-3 satellite images at 0.3m ground sample distance, courtesy xView dataset (Lam et al., 2018).
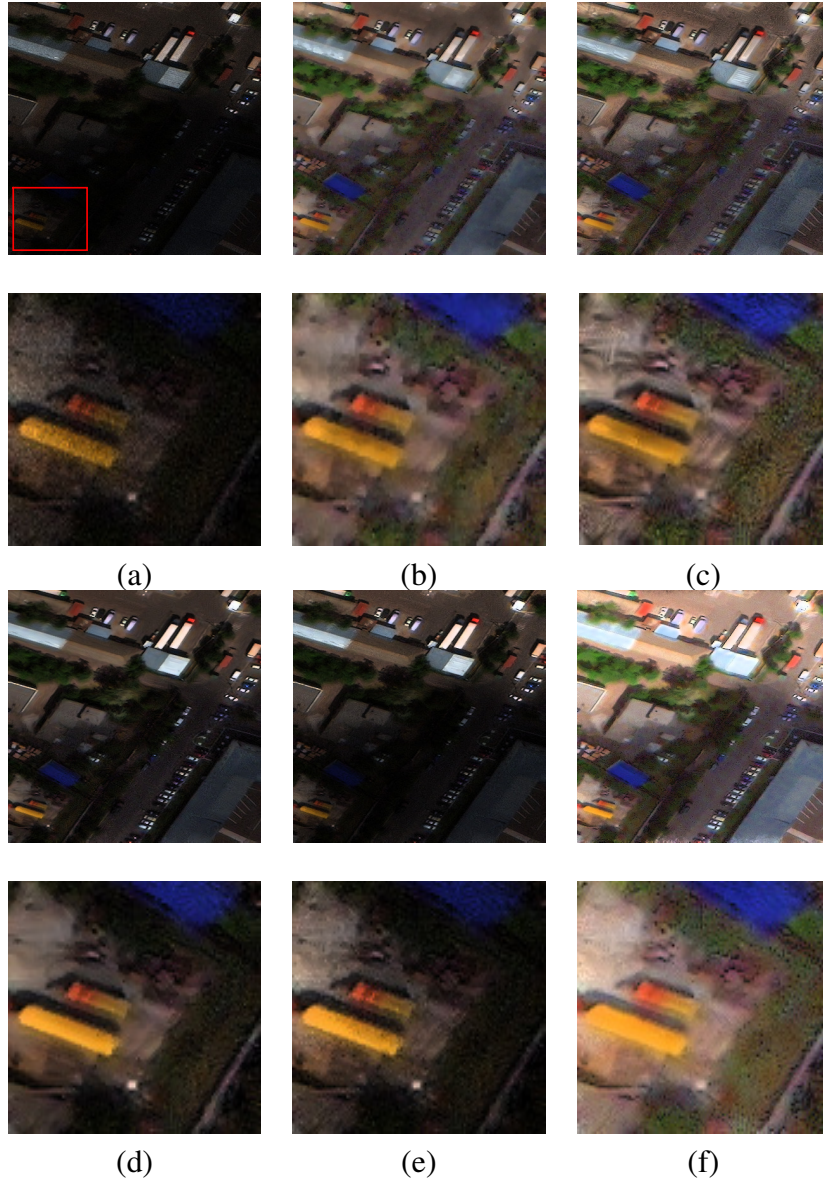
Figure 4.3 xView image 1 with Poisson noise: restoration results and corresponding enlarged portions below it (a) Input image (b) Restored using Fast TV+CLAHE (Wang and He, 2017) (c) Restored using NLTV+CLAHE (Gilboa and Osher, 2008) (d) Restored using NLTVR+NLTV (Zosso et al., 2015) (e) Restored using PVM+NLTV (Huifang Li and Shen, 2012) (f) Restored using Proposed method.
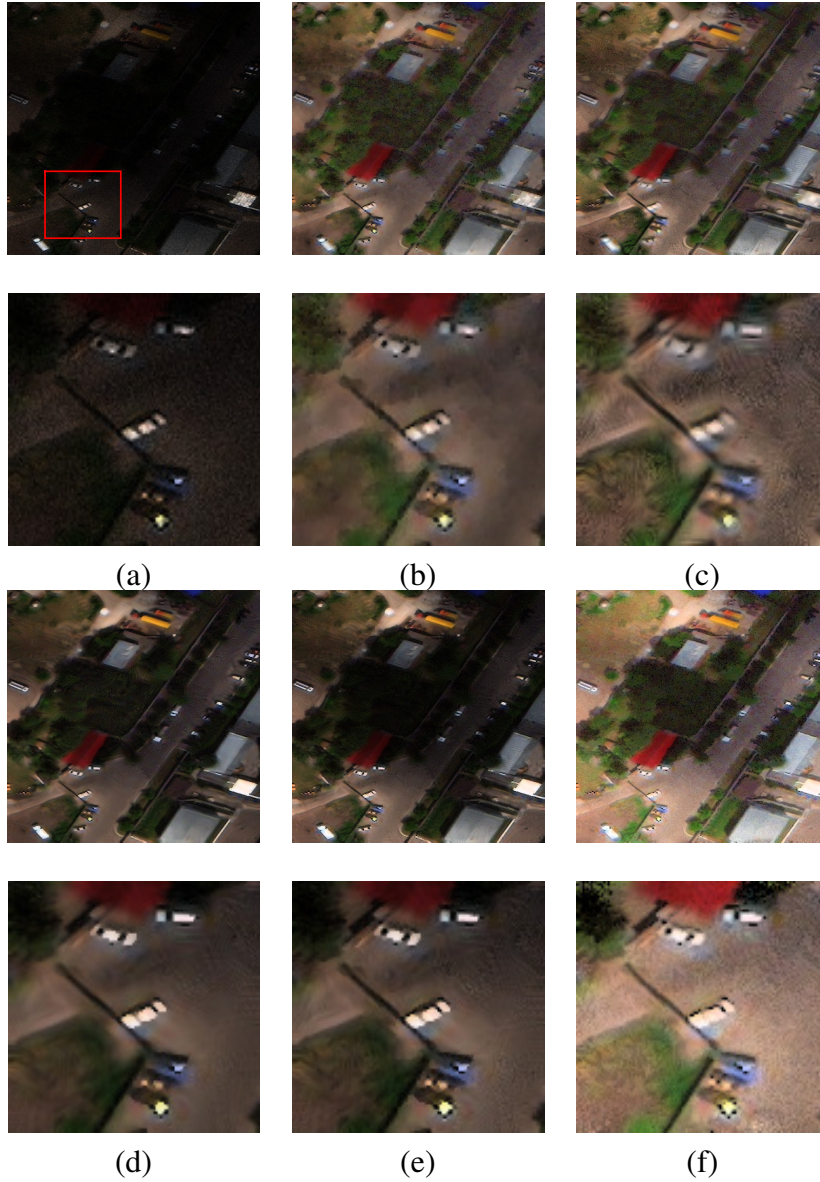
Figure 4.4 xView image 2 with Poisson: restoration results and corresponding enlarged portions below it (a) Input image (b) Restored using Fast TV+CLAHE (Wang and He, 2017) (c) Restored using NLTV+CLAHE (Gilboa and Osher, 2008) (d) Restored using NLTVR+NLTV (Zosso et al., 2015) (e) Restored using PVM+NLTV (Huifang Li and Shen, 2012) (f) Restored using Proposed method.
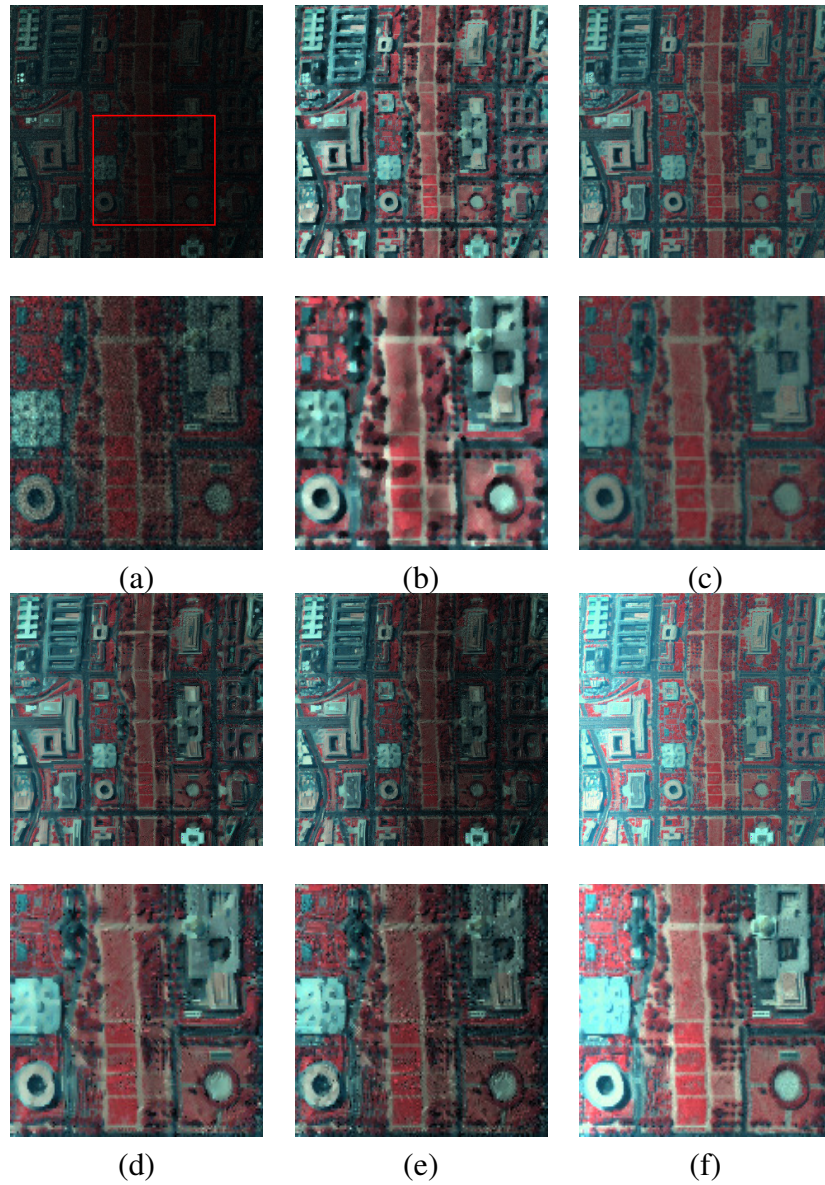
Figure 4.5 Washington DC image with Poisson : restoration results and corresponding enlarged portions below it (a) Input image (b) Restored using Fast TV+CLAHE (Wang and He, 2017) (c) Restored using NLTV+CLAHE (Gilboa and Osher, 2008) (d) Restored using NLTVR+NLTV (Zosso et al., 2015) (e) Restored using PVM+NLTV (Huifang Li and Shen, 2012) (f) Restored using Proposed method.
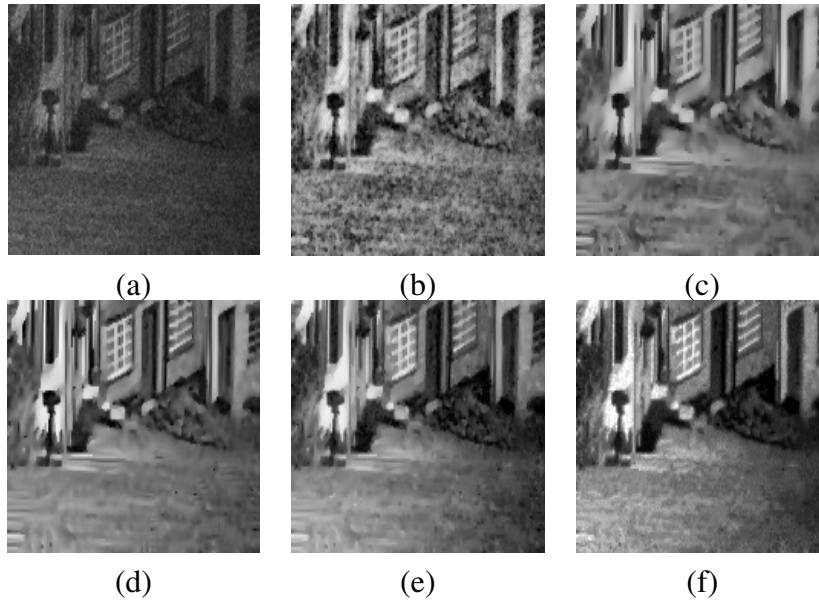
Figure 4.6 Optical image with Poisson noise peak=30: (a) Input image (b) Restored using Fast TV+CLAHE (Wang and He, 2017) (c) Restored using NLTV+CLAHE (Gilboa and Osher, 2008) (d) Restored using NLTVR+NLTV (Zosso et al., 2015) (e) Restored using PVM+NLTV (Huifang Li and Shen, 2012) (f) Restored using Proposed method.

of denoising. As the value decreases, the restoration gets improved. Whereas a high value of AG implies better spatial resolution (Li et al., 2017). According to Table 4.1, the FastTV+CLAHE is giving comparable performances in some synthetically noisy inputs, and the performance of PVM+NLTV is also on par with the proposed method in original noisy data (Pines, Jasper Ridge); however, the proposed method displays consistently better performance for all images. The measures in Table 4.1 check the naturalness of the image and its clarity; hence, the higher performance here implies the better restoration. To measure the quality of details preservation, we have evaluated the discrete entropy of the image. Generally, entropy measures information content; hence, higher entropy values imply the presence of more details in the filtered image. Table 4.3 gives a comparison of discrete entropy values. As inferred from this table, the details preservation capability of the proposed strategy is dominant than all other methods under study. Table 4.3 also shows the comparison of GCF among different methods. It is a global measure of contrast, and it is stated to be more close to the human perception of contrast (Matkovic et al., 2005). It operates in different scales of resolution to get local contrast information and a weighted average of which will be calculated as GCF. A high value of this measure implies an improvement in the contrast

and high visibility of the details. According to Table 4.3, the proposed methodology has a higher GCF for all images. Table 4.2 describes the visual descriptors obtained for different methods. The e and r̄ values are high if the restored results have high visibility and σ is less when the number of saturated pixels is less. In light of these results, we observe that the proposed model outperforms the other ones. Finally, Table 4.4 includes the time taken by different algorithms for restoration. As evident from this table, the proposed method converges faster.

In addition to the remote sensing images, the performance on natural image (optical image) is demonstrated in Figure 4.6, and it is observed that the denoising and enhancement obtained by the proposed algorithm are on par with the other methods. The results obtained on real noisy input images are represented in Figure 4.7 and Figure 4.8. The noisy bands (3, 110, 204), Indian Pines dataset (http://lesun.weebly.com/hyperspectral-data-set.html), and (4, 107, 153), Jasper Ridge dataset has been used here for the evaluation. The performance of comparing algorithms on each band is shown in the subfigures. The first row of the figure is showing all noisy bands, and the last column in this figure represents the false colour image formed using all these bands. In case of a regular RGB image, the proposed algorithm can be applied in each band as depicted herein but this leads to color distortions in the input data, in order to reduce this colour discrepancy, operation in the HSV domain is recommended. As inferred from the experimental study, the proposed method is prominent in preserving textures and other details present in the input while denoising and enhancing the data.

4.4   Summary of the Chapter

In this Chapter, a novel framework is designed for enhancing and restoring Poisson corrupted images. The data-correlated Poisson noise and contrast unevenness are handled using a perceptually driven retinex model under the variational framework. Fast numerical implementation under the spilt-Bregman method improves the convergence. The results both visual/quantitative-statistical shown in favour of the proposed model

Table 4.1 AG and NIQE evaluated for various methods

Images	Quality metrics	Fast TV+CLAHE (Wang and He, 2017)	NLTV+CLAHE (Gilboa and Osher, 2008)	NLTVR+NLTV (Zosso et al., 2015)	PVM+NLTV (Huifang Li and Shen, 2012)	Proposed method
Washington DC	AG	48.6268	38.9858	45.2348	41.4343	**50.0104**
	NIQE	5.7783	5.4592	6.2676	6.2449	**5.3555**
xView 1	AG	22.2802	30.3130	24.4006	21.0895	**31.8546**
	NIQE	6.1672	6.6492	6.6822	6.7088	**6.1458**
xView 2	AG	22.7537	26.7697	21.8139	20.9387	**53.6950**
	NIQE	5.2839	6.6844	5.1235	5.1579	**5.1215**
Pines	AG	50.4822	51.7613	51.1983	50.8462	**59.2906**
	NIQE	39.8003	39.8643	39.8002	39.7995	**39.7994**
Jasper Ridge	AG	34.8662	38.7902	38.8006	34.1701	**38.9568**
	NIQE	38.4545	39.8014	39.8006	**39.8001**	39.8001

Table 4.2 Visual descriptors evaluated for various methods

Images	Quality metrics	Fast TV+CLAHE (Wang and He, 2017)	NLTV+CLAHE (Gilboa and Osher, 2008)	NLTVR+NLTV (Zosso et al., 2015)	PVM+NLTV (Huifang Li and Shen, 2012)	Proposed method
Washington DC	e	-0.1895	-0.1523	-0.1597	-0.1597	**-0.1521**
	$\bar{r}$	3.554	2.5294	2.8437	2.3719	**3.8885**
	σ	0.0130	0.0116	0.0485	0.0134	**0.0109**
xView 1	e	-0.5065	-0.2536	-0.2963	-0.1738	**-0.1729**
	$\bar{r}$	2.4125	2.8910	1.9283	1.4186	**3.3906**
	σ	**0.00**	**0.00**	0.0139	0.1466	**0.00**
xView 2	e	-0.5056	-0.2818	-0.3680	-0.2794	**-0.2426**
	$\bar{r}$	2.9659	2.7704	2.1440	1.7779	**3.2680**
	σ	**0.00**	**0.00**	0.0763	0.0025	**0.00**
Pines	e	0.0154	0.0156	0.0101	0.0156	**0.0188**
	$\bar{r}$	1.4931	1.4714	1.5605	1.4702	**1.7049**
	σ	0.0183	0.0250	0.0110	0.0146	**0.0101**
Jasper Ridge	e	-0.0384	-0.0325	-0.0336	-0.0368	**-0.0273**
	$\bar{r}$	1.1681	1.1643	1.2513	1.1797	**1.2625**
	σ	0.5030	0.6110	0.1500	0.5533	**0.0121**

Table 4.3 GCF and EM evaluated for various methods

Images	Quality metrics	Fast TV+CLAHE (Wang and He, 2017)	NLTV+CLAHE (Gilboa and Osher, 2008)	NLTVR+NLTV (Zosso et al., 2015)	PVM+NLTV (Huifang Li and Shen, 2012)	Proposed method
Washington DC	GCF	6.8124	6.1452	6.6792	6.6731	**6.8423**
	EM	7.4730	6.9371	7.1578	7.1176	**7.6097**
xView 1	GCF	5.7280	6.1470	7.2725	7.1195	**7.7424**
	EM	6.9791	6.1294	6.6822	6.4970	**7.6940**
xView 2	GCF	5.9825	6.5800	7.2038	7.5713	**7.6093**
	EM	7.0026	7.1094	6.8778	6.8838	**7.6475**
Pines	GCF	7.6881	6.5214	6.5945	8.4802	**8.5215**
	EM	7.6044	7.6391	7.7819	7.7722	**7.8388**
Jasper Ridge	GCF	7.0671	6.0351	6.1817	7.5104	**8.7325**
	EM	7.1104	7.3915	7.6713	7.6708	**7.6730**
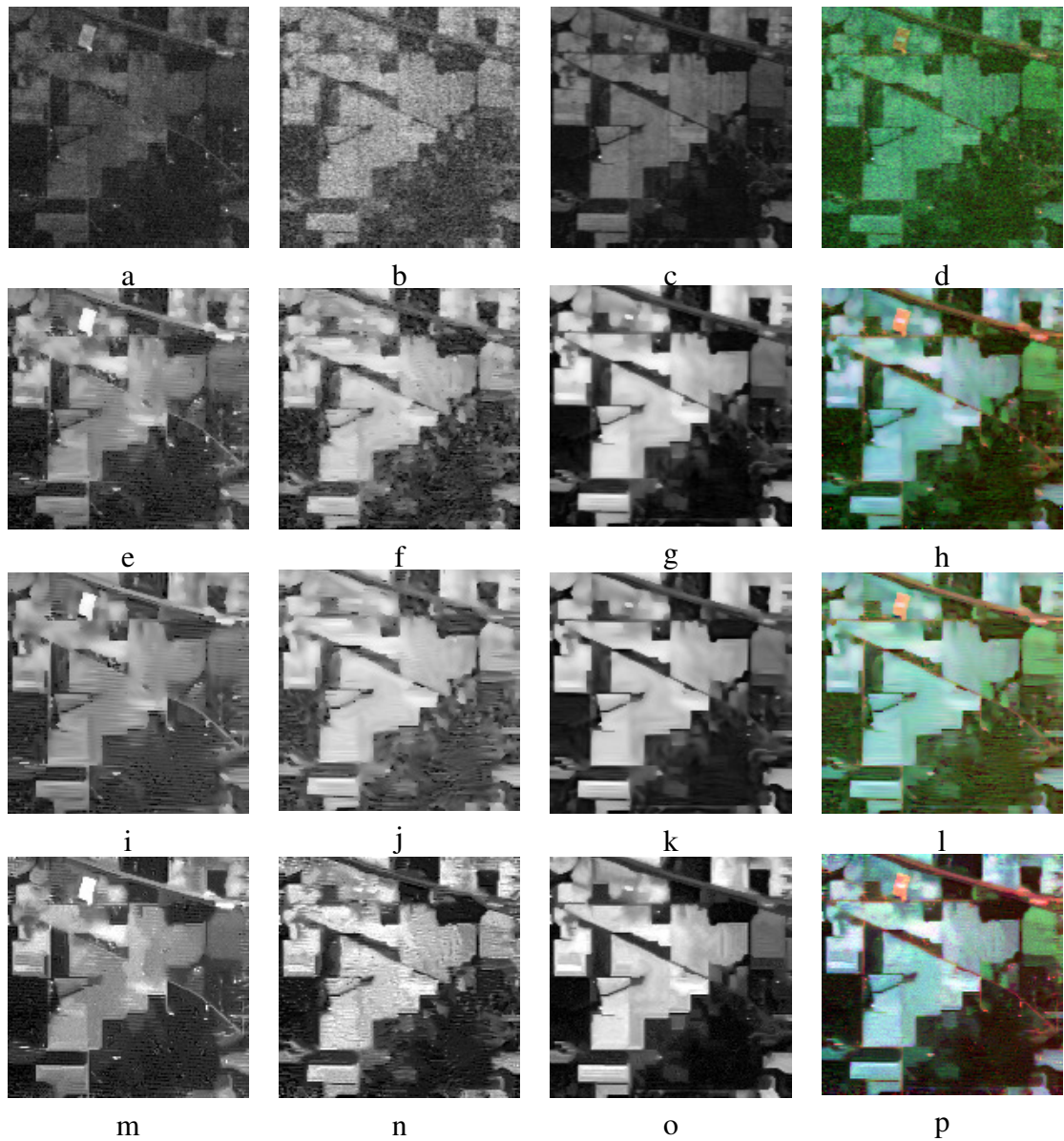
Figure 4.7 Results on low contrast noisy bands of Indian Pines (AVIRIS, 145×145 pixels, 224 spectral reflectance bands, wavelength range: 0.4 - 2.5 10^{-6} meters), courtesy MultiSpec : (a) Input low-contrast noisy Band 3 (b) Input low-contrast noisy Band 110 (c) Input low-contrast noisy Band 204 (d) Noisy False color image, PVM+NLTV: (e) Band 3 restored (f) Band 110 restored (g) Band 204 restored (h) restored false color image, NLTVR+NLTV: (i) Band 3 restored (j) Band 110 restored (k) Band 204 restored (l) restored false color image, Proposed: (m) Band 3 restored (n) Band 110 restored (o) Band 204 restored (p) restored false color image.

endorses efficiency of the model and votes for its applicability in real-time applications.
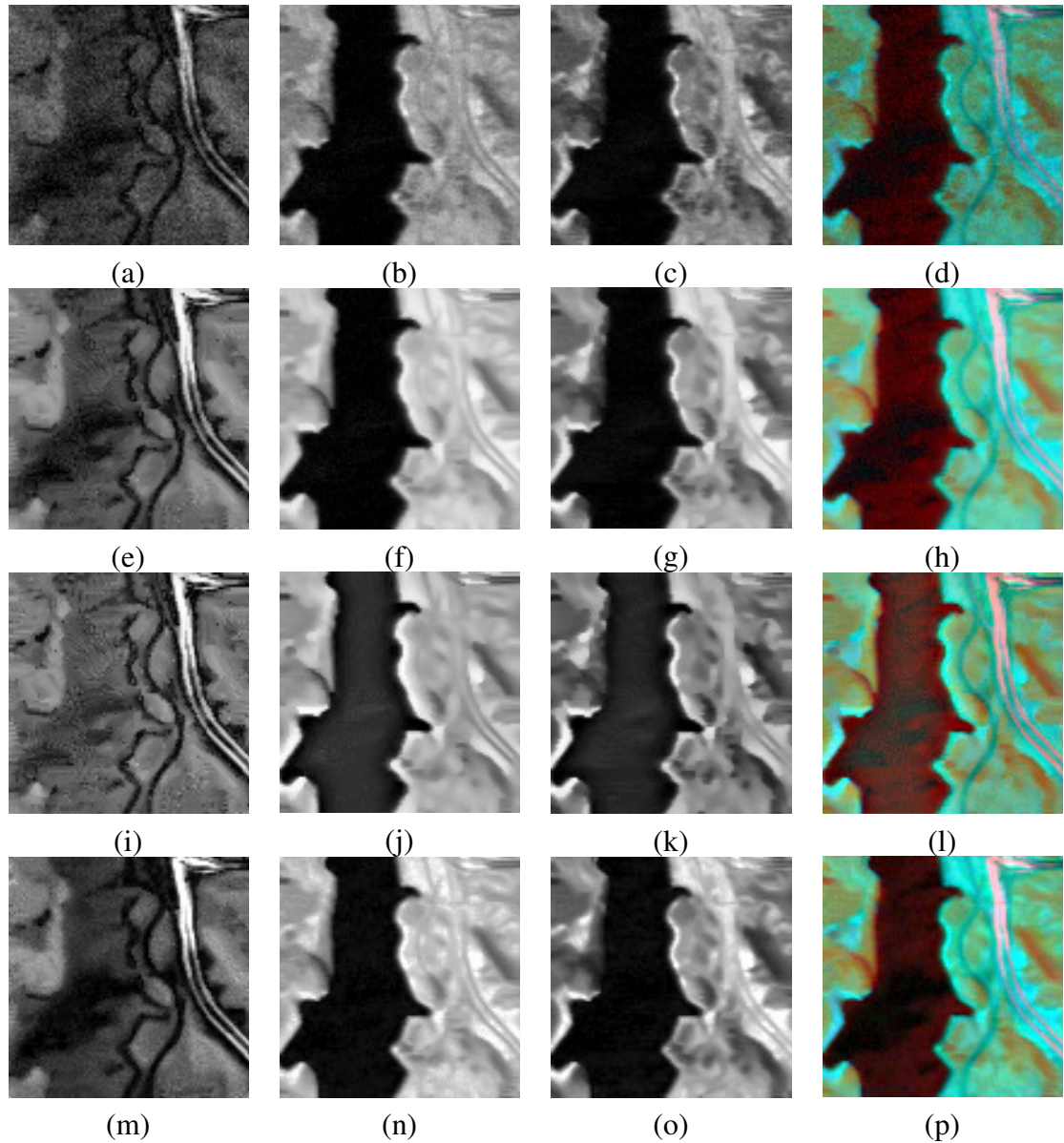
Figure 4.8 Results on low contrast noisy bands of Japser Ridge (Zhu et al., 2014) (subimage of 100×100 pixels, 224 bands, wavelength range: 380 nm to 2500 nm): (a) Input low-contrast noisy Band 4 (b) Input low-contrast noisy Band 107 (c) Input low-contrast noisy Band 153 (d) Noisy False color image, PVM+NLTV: (e) Band 4 restored (f) Band 107 restored (g) Band 153 restored (h) restored false color image, NLTVR+NLTV: (i) Band 4 restored (j) Band 107 restored (k) Band 153 restored (l) restored false color image, Proposed: (m) Band 4 restored (n) Band 107 restored (o) Band 153 restored (p) restored false color image.

Table 4.4 Time taken by different methods in seconds

Images	Fast TV+CLAHE (Wang and He, 2017)	NLTV+CLAHE (Gilboa and Osher, 2008)	NLTVR+NLTV (Zosso et al., 2015)	PVM+NLTV (Huifang Li and Shen, 2012)	Proposed method
Washington DC	5.4706	6.1788	26.5439	7.6272	**3.3718**
xView 1	6.0304	8.9574	163.0553	11.3595	**4.0991**
xView 2	6.0094	8.9712	129.1649	11.2597	**4.1921**

CHAPTER 5

Perceptually inspired framework for despeckling

5.1 Introduction

Ultrasound (US) imaging is a diagnostic imaging technique to visualize various subcutaneous body structures such as muscles, vessels, joints etc., for detecting or diagnosing the pathological symptoms. There are essentially four different modes of scanning as far as ultrasound sonography is concerned. Among them, B-mode sonography is more popular due to its extent of applicability and wide range of acceptance among the medical imaging community for diagnostic purpose. The extensive used of US imaging is justified by its non-invasive and non-ionizing nature of characterizing of the tissues. The US scanning system sends acoustic signals to probe the nature of tissues in the human body and based on the reflected pattern the images are formed. Since the acoustic signals used for probing the tissues result in constructive and destructive interferences causing high and low amplitude deflections in the magnitude of the captured data, usually coined as speckles Michailovich and Tannenbaum (2006). A speckle by its sheer nature is data correlated and cannot be neglected like the other noise interventions Michailovich and Tannenbaum (2006). Speckles are not completely noise components though apparently they seem to be. They carry information about the tissue. However, their presence results in spurious analysis by the medical experts. The low-amplitude signals are sometimes treated as blood vessels though they are formed due to the destructive interference of the waves.

The statistical filters were introduced to effectively address the multiplicative speck-

led interference in many previous works. The pioneer works in this field are Lee filter Lee (1980), Frost filter Frost et al. (1982) and Kuan filter Kuan et al. (1985). The extent of averaging in these filters depends on the coefficient of variation of the image. The areas with high variance are smoothened at a lesser magnitude compared to the low variance regions which are categorically smooth in nature. This property in turn preserves the structures. The minimum mean square filter based on the local variance introduced by Weiner Ekstrom (1982) is another similar approach in this direction. Nevertheless, these filter duly neglect the noise distribution in the input and the correlated nature of the noise to a large extend. These issues are addressed in their subsequent modifications.

Anisotropic diffusion models inspired by the Perona-Malik model Perona and Malik (1990) has apparently changed the outlook of the image restoration framework. The Perona-Malik model is a non-linear diffusion model whose diffusion coefficient is controlled by a non-linear function of the gradient term (i.e. $I_t = div(C(|\nabla I|)\nabla I)$, where $I_t = \frac{\partial I}{\partial t}$ and the diffusion coefficient $C(x) = \frac{1}{1+(x/K)^2}$). The models such as speckle reducing anisotropic diffusion (SRAD) Yu and Acton (2002), oriented SRAD (OS-RAD) Krissian et al. (2007) and direction preserving AD (DPAD) Aja-Fernandez and Alberola-Lopez (2002) are the notable anisotropic diffusion models introduced for despeckling images. These filters incorporate the statistical feature, such as, coefficient of variation as the driving force of the diffusion process (or the diffusion coefficient function $C(.)$ is a function of coefficient of variation). The diffusion magnitude is controlled by the coefficient of variation which depends on the local mean and variance of the data. For instance, the instantaneous coefficient of diffusion serves as the edge detection function in Yu and Acton (2002) and the eigenvectors of the structure tensor are used to control the magnitude of diffusion in Krissian et al. (2007). The eigenvector in the principal major direction is smoothed less compared to the principal minor direction in case of a 2D matrix. This eventually results in despeckling with less penalization of the structures. There are certain advancements suggested for these filters as well Bini and Bhat (2014); Jidesh and Bini (2017) to improve their performance in terms of image restoration. In Bini and Bhat (2014), the authors propose a speckle reducing model where a speckle reducing edge detector is embedded in the well known

"Geodesic snakes" model. Similarly, in Jidesh and Bini (2017) the authors introduce a complex diffusion driven diffusion coefficient to drive the process. However, these filters too ignore the distribution of the noise at large.

Thresholding schemes are employed in large scale in image restoration applications. Especially, multi-resolution models have captured the attention lately and they are extensively employed in image restoration. For instance, wavelet models are prominent in this regard. The wavelet decomposition approximates a scale space representation of the data Xizhi (2008). The noise also gets represented in the scale space domain and an appropriate thresholding scheme should effectively remove noise features. Hard and soft (adaptive) thresholding schemes are proposed in the literature to effectively handle the noise interventions. Apart from wavelet models, other advanced version such as curvelet has also been proposed for restoration activities in the literature, see Li et al. (2011) for details.

These methods converts the original image into a logarithmic domain and make use of the Gaussian distribution assumption of sub-band coefficients. One of the main drawbacks here is related to the inaccuracy in choosing appropriate threshold. Later, several researchers proposed methods for advancement in threshold selection which includes the nonlinear estimator proposed in Simoncelli and Adelson (1996). Recently a multi directional 2-D Eigen filter approach for ultrasound denoising is proposed in Nagare et al. (2017). This method uses Translation Invariant Pyramidal Directional filter Bank (TIPDFB) to decompose the image and thresholding applies on all these sub-bands to remove noise. All of the multiscale methods use the Gaussian distribution assumption in log domain instead of incorporating speckle characteristics in the denoising process.

We recall from chapter 1 that the total variation regularization is a well known variational model for image restoration, see Rudin et al. (1992) for the details. The total variation norm of the function I is defined in the space of Bounded variation (BV) in which the total variations are bounded (i.e. $BV(\Omega) := \int_\Omega |\nabla I| d\Omega < \infty$). The TV minimization model takes the form:

$$E(I) = \min_{I \in BV(\Omega)} \|\nabla I\|_{TV} + \lambda \|I - I_0\|. \tag{5.1.1}$$

As already pointed out, the linear approximation of the model results in undesired ef-

fected in the restored output. Moreover, the model assumes a Gaussian distributed white noise intervention in the data. Nevertheless, such an assumption limits the applicability of the model to various real-time imaging applications especially from medical imaging domain. A notable modification to this model to incorporate the multiplicative Gamma noise is introduced in Aubert and Aujol (2008). Here a Bayesian formulation is explored for reinterpreting the minimization problem as a posterior probability minimization model and the prior in the model is assumed to follow the distribution of the noise. The model is found to perform well in case of multiplicative speckled following a Gamma law. Many variant thoughts in this direction is seen in works Huang et al. (2010) and Xiao et al. (2010). However, these methods too are not efficient enough to maintain small textures and details present in the data, even though they ensure the preservation of edge details. To address this issue to a considerable extent, a new category of variational methods were introduced, which is based on the non-local total variation framework proposed in Gilboa and Osher (2008). Some variations of this model is found in Liu and Huang (2014) and Jidesh and Balaji (2018), where the latter work proposes a nonlocal total bounded variation regularization model for speckle removal. Compared to other methods the non-local total variation algorithms have succeeded in ensuring the efficiency in retaining small details and textures. In Mei et al. (2020), authors proposed a combination of diffusion and TV filters where a phase asymmetry measure for edge detection is being used to distinguish edges and constant intensity regions.

5.1.1 Speckles in ultrasound data

The ultrasound image formation is based on the reflection of acoustic signals from various tissues in the human body. The constructive and destructive interferences of the wave send to probe the details can lead to unexpected amplification of the amplitude. The noise introduced due to the interference of the waves are analysed in many ultrasound images using the machine learning algorithm given in Chapter 2. The noise analysis shows the distribution to be closely in line with the Gamma distribution following the PDF (1.1.5). The analytical study on various images obtained from the US imaging repository (`http://splab.cz/en`) have shown that the noise distribution fol-

(a)   (b)
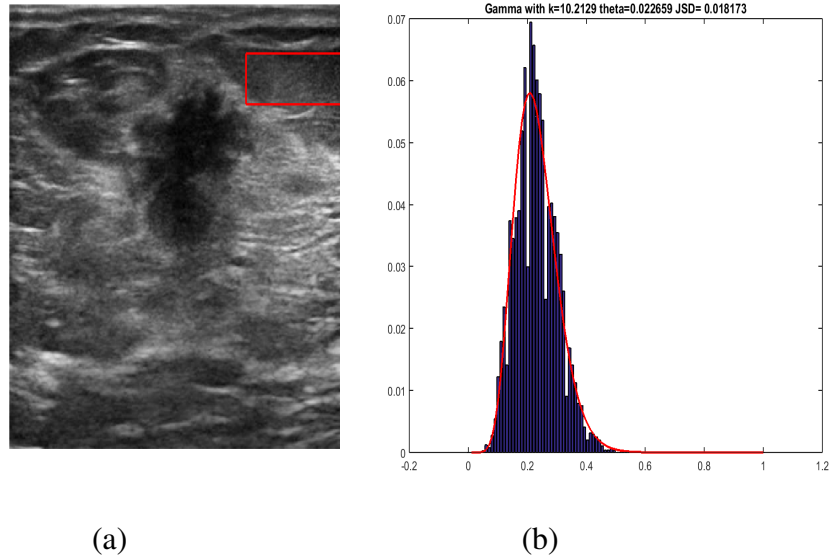
Figure 5.1 (a) Original noisy US image (b) Noise fitting done on area marked

lows Gamma law. A curve fitted from the obtained PDF with a Gamma curve (whose parameters are estimated) is shown in Figure 5.1.

Many of the models discussed so far seek to find a despeckling solution that eventually retains the edges and other details present in the data to a considerable extend. Nevertheless, the images captured under the US modality are observed to be deficient in contrast aspects. An uneven contrast distribution duly hinders the subsequent analysis phase spoiling the diagnosis and detection phase of the automated systems. This has been a matter for concern among the research community. The untiring efforts in addressing the uneven distribution of the data resulted in retinex based models, which are extensively used in low contrast photography reconstruction algorithms. This study is intended to address the uneven-contrast aspect of speckled images which are otherwise unexplored to a deserving extent. An effective despeckling and contrast enhancement is the need of the hour.

5.2 The proposed retinex model

As studied in many previous works the distorted image is represented as $I_0 = I \times n$, where n is multiplicative data-correlated noise. The noise distribution is observed to follow a Gamma law. This claim has been substantiated in the experimental section of this chapter using the distributional characteristics of the noise components present in

the homogeneous intensity regions of the image. Now using the Bayesian framework under the assumption of a Gamma distribution of th likelihood and nonlocal TV norm as the prior we have:

$$\min_I \{-\log(P(I|I_0))\} = \min_I \left\{ \log(I) + \frac{I_0}{I} + \lambda \phi(I) \right\}. \tag{5.2.1}$$

Here $\lambda \in (0, \infty)$ denotes the positive scalar regularization parameter and further, we take the log of prior probability function as $\log P(I|I_0) = -(log(I) + I_0/I)$, the readers are directed to refer Aubert and Aujol (2008) for the derivation of the same.

With the assumptions made above, the model proposed is represented as:

$$\min_{l,r,i} \{E(l,r,i)\} = \lambda_0 \int_\Omega \|\nabla l\|_2^2 dxdy \tag{5.2.2}$$

$$+ \lambda_1 \int_\Omega W(r) \|\nabla \hat{r}\| dxdy$$

$$+ \lambda_2 \int_\Omega (exp(r) - 1/2)^2 dxdy$$

$$+ \lambda_3 \int_\Omega (W(i) \|\nabla \hat{i}\| + \beta \|i\|_2^2) dxdy$$

$$+ \lambda_4 \int_\Omega (r - i + l)^2 dxdy$$

$$+ \lambda_5 \int_\Omega log(I) + (I_0/I).$$

Inspired form previous variational methods this model also evaluates the L_2 norm of illumination to ensure its smoothness. Since the reflectance part of the image contains more textural informations, the weighted non-local TV is employed in this study. Unlike the regularization described in Chapter 4, a weighted non-local Total bounded variation (TBV) of intensity matrix is employed here to eliminate the noise present in images. The intensity regularization term used here is a combination of NLTV and L^2 norm. As the value value of β increases the smoothing of i increases. Hence, TBV is efficient in giving better results in heavily noisy data. The drawback of using L^2 norm is it does not care about the edges and details in image which is addressed by NLTV term in TBV. As observed by Kimmel et al. (2003), the reflectance is in the range $[0, 1]$ and the term $(exp(r) - 1/2)^2$ forces it to be close to the average value in the minimization model. The term $(r - i + l)$ ensures the intensity matrix evaluated in each step is a combination of corresponding r and l estimates and vice versa. The intensity smoothing is constrained by the term $\int_\Omega log(I) + (I_0/I)$ which denotes the data fidelity. The term is conditionally convex (ie convex if $2I_0 > I$.) and is derived using the Bayesian MAP estimator under

the assumption of a Gamma distributed noise in the input image (see Appendix A for the details). This term tends to retain more textures and small details while reducing the speckle and enhancing the input. The reflectance and intensity are assumed to be the properties of the object being imaged and hence they are expected to carry non-smooth information. Therefore, the Weberized-TV norm is employed to ensure proper retaining of the structures and enhancement of the contrast. The luminance being the property of the source, L^2 norm is employed to ensure its smooth transition. Since the optimization framework contain six different terms, solving all terms in one stretch is practically tedious. As one term influences the other one, one needs to seek for a solution by variable separation method. A split scheme comes handy in such situations.

The optimization problem in equation (5.2.2) shall be split into three separate minimization problems (in terms of the three quantities r, l and i) as given below:

$$\min_r\{E(r)\} = \lambda_1 \int_\Omega W(r)\|\nabla \hat{r}\| dxdy \tag{5.2.3}$$
$$+ \lambda_2 \int_\Omega (exp(r) - 1/2)^2 dxdy$$
$$+ \lambda_4 \int_\Omega (r - i + l)^2 dxdy,$$

$$\min_i\{E(i)\} = \lambda_3 \int_\Omega (W(i)\|\nabla \hat{i}\| + \beta \|i\|_2^2) dxdy \tag{5.2.4}$$
$$+ \lambda_4 \int_\Omega (r - i + l)^2 dxdy$$
$$+ \lambda_5 \int_\Omega log(I) + (I_0/I) dxdy,$$

n and

$$\min_l\{E(l)\} = \lambda_0 \int_\Omega \|\nabla l\|_2^2 dxdy \tag{5.2.5}$$
$$+ \lambda_4 \int_\Omega (r - i + l)^2 dxdy.$$

These equations are to be solved iteratively to get the final result.

5.2.1 Numerical Implementation

There are various alternating minimization approaches for solving the above mentioned problem. The numerical solutions seeks for a solution which converges at a higher rate. Given many such implementations such as alternating method Chan et al. (2011), projection method Chambolle and Pock (2010), primal-dual method Perona and Malik

(1990), Bregman method Goldstein et al. (2010) etc., we chose the split-Bregman solution for the reason that it provides a stable solution with good convergence rate and less parameter sensitivity. Therefore, the above equations (5.2.3), (5.2.4), and (5.2.5) are solved using the Split-Bregman numerical optimization technique, see Goldstein et al. (2010) and Liu and Huang (2010) for more details. It is based on the idea of minimizing the Bregman distance. For any convex function J the Bregman distance between two points m and n is defined as

$$D_J^g(m,n) = J(m) - J(n) - <g, m - n>,$$

where g is the sub-gradient of J at point n. According to split Bregman iteration we introduce new constrains as $a = \nabla \hat{r}$ and $b = \nabla \hat{i}$ along with auxiliary variables d_1 and d_2, then the equation (5.2.3) and (5.2.4) get transformed as

$$\min_r \{E(r)\} = \lambda_1 W(r)\|a\| \tag{5.2.6}$$
$$+ \lambda_2 (exp(r) - 1/2)^2$$
$$+ \lambda_4 (r - i + l)^2$$
$$+ \lambda \|a - \nabla \hat{r} - d_1\|_2^2$$

and

$$\min_i \{E(i)\} = \lambda_3 (W(i)\|b\| + \beta \|i\|_2^2) \tag{5.2.7}$$
$$+ \lambda_4 (r - i + l)^2$$
$$+ \lambda_5 log(I) + (I_0/I)$$
$$+ \alpha \|b - \nabla \hat{i} - d_2\|_2^2,$$

The above equations can be further split as given below (We are assuming $\lambda_1 = 1$ and $\lambda_3 = 1$).

$$r^{k+1} = \min_r \left\{ \lambda_2 (exp(r) - 1/2)^2 + \lambda_4 (r - i + l)^2 \tag{5.2.8} \right.$$
$$\left. + \lambda \|a - \nabla \hat{r} - d_1^k\|_2^2 \right\},$$
$$a^{k+1} = \min_r \left\{ W(r)\|a\| + \lambda \|a - \nabla \hat{r} - d_1^k\|_2^2 \right\}, \tag{5.2.9}$$
$$i^{k+1} = \min_i \left\{ \lambda_5 (log\, I + (I_0/I)) + \beta \|i\|_2^2 + \lambda_4 (r - i + l)^2 \tag{5.2.10} \right.$$
$$\left. + \alpha \|b - \nabla \hat{i} - d_2^k\|_2^2 \right\},$$

and

$$b^{k+1} = \min_i \left\{ W(i) \, \|b\| + \alpha \|b - \nabla \hat{i} - d_2^k\|_2^2 \right\}, \tag{5.2.11}$$

The auxiliary variables d_1 and d_2 gets updated after each corresponding Bregman iteration as follows:

$$d_1^{k+1} = d_1^k + (\nabla \hat{r} - a^{k+1}). \tag{5.2.12}$$

and

$$d_2^{k+1} = d_2^k + (\nabla \hat{i} - b^{k+1}). \tag{5.2.13}$$

The Euler-Lagrange is applied on equation (5.2.8) and (5.2.10) to evaluate the derivative of the functional which is later solved using Fourier transform. The iterative procedure for restoration is given in Algorithm 3.

Algorithm 3 Algorithm to implement the method

    Input $I_0 \leftarrow$ Noisy ultrasound image
    Output Restored ultrasound image I

1: Initialize $k = 1, \varepsilon = 0.0001, a^1 = 0, d_1^1 = 0, b^1 = 0, d_2^1 = 0, i^1 = log(I_0), l^1 = \max(i^1), and \, r^1 = (l^1 - i^1)$

2: **while do**$\|i^k - i^{k-1}\|/\|i^k\| < \varepsilon$

3:     $a^{k+1} = shrinkage(\nabla \hat{r} + d_1^k, \frac{W(r)}{\lambda})$,
        where $shrinkage(x, \theta) = \frac{x}{|x|} \max(|x| - \theta, 0)$.

4:     $r^{k^1} = \mathbb{F}\left\{ \frac{\lambda_4 F(i-l) - \lambda_2 F((E(r) \, (E(r) - 1/2))) - \lambda F(\nabla . (a - \nabla \hat{r} - d_1^k))}{\lambda_4} \right\}$
        (where E denoted exp function, $k^1 := k + 1$, and $\mathbb{F}$ is the inverse Fourier transform)

5:     update d_1^{k+1} using equation (5.2.12)

6:     $b^{k+1} = shrinkage(\nabla \hat{i} + d_2^k, \frac{W(i)}{\alpha})$.

7:     $i^{k+1} = \mathbb{F}\left\{ \frac{\lambda_5 F(I_0/I) - \lambda_4 F(r+l) - \alpha F(\nabla . (b - \nabla \hat{i} - d_2^k))}{F((\lambda_5/i) + \beta - \lambda_4)} \right\}$.

8:     update d_2^{k+1} using equation (5.2.13)

9:     $l^{k+1} = \mathbb{F}\left\{ \frac{\lambda_4 F(i-r)}{F(\lambda_4 + \lambda_0 \Delta)} \right\}$.

10: **end while**

11: update I as exponential of $e^{(l+r)}$

5.3 Experimental Results and Analysis

For the experimental evaluation we use the Ultrasound image dataset provided by Signal Processing Laboratory (http://splab.cz/en/download/). This dataset includes B-mode ultrasound images of common carotid artery (CCA). For comparative study we use the

popular despeckling algorithms like SRAD Yu and Acton (2002), DPAD Aja-Fernandez and Alberola-Lopez (2002), OBNLM Coupe et al. (2009), NLTBV Gilboa and Osher (2008), ADMSS Ramos-Llorden et al. (2015), PFDTV Mei et al. (2020), and Eigen-filter Nagare et al. (2017).

The restoration results obtained by various comparing methods are given in Figure 5.2, 5.3, and 5.4, for a visual comparison. In Figure 5.2, the details present in the image is missing in most of the restoration results except the proposed method. The performance given by Eigen-filter is comparatively better but the enhancement capability of the proposed algorithm has succeeded in retaining even the small details. Similar kind of performance is visible in Figure 5.3 also, where the details in the upper end of the image is least preserved by OBNLM. The restoration results obtained using Eigen-filter (Nagare et al. (2017)) appears low in contrast and blurry whereas, the proposed algorithm gives a better contrast enhancement and denoising at the same time which makes this result superior to the other comparative models. The better contrast of these results eventually helps to perform an accurate decision making process . The same performance pattern is visible in Figure 5.4 also.

Performance comparison on a artificially noisy synthetic image is depicted in Figure 5.5. The noisy input is given in sub-figure (a) of the same figure, where speckle noise of variance 0.25 is used to degrade the image. As observable from the results, the presence of speckle noise has degraded the contrast of the image as well. Most of the diffusion based comparing algorithms such as SRAD, DPAD, and ADMSS gives poor contrast enhancement, see sub-figures (b), (c), and (f). The OBNLM has considerably done well in maintaining proper contrast, but as seen in Figure 5.5(d), along with the smoothing (due to the speckles) some artefacts are introduced in restored image. Similarly, NLTBV method also restores the original contrast of the image to some extent. The denoising achieved in low intensity areas is remarkable, however, in high-intensity areas the performance is moderately degraded. The restoration provided by Eigen-filter method is good in suppressing the noise and restoring the contrast aspects of the data, but the resultant image appears blurred with minimal sharp details or textures. On the contrary, the PFDTV result gives sharp edges and details but contrast between the

dark pixel regions like the back square and the background is very low. Comparatively the method proposed herein gives a better performance even in case of highly corrupted data by giving comparable performance in low and high intensity regions, see sub-figure (h). This method preserves edges and other sharp details efficiently and the contrast improvement achieved assists the analysis of real scan-images, as it reveals the hidden details which are otherwise unobserved. The same performance pattern is visible in restoring a one dimensional signal too, refer Figure 5.6. Here subfigures (b), (c), and (f) represent the SRAD, DPAD, and ADMSS results, respectively, where the restored signal (Green) appears noise-free, but the amplitude or pixel values are getting diminished in the restored data. The range of output amplitude is also reduced to [0-50], which indicates a degradation in contrast. Moreover, unlike the noisy input signal (Red), the shifts from different pixel levels are not sharp in the output, and the lines are mostly straight, which indicates the poorly preserved edges and textures. The OBNLM result given in subfigure (d) is not shown to degrade the pixel values, but the denoising performance is considerably low. The subfigure (e) provides the result of NLTBV, where the denoising of high pixel values (corresponds to bright areas in a 2D image) is compromised. Nevertheless, denoising of the rest of the parts appears comparatively better. The subfigure (g) shows the PFDTV result, where it succeeds in preserving sharp edges, but the black region is not distinguishable from the background. The Eigenfilter result given in subfigure (h) succeeds in removing noise; however, texture preservation capability seems low. The output pixel values are slightly reduced in this result, especially in high-intensity regions. The proposed result is given in subfigure (h), which improves the contrast of the output by enhancing the intermediate intensity levels, which intern makes the darker regions bright for better visibility. As speckle noise contains useful information, the textures in noisy input (red) are well preserved in this result and edges are also properly retained.

The parameter values used for the experiments are $\lambda = 1.4, \alpha = 0.2, \lambda_0 = 0.1, \lambda_2 = 8, \lambda_4 = 800, \lambda_5 = 0.001, \beta = 0.2$. These parameters are set based on various experimental studies performed with various image dataset. An adaptive selection of them are still an open problem which is being investigated as a future work. The detailed parameter

analysis is conducted on the basis of quality matrices to fix the value which is given in Figure 5.7.

Various quality metrics are used in this study to analyse the performance of various methods used for comparative study along with the proposed method. The details of these measures and the expression for evaluating them are provided in Appendix A). The metrics are chosen to establish the performance of various models in terms of various parameters such as noise reduction, contrast enhancement etc. The Equivalent Number of Looks (ENL) is a well known blind quality metric to evaluate despeckling filters Gomez et al. (2017). The higher value of ENL indicate better speckle removing capability. We have evaluated the same for different region of interests (ROI) and the proposed method has consistently proved to give higher value in all cases. The ENL value obtained for one particular ROI is given in Table 5.1. The methods such as Eigenfilter, PFDTV, and DPAD give comparatively good ENL values than the other diffusion and variational methods used for the comparison. However, the ENL metric evaluated for the proposed method is considerably higher for all input images. The NIQE Mittal et al. (2013) is a widely used blind quality evaluator. It based on a natural scene statistical model and a low value of NIQE indicates less distortion due to noise or any other source. As we can infer from the table 5.1, the proposed method is giving a comparatively low value in all the test cases which also indicates the restored data is less noisy.

Other than denoising capability, the details-preserving ability is also evaluated using the metric: Entropy Karathanassi et al. (2007). A high Entropy indicates an increased amount of details present in an image. In case of the proposed method, the tabulated Entropy values are comparatively high which implies that the illumination correction along with restoration is useful to preserve small hidden details. We have used the Global contrast Factor (GCF) Matkovic et al. (2005) for studying the contrast improvement. As we can infer from the Table 5.1, the contrast measure obtained by OBNLM is close to the proposed method for some test cases, but the details present in the image is significantly compromised. However, the proposed method is showing a constant global contrast advancement in all the test cases.

The Contrast Noise Ratio (CNR) Timischl (2015) is similar to Signal to Noise Ratio (SNR), it is used to evaluate quality of restoration. A high CNR value indicates better denoising capability and ensures a contrast preservation. We have evaluated the same on different ROIs and one such result is included in Table 5.1. This tabulated values also support the superior restoration capability of the proposed method.

5.4   Summary of the Chapter

A Non-local TV retinex based restoration algorithm for ultrasound despeckling has been proposed in this Chapter which does the denoising along with contrast enhancement and illumination correction. A fast numerical model based on split-Bregman scheme is followed for providing the solution. The implementation details and other concluding remarks are stated in next chapter.

Figure 5.2 Restoration results of Ultrasound B-mode input (a) noisy input (b)SRAD (c)DPAD (d)OBNLM (e)NLTBV (f)ADMSS (g)PFDTV (h)Eigenfilter (i) Proposed method

(a)　　　　　　　(b)　　　　　　　(c)

(d)　　　　　　　(e)　　　　　　　(f)

(g)　　　　　　　(g)　　　　　　　(h)

Figure 5.3 Restoration results of Ultrasound B-mode input (a) noisy input (b)SRAD (c)DPAD (d)OBNLM (e)NLTBV (f)ADMSS (g)PFDTV (h)Eigenfilter (i) Proposed method
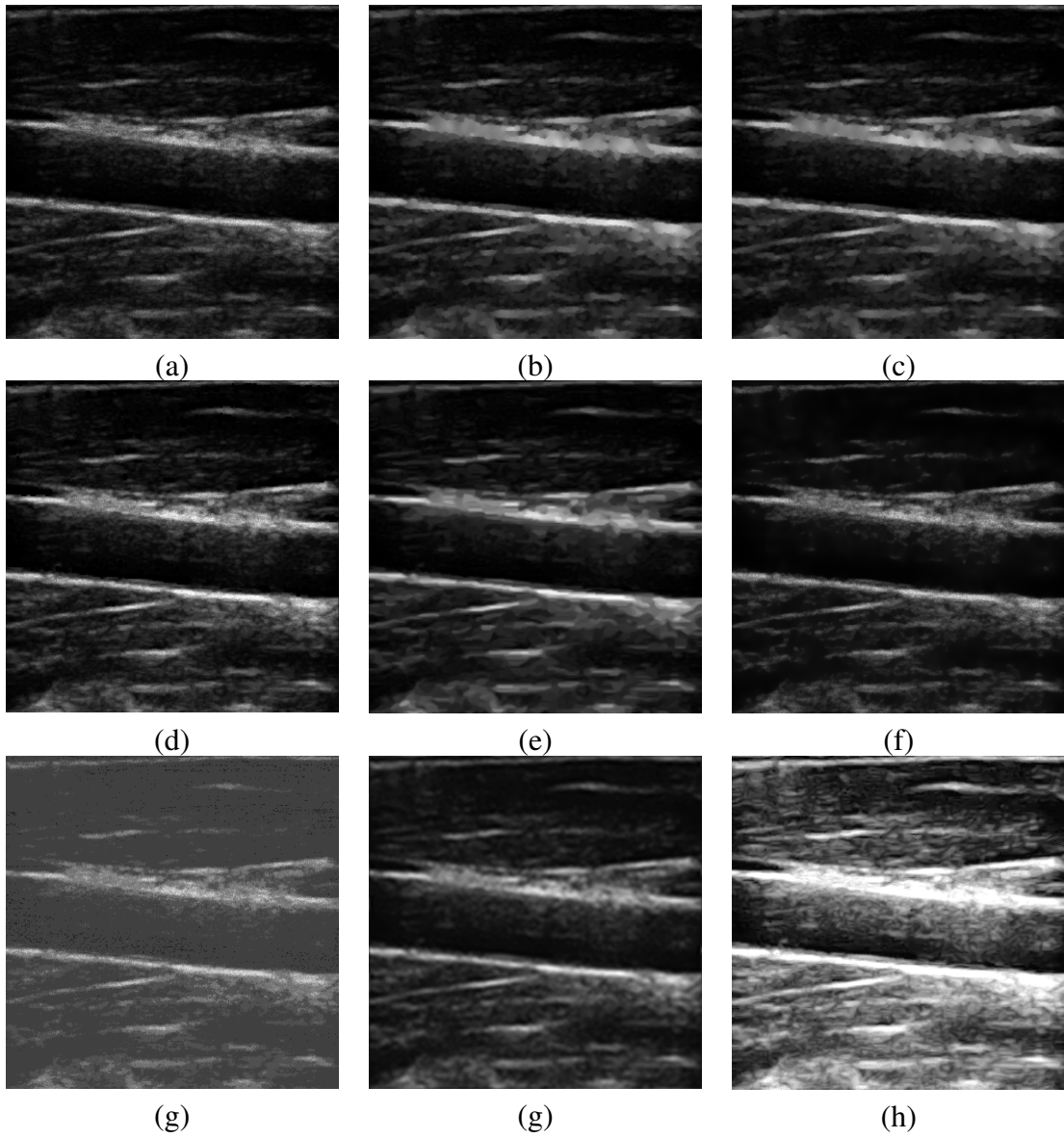
Figure 5.4 Restoration results of Ultrasound B-mode input (a) noisy input (b)SRAD (c)DPAD (d)OBNLM (e)NLTBV (f)ADMSS (g)PFDTV (h)Eigenfilter (i) Proposed method
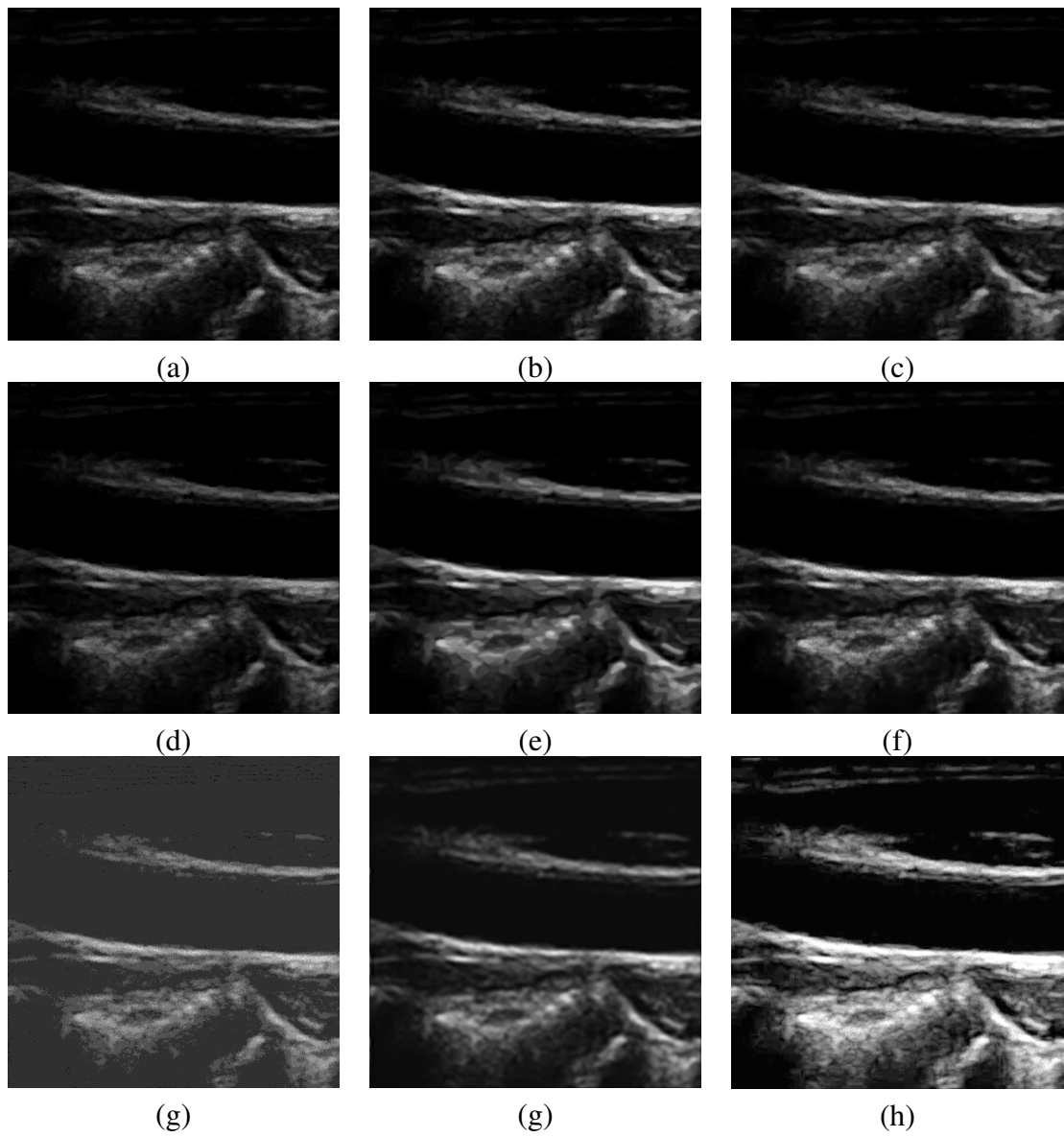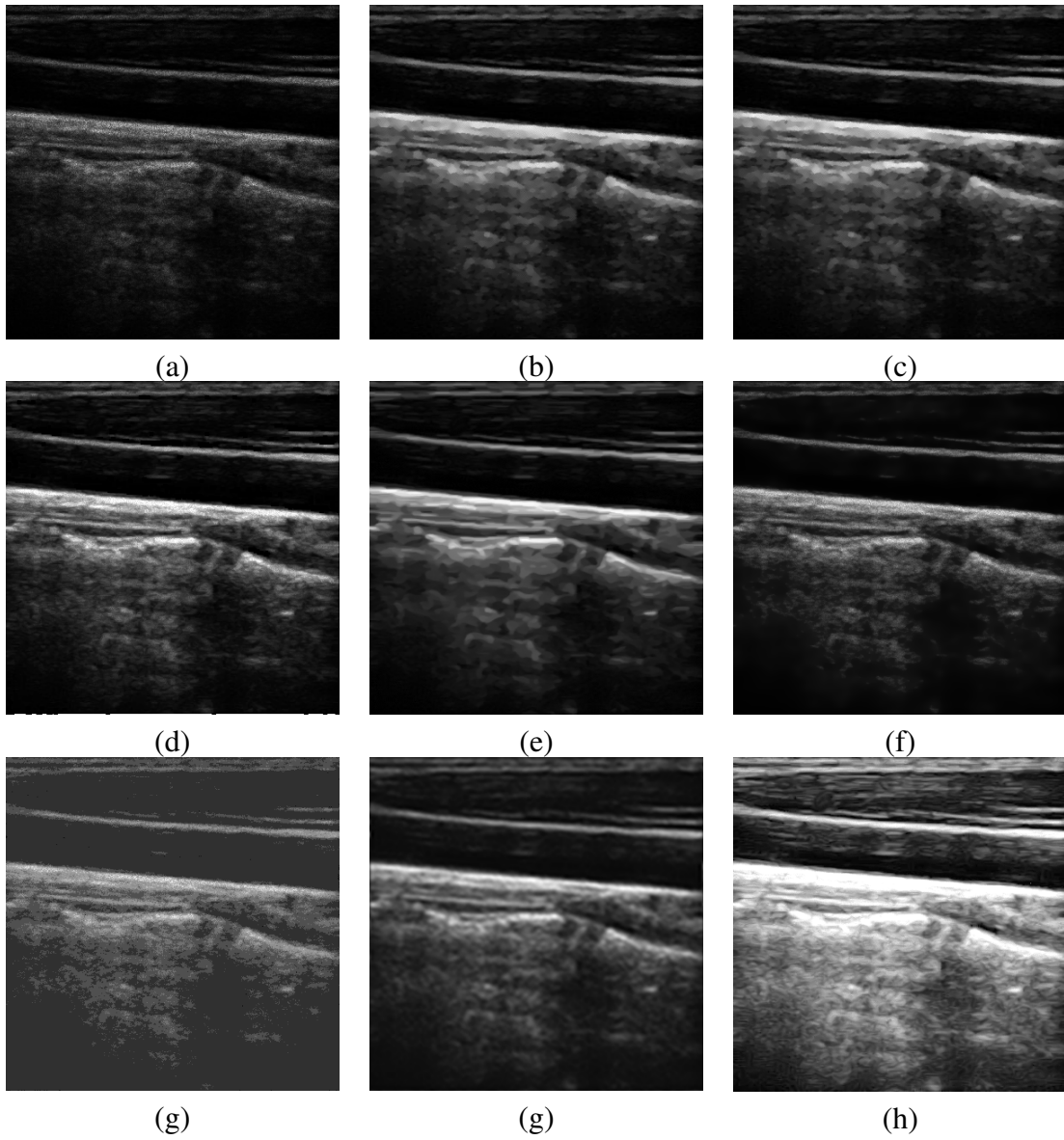
Table 5.1 Comparison on the basis of different Quality metrics

Images	Quality	SRAD	DPAD	OBNLM	NLTBV	ADMSS	PFDTV	Eigen-filter	Proposed
Fig 5.2	Entropy	6.7053	6.7760	6.8013	6.7480	6.3691	1.6262	6.6896	**7.7073**
	GCF	7.6296	7.6375	7.8531	7.6382	6.8447	3.0850	6.1570	**8.2439**
	NIQE	5.0591	4.9484	6.5769	7.2262	6.0977	16.6590	7.3484	**4.0918**
	ENL	48.6909	47.7218	44.1535	31.9273	26.5392	24.3303	63.2070	**413.3297**
	CNR	6.8797	6.8127	6.6179	5.5728	5.0935	2.8834	7.3992	**15.8744**
Fig 5.3	Entropy	6.607	6.6203	6.6901	6.6467	6.2703	1.2658	6.6068	**7.7233**
	GCF	8.0282	7.8897	8.9615	7.8978	6.2703	3.3348	6.5716	**8.9733**
	NIQE	6.9897	6.9727	5.3094	7.3019	8.8407	15.6634	8.0066	**5.2590**
	ENL	22.9210	22.3363	21.3240	17.0062	15.2761	40.2538	22.0371	**268.8701**
	CNR	4.7324	4.6716	4.5630	4.0870	3.8647	4.5501	4.4238	**14.0828**
Fig 5.4	Entropy	5.0950	5.0981	4.4555	5.3408	5.2410	1.5188	5.3604	**5.6627**
	GCF	8.0922	8.1033	7.0739	8.5077	8.3438	3.8821	5.8713	**9.8235**
	NIQE	6.6294	6.6699	8.2822	8.9055	7.3673	15.5489	9.5555	**6.7498**
	ENL	42.7824	42.8157	32.6069	39.6929	40.1287	66.0088	43.2062	**595.0250**
	CNR	6.5194	6.5220	5.6633	6.2646	6.2751	5.5931	6.1064	**22.1321**

(a)　　　　　　　(b)　　　　　　　(c)

(d)　　　　　　　(e)　　　　　　　(f)

(g)　　　　　　　(g)　　　　　　　(h)
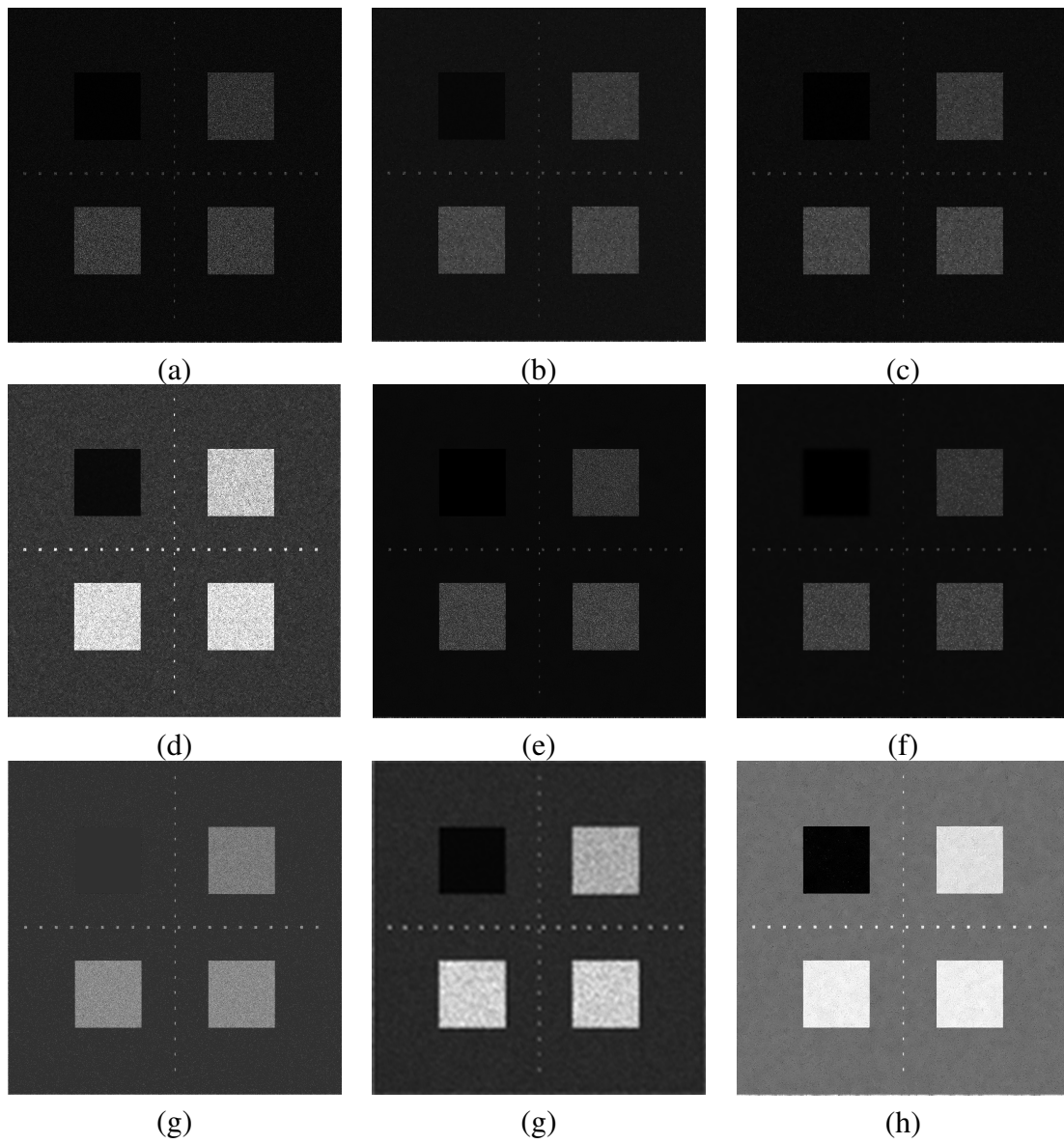
Figure 5.5 Restoration of synthetic noisy data (a) Input image after adding Gamma noise of variance=0.25 (b)SRAD (c)DPAD (d)OBNLM (e)NLTBV (f)ADMSS (g)PFDTV (h)Eigenfilter (i) Proposed method
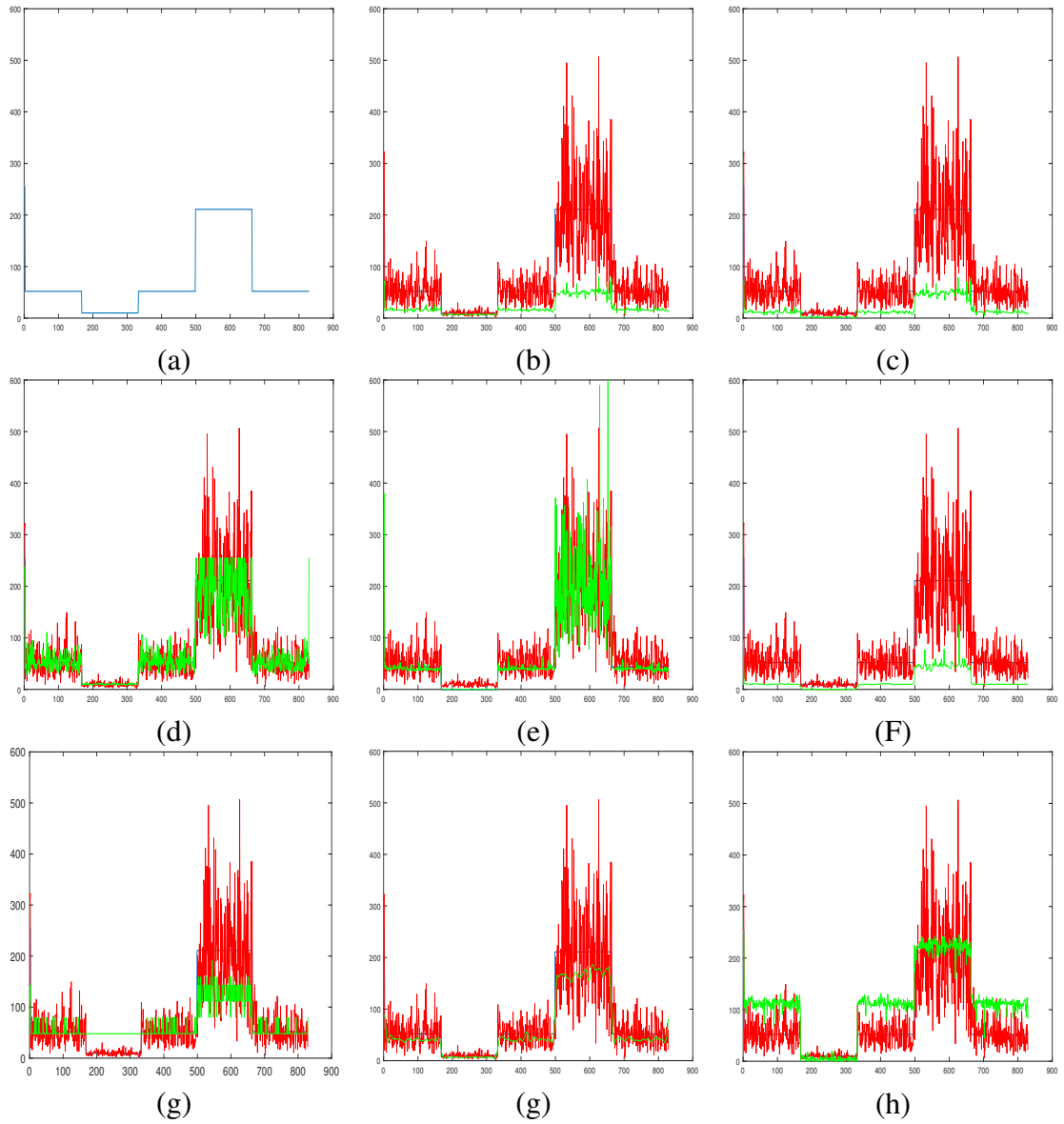
Figure 5.6 Restoration of a 1D signal, sub-figures (b)-(h) contains original signal (Blue), input signal after adding gamma noise of variance=0.25 (Red) and different restored signals (Green): (a) original signal (b)SRAD (c)DPAD (d)OBNLM (e)NLTBV (f)ADMSS (g)PFDTV (h)Eigenfilter (i) Proposed method
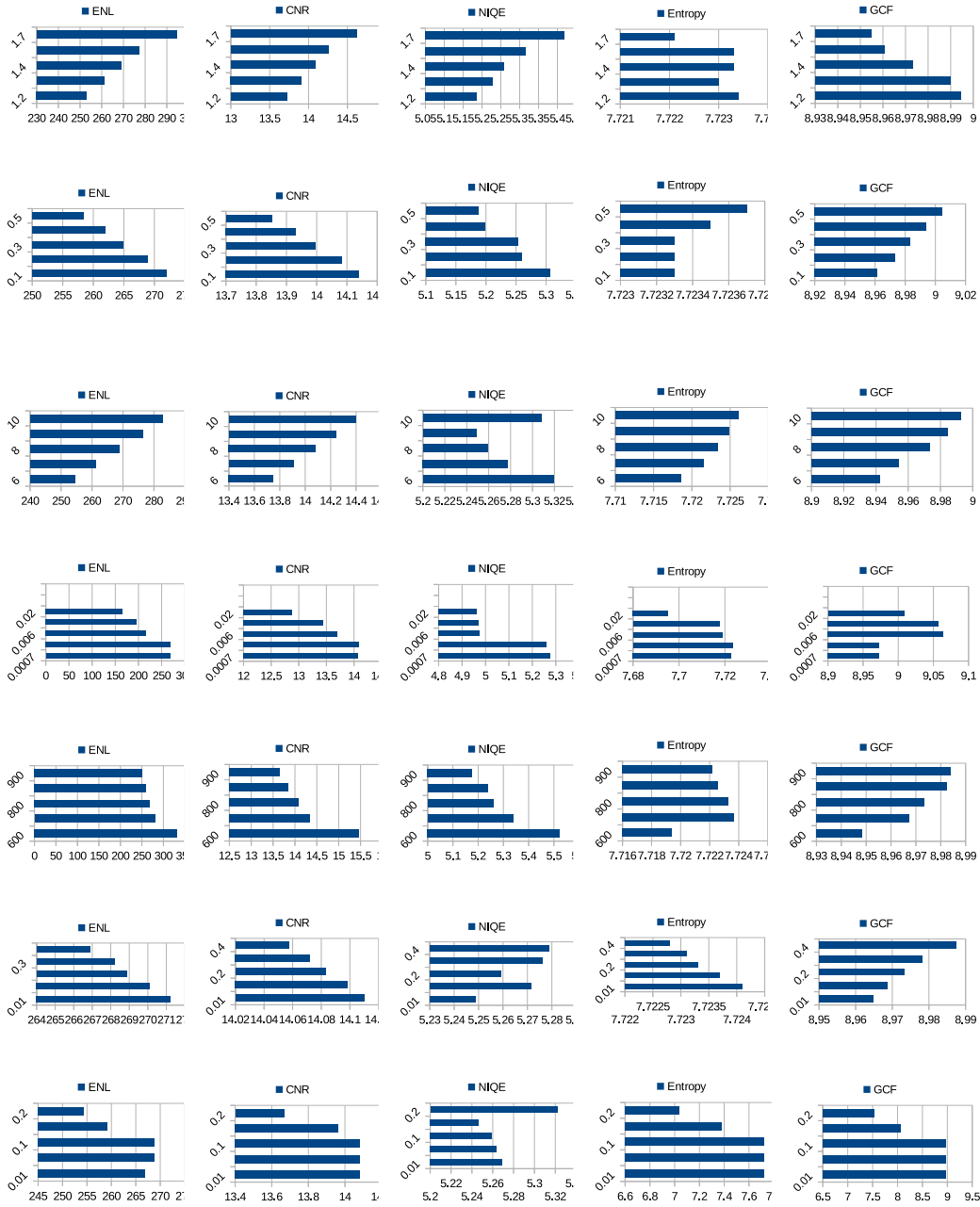
Figure 5.7 Parameter analysis using different quality measures (QM) Row1: Change in QM with respect to λ, Row2: Change in QM with respect to α, Row3: Change in QM with respect to λ_2, Row4: Change in QM with respect to λ_5, Row5: Change in QM with respect to λ_4, Row6: Change in QM with respect to β, Row7: Change in QM with respect to λ_0

96

CHAPTER 6

Conclusion and Future Works

In this thesis three perceptually inspired variational models are proposed (viz. Chapters 3-5) for restoring and enhancing images corrupted by various noise distributions such as Gaussian, Poisson and Gamma. In order to make it as a unified restoration framework, a technique for degradation analysis is also proposed (in Chapter 2). The intensity inhomogeneity being an inevitable hurdle in many satellite and medical image analysis, homogenizing the same is of utmost priority in many applications from these domains. The proposed models are designed based on the retinex theory to handle intensity distortions very effectively. Furthermore, handling noise distortions along with intensity inhomogeneity is a challenging task, as these two complement each other in term of their requirement. This has been effectively addressed by adopting a trade-off between these two processes. Both medical and satellite images are used for testing and verification process. The three contributed models work based on the noise estimation and analysis phase proposed in the second Chapter of this thesis. A detailed analysis is performed to detect the noise characteristics and parameters from the input data. This noise analysis phase serves as a backbone of all the variational models proposed in Chapters 3, 4, and 5. This model automatically analyses the noise distribution from the input data, thereby assists in automatic selection of the appropriate model to handle the relevant distortion.

The variational models in general are useful in defining a framework where the distortions are duly incorporated as constraints in the model and the solution eventually yields the restored version of the image. However, the models converge slowly under a usual explicit numerical solution. Fast numerical approach under the split-Bregman
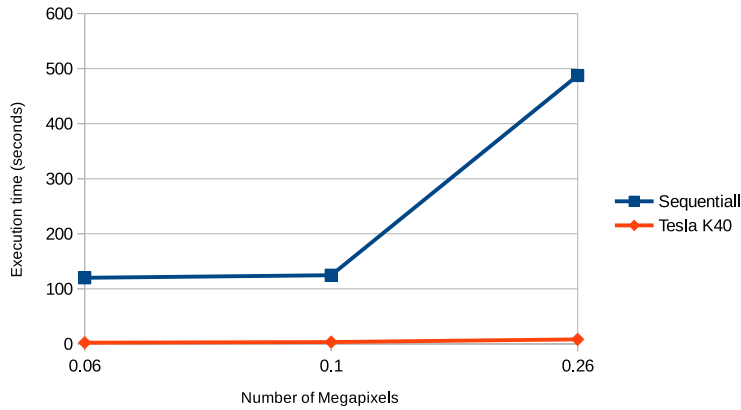
Figure 6.1 Performance comparison of Tesla K40 with Sequential
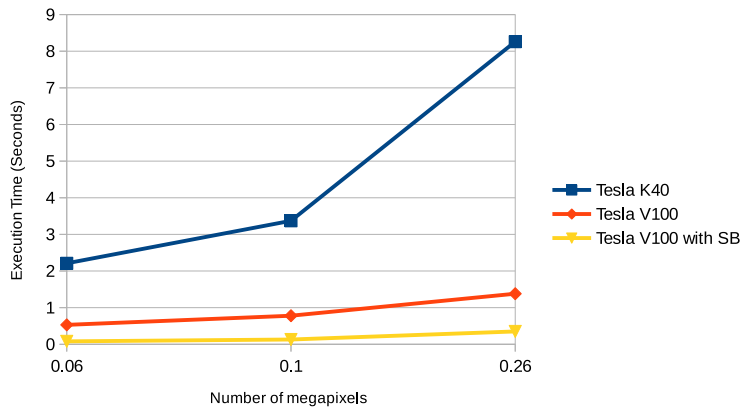
Figure 6.2 Performance comparison of Tesla K40, V100 and V100 with SB

framework helps the model in attaining better convergence rate and it is experimentally verified in Chapters 3-5. Furthermore, the models are implemented by exploiting the parallel computing regime using C++ CUDA, pyCUDA and Open CV library. The parallel computing paradigm improves the overall computational efficiency of the model. For the comparison we have used Nvidia Tesla K40 in Kepler Architecture and V100 in Volta Architecture. The Tesla K40 has 15 Streaming Multiprocessors(SM) with 192 cores per SM, to give a total 2880 CUDA cores. The maximum number of threads per multiprocessor is 2048, and the maximum threads per block are 1024. It has compute ability 3.5 and 12 GB Global memory. Whereas, compute ability of Tesla V100 is 7.0 and it has 5120 CUDA cores with 16 GB memory. The comparison of execution time of NLTV based on the size of the image is given in Fig. 6.1 and Table 6.1. In addition to the conventional Gradient descent optimization, for fast convergence, we have also

Table 6.1 Execution time taken by Sequential and Parallel implementation

Image Size	Sequential	TeslaK40	TeslaV100	Tesla V100 with SB
256×256	120.06	2.21	0.53	0.08
320×320	124.75	3.37	0.78	0.13
512×512	487.48	8.26	1.38	0.36

compared the GPU based NLTV with Split-Bregman (SB), see Figure. 6.2 for details.

From the comparison shown in Table 6.1, one can infer that the Tesla K40 is giving 60 times speedup over the corresponding serial code. From Figure 6.2, we infer that the computational advancement obtained by Tesla V100 is comparatively higher with an average speedup of 356 times. However, the GPU algorithm with split-Bregman optimization has shown a significant advancement that supports the use of this algorithm in real-time restoration tasks. For images of size 512×512 this method is giving an average speedup of 1354 times.

The non-availability of a parallel computing environment sets the model to work under serial computing regime without any user interference. Various medical and satellite images from real-time databases have been adopted for testing and verification process. The models are found to be effective in restoring various images from different imaging modalities. A hardware implementation of the same is still under consideration as a future enhancement. Since the model is efficient in terms of computational aspects, its hardware portability is well substantiated. Moreover, the noise distribution analysis using maximum mean discrepancy (MMD) is also being explored as a future enhancement. MMD being a measure which incorporate higher-order statistical moments, it would be an ideal candidate for performing the feature analysis for the machine learning algorithm designed for the noise analysis phase.

Moreover, there are some deep learning algorithms introduced lately to handle the degradations in images. However, a strong theoretical study regarding the influence of noise characteristics has not been done (Zhang et al., 2017, 2018). Though such deep learning models for some specific kind of noise distortion, they fail to handle different kinds of distortions unlike the proposed models. In addition to that, the accuracy of the deep learning architecture depends on the training data and works for the data on which it is trained and may overlook the others (Linwei Fan and Zhang, 2019). Designing the

deep learning architecture to duly care some of the specific details in images (as this is an inevitable requirement in many imaging modalities) is tedious. Reconstruction and enhancement being an ill-posed inverse problem, the solution under a deep learning framework may not converge to the desired one unlike the regularization frameworks, therefore a unique solution cannot be guaranteed always. However, a detailed theoretical analysis to modify the deep learning architecture (one of the state of the art architectures for various image processing applications) is also being proposed to study as a future work.

The models proposed in chapters 3,4 and 5 are designed for a specific noise distortion. However, they may even work for the other distortions conditionally, but such an analysis has not been performed for the sheer reason that we cannot conclusively prove theoretically that the model designed for a particular distortion works well for the other ones at all conditions. Therefore we refrain from a cross comparative study.

Appendix A

A.1 Statistical metrics

This section details various statistical measures used for quantifying different methods given in the thesis. The evaluation expression and significance are highlighted herein.

A.1.1 Contrast to Noise Ratio (CNR)

Even though Signal to Noise Ratio (SNR) is a very popular measure in image restoration, it ignores the contrast related effects. Therefore, an image degraded due to fog or haze may give a better SNR value despite of being poor in contrast. Consequently, CNR is a widely adopted measure in restoration literature to measure the contrast enhancement ability of a models under consideration. It is evaluated as:

$$CNR = \frac{|\mu_1 - \mu_2|}{\sqrt{\sigma_1^2 + \sigma_2^2}},$$

where μ_1, μ_2, σ_1^2 and σ_2^2 represents the mean intensity and variances of two different regions. Regions are selected so that they have considerable changes in intensity. In this study we have evaluated CNR from multiple regions for getting more reliable results.

A.1.2 Equivalent Number of Looks (ENL)

The ENL is a well known quality metric to evaluate a despeckling algorithms. It is measured for any region of interest (ROI) as:

$$ENL = \frac{\mu_{ROI}^2}{\sigma_{ROI}^2}$$

A better despeckling preserves the mean in the region while reducing the variance, hence a higher value of ENL indicates better denoising, refer Gomez et al. (2017). We have calculated ENL from different homogeneous regions of images, to arrive at the final conclusion regarding quality of restored images.

A.1.3 Naturalness image quality evaluator (NIQE)

The NIQE is a completely "blind quality metric" (the metric that does not require the original image for its calculation). It generates a set of quality aware statistical features from spatial domain (Natural Scene Statistic) NSS model. Then fitting is done on them using a multivariate Gaussian (MVG) model. The same MVG model created from natural images will be compared with the test image fitting, to get the estimate of the quality. As this measure is calculated as a deviation from naturalness of the image, a low value of NIQE indicates better quality, refer Mittal et al. (2013).

A.1.4 Entropy Measure

Entropy is a measure of randomness in data and it can be used to evaluate the information gain. Hence entropy of a contrast degraded image will be very low and the value increases with the enhancement of data. Entropy of an image is calculate as:

$$Entropy(EM) = -\sum_{j=0}^{MAX} P(j)log(P(j)),$$

where *MAX* represents the maximum possible grey value, in case of an 8-bit image it takes the value 255 and $P(j)$ represents the probability of different intensity values.

A.1.5 Global Contrast Factor (GCF)

It is a measure of image contrast and calculated as a weighted average of mean local contrast in different resolutions. Generally,GCF is a more reliable measure as it is not dependent on any region of interest and this measure is closely related to how humans perceive contrast in a scene, refer Matkovic et al. (2005) for more details.

A.1.6 Average Gradient (AG)

It measures the quality of the image and uses it for calculating the spatial resolution in image fusion (Yang et al., 2007). The AG of an image $I(x,y)$ of size $M \times N$ is calculated as below:

$$AG = \frac{1}{NM} \sum_{x=1}^{N} \sum_{y=1}^{M} \sqrt{\left(\left(\frac{\partial I(x,y)}{\partial x} \right)^2 + \left(\frac{\partial I(x,y)}{\partial y} \right)^2 \right)/2}$$

A.1.7 BLind Image Integrity Notator using DCT Statistics (BLIINDS-II)

The BLIINDS-II metric is a no-reference image (blind) quality assessment technique which creates a probabilistic model to give the quality score. In this method four different features related to structure, contrast, etc., are extracted from DCT of image patches in two different scales. A low value of BLIINDS-II indicates better quality of the image (Saad et al., 2010).

A.1.8 Visual Descriptors

The visual descriptors proposed in Hautiere et al. (2008) provides an effective way to evaluate the contrast enhancement achieved in total. This technique is based on the assumption that a good enhancement results in more visible edges and more contrast without saturating the pixels. The descriptors proposed are "rate of new visible edges" (e), contrast measure ($\bar{r}$), and saturation indicator (σ_S). The equations for evaluating e is

$$e = \frac{n_r - n_o}{n_o},$$

where n_r and n_o are the number of visible edges in restored image I and observed image I_0, respectively. If n_s is the number of saturated pixels and $M \times N$ is the size of the image, then the saturation measure is evaluated as:

$$\sigma_s = \frac{n_S}{NM}.$$

The value of $\bar{r}$ is evaluated as geometric mean ratio of visibility levels, see Hautiere et al. (2008) for more details. For a better contrast enhanced image, the value of e and $\bar{r}$ should be high and σ_s should be low.

A.2 Bayesian formulation for various noise distributions

In this section the Bayesian formulation of various functional forms, where the likelihood follows different distributions are provided. The formulations are extracted from various sources and presented for the sake of completeness of the thesis.

A.2.1 Maximum Likelihood Estimate (MLE)

It is a parameter estimation method for data with any probability distribution provided it follows i.i.d. assumption. A normal/Gaussian distribution has PDF

$$P(z|\mu, \sigma) = \frac{1}{\sqrt{2\pi\sigma_0^2}} exp\left(-\frac{1}{2}\frac{(z-\mu)^2}{\sigma^2}\right). \tag{A.2.1}$$

The MLE of the parameters (mean and variance) for any Gaussian distributed data $z(z_1, z_2, ...,_N)$ of size N is as given below:

$$\hat{\mu} = \frac{1}{N}\sum_{j=1}^{N} z_j,$$

$$\sigma^2 = \frac{1}{N}\sum_{j=1}^{N} (z_j - \hat{\mu})^2.$$

Similarly, for the Gamma distribution with PDF

$$P(z|s, \theta) = \frac{z^{s-1}}{\theta^s \Gamma(s)} exp\left(-\frac{z}{\theta}\right), \tag{A.2.2}$$

the parameters shape s and scale θ are

$$\hat{s} = \frac{N\sum_{j=1}^{N} z_j}{N\sum_{j=1}^{N} z_j \ln z_j - \sum_{j=1}^{N} \ln z_j \sum_{j=1}^{N} z_j},$$

and

$$\hat{\theta} = \frac{1}{N^2}\left(N\sum_{j=1}^{N} z_j \ln z_j - \sum_{j=1}^{N} \ln z_j \sum_{j=1}^{N} X_j\right).$$

For Poisson distribution with the PDF

$$P(z|\lambda_p) = \frac{exp(-\lambda_p)\lambda_p^z}{z!}, \tag{A.2.3}$$

the estimate of the parameter λ_p is $\hat{\lambda_p} = \frac{1}{N}\sum_{j=1}^{N} z_j$.

A.2.2 MAP estimator for Gaussian distribution

The Bayesian MAP method is well known in solving ill-posed problems like image restoration. It tries to maximize the posterior probability of the data. According to the Bayes rule,

$$P(X|Y) = \frac{P(Y|X)P(X)}{P(Y)} \tag{A.2.4}$$

where X and Y represent the random variables and $P(X|Y)$ represents the conditional probability i.e probability of X given Y. In the imaging domain, the observed data can be represented as $P(I_0|I)$, where I and I_0 are the original and distorted image respectively. Posterior probability of the desired data $P(I|I_0)$ is then determined by Bayes rule. MAP (Maximum A Posteriori) estimator can be used to get the better approximation of

desired data. This method maximizes $P(I|I_0)$ which takes the form:

$$\max_I \left\{ P(I|I_0) \right\} = \max_I \left\{ (P(I_0|I)) \, P(I) \right\}. \tag{A.2.5}$$

In the above equation $P(I)$ is known as Prior probability and as $P(I_0)$ is a constant as it does not affect the minimization process, therefore it is omitted in calculations. The maximization problem in equation (A.2.5) is equivalent to the minimization of $-log$ likelihood, which takes the form:

$$\min_I \left\{ -\log(P(I|I_0)) \right\} = \min_I \left\{ -\log(P(I_0|I)) - \log(P(I)) \right\}. \tag{A.2.6}$$

Assuming a Gibb's prior $P(I) = e^{(-\frac{\lambda}{2}\phi(I))}$ the minimization problem will be as shown below:

$$\min_I \left\{ -\log(P(I|I_0)) + \frac{\lambda}{2} \, \phi(I) \right\}. \tag{A.2.7}$$

In the above functional $\phi(.)$ denotes regularization prior and $P(I_0|I)$ can be estimated based on noise distribution.

Consider the Gaussian noise with PDF as in equation A.2.1, where maximizing $P(I|I_0)$ amounts to minimizing the negative log-likelihood as in equation A.2.6. For a Gaussian distributed data $p(I_0|I)$ is as follows

$$p(I_0|I) = \frac{1}{2\pi\sigma^2} exp \left(-\frac{(I-I_0)^2}{2\pi\sigma^2} \right). \tag{A.2.8}$$

Assume that the samples of the noise on each pixel $z_j \in \Omega$ (Ω is a discrete image domain) are mutually independent and identically distributed and N is the total number of pixels in image I or I_0 then the likelihood takes the form

$$P(I_0|I) = \prod_{j=1}^{N} P(I_0(z_j)|I(z_j)),$$

which means minimizing $-\log(P(I_0|I))$ amounts to minimizing:

$$\min_I \left\{ \sum_{j=1}^{N} - \left(\left(\frac{(I(z_j)-I_0(z_j))^2}{2\pi\sigma^2} \right) + \lambda\phi(I(z_j)) \right) \right\}. \tag{A.2.9}$$

For simplicity drop the index z_j and constant terms in the minimization functional, then we have

$$\min_I \left\{ -\sum \left((I-I_0)^2 + \lambda\phi(I) \right) \right\}, \tag{A.2.10}$$

Now the optimization problem in case of a Gaussian distributed noise gives the above expression and the corresponding fidelity is $(I-I_0)^2$, refer Rudin et al. (1992) for more details. The term $\phi(.)$ denotes the regularization prior and we can assume a non-local total variation regularization prior in place of $\phi(I)$.

A.2.3 MAP estimator for Poisson distribution

The Probability Density Function(PDF) of Poisson distribution is given in equation A.2.3, where λ_p is both mean and standard deviation. As stated before, our goal is to maximize the probability of the random variable I (the original image) given the observed noisy image I_0 which eventually leads to the minimization as in equation A.2.6. As the noise follow Poisson distribution, the corresponding likelihood probability is given below:

$$P(I_0|I) = P_I(I_0) = \frac{e^{-I}I^{I_0}}{I_0!}, \tag{A.2.11}$$

Considering the image (I and I_0) as a set of independent pixels x_j and following similar steps as in the previous section the -log likelihood of the Poisson noisy data is

$$\min_I \left\{ \sum_{j=1}^N I(z_j) - I_0(z_j)\log I(z_j) - \sum_{j=1}^N \log(P(I(z_i))) \right\}. \tag{A.2.12}$$

Assuming Gibbs prior as before the above equation becomes

$$\min_I \left\{ I - I_0 \log I + \frac{\lambda}{2}\phi(I) \right\}, \tag{A.2.13}$$

where $(I - I_0 \log I)$ represents the fidelity term. Explanation regarding the same is given in Kayyar and Jidesh (2018).

A.2.4 MAP estimator for Gamma distribution

The MAP estimator for Gamma distributed noise is derived in Aubert and Aujol (2008) and some highlights of the same is provided here. The PDF of Gamma distribution is given in equation A.2.2. Assuming the speckle noise to follow Gamma law $P(I_0|I)$ is as below

$$P(I_0|I) = \frac{L^L}{I^L \Gamma(L)} I_0^{L-1} e^{(-LI_0)/I}, \tag{A.2.14}$$

where L stands for the number of looks and in normal single image operation it takes the value one. As stated before, MAP estimator works by maximizing $P(I|I_0)$ which implies to minimizing the negative log-likelihood. Minimizing $-log(P(I_0|I))$ takes the following form:

$$\min_I \left\{ \sum_{j=1}^N \left(\left(L(\ln I(z_j) + \frac{I_0(z_j)}{I(z_j)}) \right) + \lambda\phi(I(z_j)) \right) \right\}. \tag{A.2.15}$$

For simplicity if we eliminate z_j and assume $L = 1$ then the minimization problem will be as given below:

$$\min_I \left\{ \left(\ln I + \frac{I_0}{I} \right) + \frac{\lambda}{2} \phi(I) \right\}, \tag{A.2.16}$$

where the noise fidelity term derived is $\left(\ln I + \frac{I_0}{I} \right)$.

BIBLIOGRAPHY

Aja-Fernandez, S. and Alberola-Lopez, C. (2002). On the estimation of the coefficient of variation for anisotropic diffusion speckle filtering. *IEEE Transactions on Image Processing*, 11(11):1260–1270.

Antoni Buades, B. C. and Morel, J.-M. (2005). A non-local algorithm for image denoising. In *2005 IEEE Computer Society Conference on Computer Vision and Pattern Recognition (CVPR'05)*, volume 2, pages 60–65. IEEE.

Arici, T., Dikbas, S., and Altunbasak, Y. (2009). A histogram modification frame-work and its application for image contrast enhancement. *IEEE Trans. Image Process.*, 18(9):1921–1935.

Aubert, G. and Aujol, J.-F. (2008). A variational approach to removing multiplicative noise. *SIAM journal on applied mathematics*, 68(4):925–946.

Aubert, G. and Kornprobst, P. (2006). *Mathematical problems in image processing: Partial Differential Equations and the Calculus of Variations*, volume 147. Springer, Berlin.

Azzam, M. and Awad, A. (1996). Entropy measures and some distribution approximations. *Microelectron.Reliab.*, 36(10):1569–1580.

Beaurepaire, L., Chehdi, K., and Vozel, B. (1997). Identification of the nature of noise and estimation of its statistical parameters by analysis of local histograms. In *1997 IEEE International Conference on Acoustics, Speech and Signal Processing*, pages 841–844. IEEE.

Bertalmio, M., Caselles, V., and Provenzi, E. (2009). Issues about retinex theory and contrast enhancement. *Int. J. Comput. Vis.*, 83(1):101–119.

Bini, A. A. and Bhat, M. S. (2014). Despeckling low SNR, low contrast ultrasound images via anisotropic level set diffusion. *Multidimensional Systems and Signal Processing*, 25(1):41–65.

Buades, A., Coll, B., and Morel, J. (2005). A non-local algorithm for image denoising. In *2005 IEEE Computer Society Conference on Computer Vision and Pattern Recognition (CVPR'05)*, volume 2, pages 1–6.

Chambolle, A. and Pock, T. (2010). A first-order primal-dual algorithm for convex problems with applications to imaging. *Journal of Mathematical Imaging and Vision*, 40(1):120–145.

Chan, S., Khoshabeh, R., Gibson, K. B., et al. (2011). An augmented Lagrangian method for total variation video restoration. *IEEE Transactions on Image Processing*, 20(11):3097–3111.

Chang, H., Ng, M. K., Wang, W., and Zeng, T. (2015). Retinex image enhancement via a learned dictionary. *Optical Engineering*, 54:013107.

Chehdi, K. and Sabri, M. (1992). A new approach to identify the nature of the noise affecting an image. In *50th Midwest Symposium on Circuits and Systems (MWSCAS)*, pages 285–288. IEEE.

Chen, Y. and Das, M. (2007). An automated technique for image noise identification using a simple pattern classification approach. In *50th Midwest Symposium on Circuits and Systems (MWSCAS)*, pages 819–822.

Cortes, C., V. V. (1995). Support-vector networks. *Mach Learn*, 20(1):273–297.

Coupe, P., Hellier, P., et al. (2009). Nonlocal means-based speckle filtering for ultrasound images. *IEEE Transactions on Image Processing*, 18(10):2221–2229.

Damerjiana, V., Tankyevych, O., Souag, N., and Petita, E. (2014). Speckle characterization methods in ultrasound images- A review. *IRBM*, 35(4):202–213.

Demirel, H., Anbarjafari, G., and Jahromi, M. N. S. (2008). Image equalization based on singular value decomposition. In *Proc. IEEE 23rd ISCIS*, pages 1–5. IEEE.

Demirel, H., Ozcinar, C., and Anbarjafari, G. (2010). Satellite image contrast enhancement using discrete wavelet transform and singular value decomposition. *IEEE Geosci. Remote Sens. Lett.*, 7(2):333–337.

Doric, D., Nikotic-Doric, E., Jevremovic, V., and Malisic, J. (2009). On measuring skewness and kurtosis. *Quality and Quantity*, 43(3):481–493.

Duan, K.-B. and Keerthi, S. (2005). *Which Is the Best Multiclass SVM Method? An Empirical Study*, volume 3541. Springer.

Ekstrom, M. P. (1982). Realizable wiener filtering in two-dimensions. *IEEE Trans. Acoust. Speech Signal Processing*, ASSP-30:31–40.

Ferradans, S., Palma-Amestoy, R., and Provenzi, E. (2015). An algorithmic analysis of variational models for perceptual local contrast enhancement. *Image Processing On Line*, 5:219–233.

Frost, V., Stiles, J., Shanmugan, K., et al. (1982). A model for radar images and its application to adaptive digital filtering of multiplicative noise. *IEEE Trans. Pattern Anal. Mach. Intell.*, PAMI-2:157–65.

Fu, X., Sun, Y., LiWang, M., et al. (2014). A novel retinex based approach for image enhancement with illumination adjustment. In *IEEE International Conference on Acoustics, Speech and Signal Processing (ICASSP)*, pages 1190–1194. IEEE.

Fu, X., Wang, J., Zeng, D., Huang, Y., and Ding, X. (2015). Remote sensing image enhancement using regularized-histogram equalization and dct. *IEEE Geoscience and Remote Sensing Letters*, 12(11):2301–2305.

Fuglede, B. and Topsoe, F. (2004). Jensen-shannon divergence and hilbert space embedding. page 31.

Fuyu, T., Xiaomin, Y., Wei, W., et al. (2018). Retinex-based image enhancement framework by using region covariance filter. *Soft Computing*, 22(5):1399–1420.

Gilboa, G. and Osher, S. (2008). Nonlocal operators with applications to image processing. *Multiscale Modeling & Simulation*, 7(3):1005–1028.

Goldstein, T., Bresson, X., and Osher, S. (2010). Geometric applications of the split bregman method: Segmentation and surface reconstruction. *IEEE Geoscience and Remote Sensing Letters*, 45(1):272–293.

Gomez, L., Ospina, R., and Frery, A. C. (2017). Unassisted quantitative evaluation of despeckling filters. *Remote Sensing*, 9(4).

Hadamard, J. and Morse, P. M. (1953). *Lectures on Cauchy's problem in linear partial differential equations*, volume 6. Dover Publications, New York.

Hautiere, N., Tarel, J.-P., Aubert, D., et al. (2008). Blind contrast enhancement assessment by gradient ratioing at visible edgese. *Image Analysis & Stereology Journal*, 27(2):87–95.

Hogg, R. V. and Craig, A. T. (1970). *Introduction to Mathematical Statistics: 3d Ed*. Macmillan.

Holla, S. and Jidesh, P. (2018). Non-local total variation regularization models for image restoration. *Computers and Electrical Engineering*, 67(1):114–133.

Huang, L. L., Xiao, L., and Wei, Z. H. (2010). Multiplicative noise removal via a novel variational model. *Journal on Image and Video Processing*, pages 1–16.

Huang, S., Cheng, F., and Chiu, Y. (2013). Efficient contrast enhancement using adaptive gamma correction with weighting distribution. *IEEE Transactions on Image Processing*, 22(3):1032–1041.

Huifang Li, L. Z. and Shen, H. (2012). Perceptually inspired variational method for the uneven intensity correction of remote sensing images. *IEEE Transactions on Geosci. and Remote Sens.*, 50(8):3053–3065.

Ibrahim, H. and Kong, N. S. P. (2007). Brightness preserving dynamic histogram equalization for image contrast enhancement. *IEEE Trans. Consum. Electron.*, 53(4):1752–1758.

Jang, J. H., Kim, S. D., and Ra, J. B. (2011). Enhancement of optical remote sensing images by subband-decomposed multiscale retinex with hybrid intensity transfer function. *IEEE Geosci. Remote Sens. Lett.*, 8(5):983–987.

Jean-Luc Starck, Candes, E. J., and Donoho, D. L. (2002). The curvelet transform for image denoising. *IEEE Transactions on Image Processing*, 11(6):670–684.

Jidesh, P. (2014). A convex regularization model for image restoration. *Computers and Electrical Engineering*, 40(8):66–78.

Jidesh, P. and Balaji, B. (2018). Image despeckling with non-local total bounded variation regularization. *Computers and Electrical Engineering*, 70(1):631–646.

Jidesh, P. and Bini, A. A. (2017). Image despeckling and deblurring via regularized complex diffusion. *Signal, Image and Video Processing*, 11:977–984.

Jidesh, P. and Febin, I. P. (2019). Estimation of noise using non-local regularization frameworks for image denoising and analysis. *Arab. J. Sci. Eng.*, 44(4):3425–3437.

Jidesh, P. and Holla, S. (2018). Non-local total bounded variation scheme for multiple-coil magnetic resonance image restoration. *Multidimensional Systems and Signal Processing*, 29(4):1427–1448.

Jobson, D. J., Rahman, Z., and Woodell, G. A. (1997). A multiscale retinex for bridging the gap between color images and the human observation of scenes. *IEEE Trans. Image Process.*, 6(7):965–976.

Karathanassi, V., Kolokousis, P., and Ioannidou, S. (2007). A comparison study on fusion methods using evaluation indicators. *Int. J. Remote Sens.*, 28:2309–2341.

Kayyar, S. H. and Jidesh, P. (2018). Non-local total variation regularization approach for image restoration under a poisson degradation. *Journal of Modern Optics*, 65(19):2231–2242.

Kimmel, R., Elad, M., Shaked, D., et al. (2003). A variational framework for retinex. *International Journal of Computer Vision*, 52:7–23.

Krissian, K., Westin, C. F., et al. (2007). Oriented speckle reducing anisotropic diffusion. *IEEE Transactions on Image Processing*, 16(5):1412–1424.

Kuan, D. T., Sawchuk, A. A., Strand, T. C., and Chavel, P. (1985). Adaptive noise smoothing filter for images with signal-dependent noise. *Pattern Anal Mach Intell. IEEE Trans.*, 2:165–77.

Kullback, S. and Leibler, R. (1952). On information and sufficiency. *Annals of Mathematical Statistics*, 22(1):79–86.

Kwak, H.-J. and Park, G.-T. (2014). Image contrast enhancement for intelligent surveillance systems using multi-local histogram transformation. *J. Intell. Manuf.*, 25(2):303–318.

Lam, D., Kuzma, R., McGee, K., et al. (2018). xview: Objects in context in overhead imagery. *CoRR*.

Lan, X., Shen, H., Zhang, L., and Yuan, Q. (2014). A spatially adaptive retinex variational model for the uneven intensity correction of remote sensing images. *Signal Processing*, 101:19–34.

Land, E. H. (1977). The retinex theory of color vision. *Sci. Amer.*, 237(6):108–128.

Land, E. H. (1983). Recent advances in the retinex theory and some implications for cortical computations: Color vision and natural image. *Proc. Natl. Acad. Sci. USA*, 80(16):5163–5169.

Land, E. H. and McCann, J. J. (1971). Lightness and retinex theory. *J. Opt. Soc. Am.*, 61(1):1–11.

Le, T., Chartrand, R., and Asaki, T. J. (2007). A variational approach to reconstructing images corrupted by Poisson noise. *Journal of Mathematical Imaging and Vision*, 27:257–263.

Lee, E., Kim, S., Kang, W., et al. (2013). Contrast enhancement using dominant brightness level analysis and adaptive intensity transformation for remote sensing images. *IEEE Geosci. Remote Sens. Lett.*, 10(1):62–66.

Lee, J.-S. (1980). Digital image enhancement and noise filtering by use of local statistics. *Pattern Anal Mach Intell IEEE Trans*, 2:165–8.

Lee, S.-H. and Seo, J. K. (2005). Noise removal with gauss curvature-driven diffusion. *IEEE Transactions on Image Processing*, 14(7):904–909.

Li, D., Zhang, Y., and P. Wen, L. B. (2015). A retinex algorithm for image enhancement based on recursive bilateral filtering. In *11th International Conference on Computational Intelligence and Security (CIS)*, pages 154–157.

Li, M., Liu, J., Yang, W., Sun, X., and Guo, Z. (2018). Structure-revealing low-light image enhancement via robust retinex model. *IEEE Transactions on Image Processing*, 27(6):2828–2841.

Li, S., Yang, Z., and Li, H. (2017). Statistical evaluation of no-reference image quality assessment metrics for remote sensing images. *ISPRS International Journal of Geo-Information*, 6(5):133.

Li, Y., Gong, H., Feng, D., and Zhang, Y. (2011). An adaptive method of speckle reduction and feature enhancement for sar images based on curvelet transform and particle swarm optimization. *IEEE Transactions on Geoscience and Remote Sensing*, 49(8):3105–3116.

Linwei Fan, Fan Zhang, H. F. and Zhang, C. (2019). Brief review of image denoising techniques. *Visual Computing for Industry, Biomedicine, and Art*, 2(1):7.

Liu, C., Freeman, W., Szeliski, R., et al. (2006). Noise estimation from a single image. In *2006 IEEE Computer Society Conference on Computer Vision and Pattern Recognition (CVPR'06)*, pages 901–908. IEEE.

Liu, H., Zhang, Z., Xiao, L., et al. (2017a). Poisson noise removal based on nonlocal total variation with euler's elastica pre-processing. *Journal of Shanghai Jiaotong University (Science)*, 22(5):609–614.

Liu, J., Zhou, C., Chen, P., et al. (2017b). An efficient contrast enhancement method for remote sensing images. *IEEE Geosci. Remote Sens. Lett.*, 14(10).

Liu, L., Pang, Z. F., and Duan, Y. (2017c). A novel variational model for retinex in presence of severe noises. In *IEEE International Conference on Image Processing (ICIP)*, pages 3490–3494. IEEE.

Liu, X. and Huang, L. (2010). Split bregman iteration algorithm for total bounded variation regularization based image deblurring. *Journal of Mathematical Analysis and Applications*, 372:486–495.

Liu, X. and Huang, L. (2014). A new nonlocal total variation regularization algorithm for image denoising. *Mathematics and Computers in Simulation*, 97:224–233.

Liu, X., Tanaka, M., and Okutomi, M. (2013). Single-image noise level estimation for blind denoising. *IEEE Trans Image Process.*, 22(12):1260–1270.

Liu, X., Tanaka, M., and Okutomi, M. (2014). Practical signal-dependent noise parameter. *IEEE Trans Image Process.*, 23(10):4361–4371.

Lu, X., Wang, Y., and Yuan, Y. (2013). Graph-regularized low-rank representation for destriping of hyperspectral images. *IEEE Transactions on Geoscience and Remote sensing*, 51(7):4009–4018.

Lu, X., Yuan, Y., and Yan, P. (2014). Alternatively constrained dictionary learning for image superresolution. *IEEE Transactions on Cybernetics.*, 44(3):366–377.

Luisier, F., Blu, T., and Unser, M. (2011). Image denoising in mixed poisson-gaussian noise. *IEEE Trans. Image Process.*, 20(3):696–708.

Ma, W. and Osher, S. (2012). A tv bregman iterative model of retinex theory. *Inverse Problems and Imaging*, 6(4):697–708.

Marquina, A. and Osher, S. (2000). Explicit algorithms for a new time dependent model based on level set motion for nonlinear deblurring and noise removal. *SIAM Journal on Scientific Computing*, 22(2):387–405.

Matkovic, K., Neumann, L., Neumann, A., and Psik, T. (2005). Global contrast factor - a new approach to image contrast. In *in Proc. Comput. Aesthetics*, pages 159–168.

Mei, K., Hu, B., Fei, B., and Qin, B. (2020). Phase asymmetry ultrasound despeckling with fractional anisotropic diffusion and total variation. *IEEE Transactions on Image Processing*, 29:2845–2859.

Menendez, M., Pardo, J., et al. (1991). Divergence measures based on the shannon entropy. *IEEE Transactions on Information theory*, 37(1):145–151.

Menendez, M., Pardo, J., et al. (1997). The jensen-shannon divergence. *Journal of the Franklin Institute*, 334(2):307–318.

Michailovich, O. V. and Tannenbaum, A. (2006). Despeckling of medical ultrasound images. *IEEE Transactions on Ultrasonics, Ferroelectrics, and Frequency Control*, 53(1):64–78.

Mittal, A., Soundararajan, R., and Bovik, A. C. (2013). Making a 'completely blind' image quality analyzer. *ISPRS International Journal of Geo-Information*, 20(3):209–212.

Mnih, V. (2013). Machine learning for aerial image labeling. *Ph.D. dissertation, University of Toronto*.

Mohamed, S. T., Ebeid, H. M., Hassanien, A. E., et al. (2017). A hybrid flower pollination optimization based modified multi-scale retinex for blood cell microscopic image enhancement. In *2017 Third International Conference on Research in Computational Intelligence and Communication Networks (ICRCICN)*, pages 225–230. IEEE.

Moreira, A., Prats-Iraola, P., Younis, M., et al. (2013). A tutorial on synthetic aperture radar. *IEEE Geoscience and Remote Sensing Magazine*, 1:6–43.

Nagare, M. B., Patil, B. D., and Holambe, R. S. (2017). A multi directional perfect reconstruction filter bank designed with 2-d eigenfilter approach: Application to ultrasound speckle reduction. *J Med Syst.*, 41(2).

Ng, M. K. and Wang, W. (2011). A total variation model for retinex. *SIAM Journal on Imaging Sciences*, 4(1):345–365.

Nnolim, U. and Lee, P. (2008). Homomorphic filtering of colour images using a spatial filter kernel in the HSI colour space. In *IEEE Int. Instrum. Meas. Technol. Conf.*, pages 1738–1743.

Parolai, S. (2009). Denoising of Seismograms Using the S Transform. *Bulletin of the Seismological Society of America*, 99(1):226–234.

Patil, P. D. and Kumbhar, A. D. (2015). Bilateral filter for image denoising. In *Proc. Green Computing and Internet of Things (ICGCIoT) 2015 International Conference*, pages 299–302.

Perona, P. and Malik, J. (1990). Scale-space and edge detection using anisotropic diffusion. *IEEE Transactions on Pattern Analysis and Machine Intelligence*, 12(7):629–639.

Ramos-Llorden, G., anchez Ferrero, G. V.-S., Martin-Fernandez, M., et al. (2015). Anisotropic diffusion filter with memory based on speckle statistics for ultrasound images. *IEEE Transactions on Image Processing*, 24(1):345–358.

Rasti, B., Scheunders, P., Ghamisi, P., et al. (2018). Noise reduction in hyperspectral imagery: Overview and application. *Remote Sens.*, 10(3):482.

Rudin, L., Osher, S., and Fatemi, E. (1992). Nonlinear total variation based noise removal algorithms. *Physica D: Nonlinear Phenomena*, 60(1):259–268.

Saad, M., Bovik, A., and Charrier, C. (2010). A dct statistics-based blind image quality index. *IEEE Signal Process. Lett.*, 17:583–586.

Schowengerdt, R. A. (2007). *Remote sensing: models and methods for image processing*, volume 2. Academic Press, New York.

Setty, S., Srinath, N. K., and Hanumantharaju, M. C. (2016). Split and merge multiscale retinex enhancement of magnetic resonance medical images. *Information Systems Design and Intelligent Applications*, 435:519–529.

Shen, J. (2003). On the foundations of vision modeling I. weber's law and weberized tv restoration. *Physica D*, 175:241–251.

Shui, P. L. and Zhang, Z. J. (2014). Fast sar image segmentation via merging cost with relative common boundary length penalty. *IEEE Transactions on Geoscience and Remote Sensing*, 52(10):6434–6448.

Simoncelli, E. P. and Adelson, E. H. (1996). Noise removal via bayesian wavelet coring. In *Proc. 3 rd International Conference on Image Processing*, pages 379–382. IEEE.

Sokolova, M. and Lapalme, G. (2009). A systematic analysis of performance measures for classification tasks. *Information Processing and Management*, 45(4):427–437.

Tikhonov, A. N. and Arsenin, V. Y. (1977). *Solutions of ill-posed problems*. V. H. Winston & Sons, Washington, D.C.: John Wiley & Sons, New York-Toronto, London.

Timischl, F. (2015). The contrast-to-noise ratio for image quality evaluation in scanning electron microscopy. *Scanning*, 37:54–62.

Vozel, B., Chehdi, K., Klaine, L., et al. (2006). Noise identification and estimation of its statistical parameters by using unsupervised variational classification. In *2006 IEEE International Conference on Acoustics, Speech and Signal Processing*, pages 2805–2808. IEEE.

Wang, L., Xiao, L., Liu, H., and Wei, Z. (2014). Variational bayesian method for retinex. *IEEE Transactions on Image Processing*, 23(8):3381–3395.

Wang, W. and He, C. (2017). A fast and effective method for a poisson denoising model with total variation. *IEEE Signal Process. Lett.*, 24(3):269–273.

Xiao, L., Huang, L.-L., and Wei, Z.-H. (2010). A weberized total variation regularization-based image multiplicative noise removal algorithm. *EURASIP J Adv SignalProcess.*, pages 1–15.

Xizhi, Z. (2008). The application of wavelet transform in digital image processing. In *2008 International Conference on MultiMedia and Information Technology*, pages 326–329.

Yang, X., Jing, Z., Liu, G., et al. (2007). Fusion of multi-spectral and panchromatic images using fuzzy rule. *Commun. Nonlinear Sci. Numer. Simul.*, 12:1334–1350.

Yu, Y. and Acton, S. (2002). Speckle reducing anisotropic diffusion. *IEEE Transactions on Image Processing*, 11(11):1260–1270.

Zamperoni, P. (2013). *Image Enhancement*, volume 1. Academic Press, New York.

Zhang, B. and Allebach, J. P. (2008). Adaptive bilateral filter for sharpness enhancement and noise removal. *IEEE Trans. ImageProcess.*, 17(5):664–678.

Zhang, G., Chen, Q., and Sun, Q. (2014). Illumination normalization among multiple remote-sensing images. *IEEE Geosci. Remote Sens. Lett.*, 11(9):1470–1474.

Zhang, K., Zuo, W., Chen, Y., Meng, D., and Zhang, L. (2017). Beyond a gaussian denoiser: Residual learning of deep cnn for image denoising. *IEEE Transactions on Image Processing*, 26(7):3142–3155.

Zhang, K., Zuo, W., and Zhang, L. (2018). Ffdnet: Toward a fast and flexible solution for cnn-based image denoising. *IEEE Transactions on Image Processing*, 27(9):4608–4622.

Zhang, S., jin Tang, G., hua Liu, X., et al. (2018). Retinex based low-light image enhancement using guided filtering and variational framework. *Optoelectronics Letters*, 14(2):156–160.

Zhang, S., Wang, T., Dong, J., and Yu, H. (2017). Underwater image enhancement via extended multi-scale retinex. *Neurocomputing*, 245:1–9.

Zhu, F., Wang, Y., Xiang, S., et al. (2014). Structured sparse method for hyperspectral unmixing. *ISPRS Journal of Photogrammetry and Remote Sensing*, 88:101–118.

Zosso, D., Tran, G., and Osher, S. (2015). Non-local retinex-a unifying framework and beyond. *SIAM Journal on Imaging Sciences*, 8:787–826.

PUBLICATIONS

Journal publication

1. P.Jidesh and I.P. Febin, A Perceptually Inspired Variational Model for Enhancing and Restoring Remote Sensing Images, IEEE Geoscience and Remote Sensing Letters, doi: 10.1109/LGRS.2020.2969411, 2020

2. I.P. Febin, P. Jidesh, A Retinex-Based Variational Model for Enhancement and Restoration of Low-Contrast Remote-Sensed Images Corrupted by Shot Noise, IEEE Journal of Selected Topics in Applied Earth Observations and Remote Sensing, vol. 13, pp. 941-949, doi: 10.1109/JSTARS.2020.2975044, 2020

3. P. Jidesh and I.P. Febin, Estimation of noise using non-local regularization frameworks for image denoising and analysis, AJSE (Springer), 44, pp. 3425-3437, DOI: http://dx.doi.org/10.1007/s13369-018-3542-2., 2019

4. I.P. Febin, P. Jidesh, Noise classification and automatic restoration system using Non-local regularization frameworks, J. Imaging Sciences (Taylor & Francis), Vol. 66, No. 8, pp. 479-491, 2018

BIODATA

Name   :   FEBIN I.P .

Email   :   febimolu@gmail.com

Date of Birth   : 01st May 1988.

Permanent address :   Febin I. P.,

                              Iyyath House,

                              Vadacode P O,

                              Karippassery mugal,

                              Kalamassery, Kerala, Pin:682021

Educational Qualifications :

Degree	Year	Institution / University
B.Tech	2010	Rajagiri School of Engineering & Technology, Kakkanad.
Information Technology		Mahatma Gandhi University
M.Tech.	2016	Government Model Engineering College, Thrikkakara.
Computer Science with Specialization in Image Processing		Cochin University of Science & Technology.